UNIVERSITY OF CALIFORNIA, SAN DIEGO

Interfacial Engineering of Inorganic Materials for Energy Storage and Conversion Applications

A dissertation submitted in partial satisfaction of requirements for the degree

Doctor of Philosophy

in

Materials Science and Engineering

by

Mojtaba Samiee

Committee in charge:

Professor Jian Luo, Chair
Professor Renkun Chen
Professor Ying Shirley Meng
Professor Shyue Ping Ong
Professor Kenneth Vecchio

2017

The dissertation of Mojtaba Samiee is approved, and it is acceptable in quality and form for publication on microfilm and electronically:

Chair

University of California, San Diego

2017

DEDICATION

This dissertation is dedicated to my family for their endless love, support and encouragement.

TABLE OF CONTENTS

LIST OF FIGURES

LIST OF TABLES

ACKNOWLEDGEMENTS

First and foremost, I would like to thank my advisor, Prof. Jian Luo, for his generous financial support, great inspiration, patience and motivation. I was sincerely honored to work with him. I would like to express the deepest gratitude to my other committee members: Dr. Shyue Ping Ong, Prof. Kenneth Vecchio, Dr. Renkun Chen, Dr. Ying Shirley Meng for their time and guidance. Specifically I deeply appreciate fruitful discussions with Dr. Shyue Ping Ong and Dr. Ying Shirley Meng in solid state electrolytes. I am very fortunate to be able to collaborate with them on solid state electrolyte part of this thesis. I am also indebted to Prof. Kenneth Vecchio for his generous help in Materials Research Center of NanoEngineering department. I appreciate all my committee members for reading the dissertation and their comments and suggestions on my dissertation.

I am also thankful to Prof. Christoph Koch at Humboldt University of Berlin for providing the reconstruction software for inline electron holography work performed in Chapter 6 of this dissertation and his help in analyzing the phase images. I am also thankful for fruitful discussions with Dr. Mona Shirpour of University of Kentucky regarding space charge layers and electron holography results. I would also like to acknowledge my collaborators and co-authors in UCSD, Dr. Balachandran Radhakrishnan, Dr. Tom Yersak, Dr. Sunny Hy, Han Nguyen, Eric Wu, Zhi Deng and Zane Rice, whom I had many useful discussions with.

I would also like to thank Dr. Bernd Fruhberger, Ryan Anderson, Larry Grissom, Sean Parks, Ivan Harris, Dr. Jeff Wu director and staff of Nano3 facility for their support in cleanroom and also with dual beam focused ion beam and electron microscopes. I would also like to thank Kimberly Ivy of Clemson University for her help in FTIR experiments in chapter 2, Dr. Lee of University of California, Riverside for his help with XPS experiments in chapters 3 and 4, Prof. Yu Qiao of UCSD for allowing me to use BET analyzer in his lab.

I would also like to thank Prof. Hong Zhou, Ivo Atanasov, and Wong Hoi Hui of Electron Imaging Center for Nanomachines in University of California, Los Angeles and FEI engineer, Nathan DeGouzman for their support during my visits to UCLA for electron microscopy experiments.

I would also like to thank Dr. Steve Horvath, Sabine Foulhaber and Wayne Neilson of Materials Research Center (MRC) in department of NanoEngineering.

Part of this dissertation was accomplished in Clemson University and I would like to thank the faculty and staff in department of Materials Science and Engineering in Clemson University. I would like to specifically thank Prof. Igor Luzinov interim chair of the department in 2011 for providing two years of financial support as TA during my time in Clemson University.

I would also like to thank Dr. Joan Hudson, Dr. Taghi Darroudi, Dr. Haijun Qian, Dayton Cash, Donald Mulwee of electron microscopy laboratory of Clemson University and Hitachi Engineer Simon Tam for their support and help during my time in Clemson University.

I am also grateful to past and present members of Prof. Luo group, Archana Kayyar, Jiajia Huang, Dr. Jaeil Jung, Dr. Tao Hu, Jiuyuan Nie, Joshua Gild, Andrew Wright, Sicon Jiang, Naixie Zhu, Dr. Yuanyao Zhang, Dr. Shengfeng Yang, Mingde Qin.

Chapter 2, in part, is a reprint of the material “Enhancing the visible-light photocatalytic activity of TiO_2 by heat treatments in reducing environments” as it appears in Materials Letters, Mojtaba Samiee, Jian Luo, 2013, 98, 205-208. The dissertation author was the primary investigator and wrote the first draft of manuscript.

Chapter 3, in part, is a reprint of the material “A facile nitridation method to improve the rate capability of TiO_2 for lithium-ion batteries” as it appears in Journal of Power Sources, Mojtaba Samiee, Jian Luo, 2014, 245, 594-598. The dissertation author was the primary investigator and wrote the first draft of manuscript.

Chapter 4, in part, is a reprint of the material “Pseudocapacitive Properties of Two-dimensional Surface Vanadia Phases Formed Spontaneously on Titania” as it appears in ACS applied materials and interfaces, Mojtaba Samiee, Jian Luo, 2016, 8, 12871-12880. The dissertation author was the primary investigator and wrote the first draft of manuscript.

Chapter 5, in full, is a reprint of the material currently under review for publication “Divalent-doped NASICON: Improving the ionic conductivity via simultaneously optimizing the phase and chemistry of the primary and secondary phases” Mojtaba Samiee, Balachandran Radhakrishnan, Zane Rice,

Zhi Deng, Ying Shirley Meng, Shyue Ping Ong, Jian Luo. The dissertation author was the co-primary investigator and wrote majority part of this paper excluding theoretical calculations.

Chapter 6, in full, is currently being prepared for submission for publication of the material “Direct observation of space charge layers at grain boundaries of Y-doped $BaZrO_3$”, Mojtaba Samiee, Christoph Koch, Jian Luo The dissertation author was the primary investigator of this paper and wrote the manuscript.

I would like to acknowledge the financial support from the National Science Foundation under grans no. DMR-1006515 and ACI-1053575.

I would like to thank my friends Dr. Alireza Madadi, Hamid Shojaiee and Amir Beik whom have been there for me during the hard times in graduate school.

Last but not least, my deepest gratitude goes to my parents, my sister and my brothers for their love, patience and never-ending support.

VITA

2004	B.S.	University of Tehran, IRAN
2007	M.S.	Sharif University of Technology, IRAN
2017	Ph.D.	University of California, San Diego, USA

PUBLICATIONS

1. A. Kayyar, J. Huang, **M. Samiee**, J. Luo, “Construction and Testing of Coin Cells of Lithium Ion Batteries” *J. Vis. Exp.* (66), e4104, DOI: 10.3791/4104 (2012).
2. **M. Samiee**, J. Luo, “Enhancing the visible-light photocatalytic activity of TiO_2 by heat treatments in reducing environments”, Materials Letters 98, 205-208 (2013).
3. **M. Samiee**, J. Luo, “A facile nitridation method to improve the rate capability of TiO_2 for lithium-ion batteries”, Journal of Power Sources 245 (2014) 594-598.
4. **M. Samiee**, J. Luo, **“**Pseudocapacitive properties of two-dimensional surface vanadia phases formed spontaneously on titania**”**, ACS Applied Materials and Interfaces 8 (2016) 12871-12880.
5. **M. Samiee**, B. Radhakrishnan, Z. Rice, Z. Deng, Y. S. Meng, S. P. Ong, J. Luo, “Divalent-doped NASICON: Improving the ionic conductivity via simultaneously optimizing the phase and chemistry of the primary and secondary phases” Submitted in Journal of Power Sources.

6. B. Radhakrishnan, **M. Samiee**, Z. Rice, J. Luo, S. P. Ong, “Pentavalent-doped NASICON as Na solid-state electrolyte for Na solid state batteries” (in preparation)
7. **M. Samiee**, C. Koch, J. Luo, “Direct observation of space charge layers at grain boundaries of Y-doped $BaZrO_3$” (in preparation)

ABSTRACT OF DISSERTATION

Interfacial Engineering of Inorganic Materials for Energy Storage and Conversion Applications

by

Mojtaba Samiee

Doctor of Philosophy in Materials Science and Engineering

University of California, San Diego, 2017

Professor Jian Luo, Chair

Since the micrometer-sized bulk materials have reached their inherent limits, development of new materials with high performance is essential for low cost and environmentally friendly electrochemical energy storage and conversion devices. One approach is to take advantage of interfacial engineering in order to modify currently developed materials, thus improving their properties for specific applications. The advantage of interfacial

engineering is that it can also be applied to newly developed materials to further improve their properties for the specific applications. In first part of this dissertation, a systematic study is performed to investigate the effect of annealing in reducing atmospheres with different oxygen partial pressures and presence of other species (Ar, H_2, N_2, vacuum or hydrocarbon) on visible-light photocatalytic activity of TiO_2. In second part, a facile nitridation method is used to improve the rate capability of TiO_2 as anode material for Li ion batteries. The enhanced high-rate capacities are attributed to moderate surface nitridation with less-disordered nitridated regions, which may enhance the surface electronic conductivity without forming discrete, nanoscale, and surface amorphous films to block the lithium transport. In third part, pseudocapacitive properties of V_2O_5-based adsorbates supported on TiO_2 nanoparticles is systematically measured. Surface amorphous films (SAFs), which form naturally at thermodynamic equilibria at 550-600 °C with self-regulating or “equilibrium” thicknesses on the order of 1 nm, exhibit superior electrochemical performance at moderate and high scan rates (20-500 mV/s) that are of prime importance for supercapacitor applications, as compared with submonolayer and monolayer adsorbates formed at lower equilibration temperatures. In fourth part, we perform a combined experimental and computational investigation into the effects of aliovalent doping in NASICON on both bulk and grain boundary ionic conductivity. Our results show that the dopants with low solid solubility limits in NASICON solid solution lead to the formation of a conducting secondary phase at grain boundaries, thereby improving effective grain boundary conductivity

that is otherwise hindered by the poorly-conducting Na_3PO_4 and ZrO_2 secondary phases in undoped NASICON. In fifth part, inline electron holography technique is used to directly observe and investigate the space charge layers at grain boundaries of Y-doped $BaZrO_3$.

Chapter 1. Introduction

1.1 **Motivation**

Providing high-efficient, low cost and environmentally friendly electrochemical energy storage and conversion devices is of significant importance for today's information-rich and mobile society. Significant attention has been paid to research and development of key materials (electrode materials, electrolytes, etc.) which strongly affects the performance of these electrochemical devices.

Development of new materials with high performance is essential since the micrometer-sized bulk materials have reached their inherent limits in performance and cannot satisfy the needs for consumer devices. In order to develop new materials with higher performances, materials scientists are using two general approaches. One approach involves developing entirely new chemistries with superior properties than currently developed materials. The other approach involves using interfacial engineering in order to modify currently developed materials, thus improving their properties for specific applications. The advantage of interfacial engineering is that it can also be applied to newly developed materials to further improve their properties for the specific applications.

In comparison with well-acknowledged area of nanoelectronics in semiconductor physics, "nanoionics" term was coined for the first time a decade ago[1]. However, the effect of nanomaterials on electrochemical energy storage

and conversion devices can be divided to two types; 1) “trivial size effect” which rely solely on surface-to-volume ratio and 2) “true size effect” which also involve changes in local material property[1]. Regardless of these two different effects, it is of crucial importance to understand the fundamental interfacial phenomena (free surface and grain boundaries) in order to prepare interfacially-controlled materials with properties unattainable in bulk materials. Two important fundamental interfacial phenomena, namely the formation of space charges and two-dimensional interfacial phases (complexions) studied extensively by two different schools of thoughts, can markedly alter ion transport along or across various types of interfaces, including grain and phase boundaries as well as free surfaces.

Space charge theory was originally developed as a similar concept to electric double layer at electrode-electrolyte interface which was first developed by Gouy in 1903. In electrochemistry of liquid electrolytes or in colloidal systems, local deviations from electrical neutrality in the vicinity of interfaces was recognized. Defect distribution at the surface of ionic crystals was then calculated by Lehovec in 1953[2]. In 1972, Carl Wagner then used space charge layer concept to explain conductivity effects in two-phase materials[3]. Jow and Wagner[4] proposed space charge layer theory in heterogeneous ionic conductors which was then extensively developed by Maier[5–7]. Accumulation (adsorption/segregation) of net charges at interfacial core results in formation of space charge layers with opposite charge at both sides of the interface due to local electroneutrality.

Formation and transition of 2-D interfacial phases (intergranular films (IGF) and their free-surface counterpart (surface amorphous film or SAF) is another important interfacial phenomenon which can affect the ionic conductivity of oxide and nonoxide ceramic materials[8]. These 2-D interfacial phases was named as “complexions” by Tang, Carter and Cannon based on the argument that they cannot be considered “phases” according to the Gibbs definition[9].

1.2. Objective and overview

The objective of this research project is to take advantage of interfacial engineering to modify the property of inorganic materials for different aspects of energy storage and conversion applications. The project can be divided into five chapters. In **chapter 2**, a systematic study is performed to investigate the effect of annealing in reducing atmospheres with different oxygen partial pressures and presence of other species (Ar, H_2, N_2, vacuum or hydrocarbon) on visible-light photocatalytic activity of TiO_2. In **chapter 3**, a facile nitridation method is used to improve the rate capability of TiO_2 as anode material for Li ion batteries. The enhanced high-rate capacities are attributed to moderate surface nitridation with less-disordered nitridated regions, which may enhance the surface electronic conductivity without forming discrete, nanoscale, and surface amorphous films to block the lithium transport. In **chapter 4**, pseudocapacitive properties of V_2O_5-based adsorbates supported on TiO_2 nanoparticles, which form spontaneously as two-dimensional (2-D) nonautonomous surface phase (complexions) at thermodynamic equilibria, is systematically measured. Surface

amorphous films (SAFs), which form naturally at thermodynamic equilibria at 550-600 °C with self-regulating or “equilibrium” thicknesses on the order of 1 nm, exhibit superior electrochemical performance at moderate and high scan rates (20-500 mV/s) that are of prime importance for supercapacitor applications, as compared with submonolayer and monolayer adsorbates formed at lower equilibration temperatures. In **chapter 5**, we perform a combined experimental and computational investigation into the effects of aliovalent doping in NASICON on both bulk and grain boundary ionic conductivity. Our results show that the dopants with low solid solubility limits in NASICON solid solution lead to the formation of a conducting secondary phase at grain boundaries, thereby improving effective grain boundary conductivity that is otherwise hindered by the poorly-conducting Na_3PO_4 and ZrO_2 secondary phases in undoped NASICON. This is accompanied by a change in the Si/P ratio in the primary NASICON bulk phase, thereby transforming monoclinic NASICON to rhombohedral NASICON. In **chapter 6**, inline electron holography technique is used to observe and investigate the space charge layers at grain boundaries of Y-doped $BaZrO_3$. Implementation of Y-doped $BaZrO_3$ in electrochemical devices such as hydrogen fuel cells is prevented mainly due to the poor ionic conductivity which is mainly due to the space charge layers at grain boundaries.

Chapter 2. Enhancing the visible-light photocatalytic activity of TiO_2 by heat treatments in reducing environments

Following a series of recent studies that demonstrated enhanced visible-light photocatalytic activities of TiO_2 by annealing in reducing atmospheres, a systematic investigation was conducted, in which TiO_2 nanoparticles were annealed in various controlled atmospheres with the estimated oxygen partial pressure being varied from ~10^{-1} to ~ 10^{-25} atm and presence of other species (Ar, H_2, N_2, vacuum or hydrocarbon); subsequently, photocatalytic activities were tested. The results suggest that the oxygen partial pressure during annealing is not the dominant controlling factor. Furthermore, the use of vacuum environments or the presence of hydrocarbon species during annealing is effective in enhancing the photocatalytic activity, but the presence of H_2 at a partial pressure of 0.05 atm does not show an appreciable beneficial effect. HRTEM suggested that the enhanced photocatalytic activity of vacuum-activated TiO_2 may be related to subnanometer-thick disordered surface layers.

2.1. Introduction

TiO_2 based photocatalysts are promising for applications in remediation of wastes, purification of water, and generation of solar hydrogen[10,11]. However, the wide band gap of TiO_2 (>3.0 eV) limits its photocatalytic efficiency in response to solar radiation because only UV light, which counts for ~ 5% of the solar spectrum, can be utilized[10]. Doping and other strategies have been used to improve the photocatalytic efficiency of TiO_2 in response to visible light[10,11].

In a high-profile publication in *Science* in 2011[12], Mao *et al.* reported an approach to make "disorder-engineered" TiO_2 by annealing anatase nanoparticles in a 20-bar H_2 atmosphere at 200 °C to form a nanometer-thick, disordered, surface phase (akin to those impurity-based, equilibrium, surface amorphous films[13]); consequently, a "black TiO_2" powder with enhanced efficiency for photocatalytic water splitting under the irradiation of solar light was obtained. Several other recent studies [14–18] also showed that annealing TiO_2 in reducing environments (*e.g.*, in 1-bar hydrogen [15] or with active carbon[16]) can enhance the visible-light adsorption and photocatalytic activities. In particular, Xing *et al.* developed a "vacuum-activated TiO_2" via annealing TiO_2 in a vacuum drying oven at approximately 200 °C to obtain a brownish powder with improved visible-light photocatalytic activities[17]. This work demonstrated that hydrogenation is not a necessary condition for improving visible-light adsorption and photocatalytic activity and suggesting that the reducing atmosphere during annealing may be a key factor in "activating" TiO_2.

These recent studies[12,14–18] collectively point us to a new direction of improving the visible-light adsorption and photocatalytic activity of TiO_2 nanoparticle by heat treatments in reducing environments. However, a systematical investigation of the effects of oxygen partial pressure and the presence/use of other species/environments (Ar, H_2, N_2, hydrocarbon species or vacuum) on activating TiO_2 has not been conducted, which motivated this study.

2.2. Experimental Procedure

TiO_2 anatase powders (MTI, ~10 nm in size, 99.99 % purity) and methyl orange (Alfa Aesar) were purchased. To systematically test the effects of oxygen partial pressure, TiO_2 nanoparticles were annealed in a tube furnace flowing dry air, Ar – 2 % O_2, Ar, N_2, and Ar – 5% H_2, respectively, as well as in a separate vacuum furnace using a diffusion pump (with high vacuum; ~10^{-6} torr), at 200 or 450 °C isothermally. The specimens were also annealed in a vacuum drying oven (with rough vacuum; < 25 torr) at 200 °C, similar to the procedure used in the prior report[17].

The photocatalytic activities were evaluated by degradation of methyl orange in an aqueous solution under visible-light irradiation using a solar simulator (Abet Technologies; Model 10500) with a standard AM 1.5G solar spectrum equipped with a 420 nm cutoff filter. In a typical test, ~0.07 g of TiO_2 photocatalyst was added into 70 mL of an aqueous solution of methyl orange (5 mg/L). Photoreaction was performed is a water cooled jacket beaker, which was open to air. Prior to irradiation, the suspensions were magnetically stirred in a dark environment for 30 min to establish an adsorption–desorption equilibrium. After irradiation of visible light for a preset period (typically 1 hour), 3 ml aliquot was sampled and filtered. UV-Vis spectrophotometry (Agilent technologies, Cary 60) was used to determine the concentrations of methyl orange in the solution before (C_0) and after (C) irradiation at a maximum absorption band of 464 nm, and the C/C_0 ratio after 1-hour irradiation is used to represent the photocatalytic activity. A calibration curve was used for concentration

calculation (for background removal). The photocatalytic reactions were carried out at neutral pH conditions.

Fourier-transform infrared (FTIR) spectra of the samples were recorded using a Thermo-Nicolet Magna 550 FTIR spectrometer. For each sample, 16 scans at a resolution of 4 cm^{-1} were collected. A background spectrum was collected from the Diamond ATR window for the baseline correction. The surfaces of TiO_2 nanoparticles were characterized using high-resolution transmission electron microscopy (HRTEM) using a Hitachi 9500 microscope. HRTEM specimens were prepared by dispersing particles ultrasonically in isopropanol and placing a small amount of suspension onto holey carbon-coated Cu grids.

2.3. Results and Discussion

Figure 2.1 shows a photo comparing the color of TiO_2 powders annealed at 200 °C for 7 hours in different atmospheres. The TiO_2 powder annealed in the vacuum oven exhibits a brownish color, similar to that reported in the prior study[17], and the powder annealed in high vacuum shows a (lighter) yellowish color; in comparison, pristine TiO_2 and TiO_2 annealed in all other gaseous atmospheres are white.

Figure 2.2(a) summarizes the measured photocatalytic activity (C/C_0 ratios after 1-hour irradiation) for 15 different powders annealed in dry air, Ar – 2 % O_2, Ar, N_2, Ar – 5% H_2, rough vacuum, and high vacuum. The *x*-axis in Fig.

2(a) represents estimated oxygen partial pressures during the annealing for each case. A key observation is that visible-light photocatalytic activity of TiO_2 is not a simple function of the estimated oxygen partial pressure. Measured UV-vis spectra for the vacuum-activated TiO_2 were shown in Figure 2.2(b) as an example, and Figure 2.2(c) shows that C/C_0 decreases monotonically with increasing irradiation time as a result of photocatalytic degradation.

Figure 2.2(a) shows that annealing in vacuum environments appears to be the most effective method to "activate" TiO_2. This result, along with the change of color shown in Figure 2.1, is consistent with Xing *et al.*'s prior report[17]. Xing *et al.*[17] attributed the enhanced visible-light photocatalytic activity of vacuum modified TiO_2 to the formation of the associated oxygen vacancies (O_V^{2-}) and Ti^{3+} due to the partial reduction in vacuum. However, this theory would suggest a color change and increased activity for TiO_2 annealed in other reducing atmospheres such as in flowing Ar, N_2 or Ar – 5% H_2; our results (Figure 2.1 and Figure 2.2 (a)) showed that this is not true. This theory would also suggest that annealing high vacuum should be more effective in activating TiO_2, which is again inconsistent with the observations shown in Figure 2.1 and Figure 2.2(a). Furthermore, we annealed TiO_2 in Ar – 2 % O_2, where the oxygen partial pressure matches that in our vacuum oven, but the resulted powder has virtually no visible-light photocatalytic activity (Figure 2.2(a)). Thus, we conclude that while annealing in vacuum is proven effective for improving the visible-light photocatalytic activity of TiO_2, the vacuum activation of TiO_2 is not simply due to the formation of defects in reducing environments.

Furthermore, the current study shows that the annealing TiO_2 in H_2 (0.05 atm) or N_2 (1 atm) at 200 or 450 °C have little effects on improving photocatalytic activity of TiO_2 (Figure 2.2(a)). However, we should note that this result does not exclude the possible beneficial effects of hydrogenation at higher pressure/H activity (*e.g.* in 20-bar H_2[12]).

Notably, small peaks at 2800-2900 cm^{-1} that are associated with saturated C-H bonds are found in the FTIR spectra obtained from powders annealed in vacuum (Figure 2.3(d)-(g)), but they are not present in spectra obtained from pristine TiO_2 and TiO_2 annealed in Ar or dry air (Figure 2.3(a)-(c)). Noting that these C-H peaks were also evident for Xing *et al.*'s vacuum-activated TiO_2[17]. This observation suggested possible hydrocarbon contamination, which is presumably coming from vacuum oils. It is known that carbon doping can enhance visible-light photocatalytic activity[19,20]. First-principle calculations also suggested that C-H co-doping are energetically favorite and can narrow the band gap of TiO_2 more effectively than C-doping itself [21]. To test the effects of oil contamination, we intentionally placed 4 drops of vacuum oil (Maxima C plus, Fisher Scientific) in one TiO_2 specimen (~0.4g) and annealed it in flowing Ar at 200 °C for 7 hours. This oil-contaminated specimen exhibits enhanced photocatalytic activity that is comparable with the vacuum-activated TiO_2 (Figure 2.2(a)). Nonetheless, this oil-contaminated specimen only shows yellowish color that is significantly lighter than that of the vacuum-activated TiO_2 (Figure 2.1), although its FTIR spectrum exhibits a much stronger C-H peak (Figure 2.3(h)). In our experiments, we pre-pumped the

vacuum oven and closed the valve to maintain a low level of vacuum during the 7-hour annealing. Thus, the hydrocarbon contamination should be minor, which is consistent with the FTIR spectra (Figure 2.3). In conclusion, the presence of hydrocarbon contamination during low-temperature annealing in reducing atmospheres appears to be effective to enhance the photocatalytic activity, but the observed color change and activation of TiO_2 via annealing in a vacuum oven cannot be fully explained by oil/hydrocarbon contamination.

As illustrated in HRTEM images in Figure 2.4, the surfaces of vacuum-activated TiO_2 appear to be more disordered or “dirty” than the surfaces of the TiO_2 annealed in Ar–2% O_2 (with similar oxygen partial pressures). The surfaces of vacuum-activated TiO_2 look somewhat similar to those of disorder-engineered TiO_2 in the *Science* report[12]. However, it is not possible to determine whether these ultrathin disordered surface layers are hydrocarbon contaminations or disordered TiO_2 layers as claimed in the prior study[12]. What we can conclude after examining a large number of surfaces is that the surfaces of vacuum-activated TiO_2 are more disordered or “dirty” on average. It is therefore inferred that these subnanometer-thick disordered surface layers may be related to the color change and enhanced visible-light photocatalytic activity of vacuum- activated TiO_2.

2.4. Conclusions

We have systematically investigated the effects of annealing environments on improving the visible-light photocatalytic activity of TiO_2 by using 15 different heat treatment conditions, in which estimated oxygen partial

pressure vary from ~10^{-1} to ~ 10^{-25} atm. In contrast to the hypothesis that enhanced visible-light photocatalytic activity is due to the formation of defects in reducing atmospheres, this study showed that the oxygen partial pressure during annealing is not the dominant controlling factor. This study confirmed the effectiveness of the simple vacuum activation method, and suggested that the presence of minor hydrocarbon species during annealing may be a factor for enhancing the photocatalytic activity. Further HRTEM characterization suggested that subnanometer-thick disordered surface layers may relate to the color change and enhanced visible-light photocatalytic activity of vacuum-activated TiO_2. This study also showed that the presence of H_2 at a partial pressure of 0.05 atm during annealing at 200-450 °C does not show an appreciable beneficial effect.

Chapter 2, in part, is a reprint of the material “Enhancing the visible-light photocatalytic activity of TiO_2 by heat treatments in reducing environments” as it appears in Materials Letters, Mojtaba Samiee, Jian Luo, 2013, 98, 205-208. The dissertation author was the primary investigator and wrote the first draft of manuscript.

Figure 2.1 A photo comparing the color of TiO_2 powders annealed at 200 °C for 7 hours in different atmospheres as well as the pristine and "oil contaminated" TiO_2.

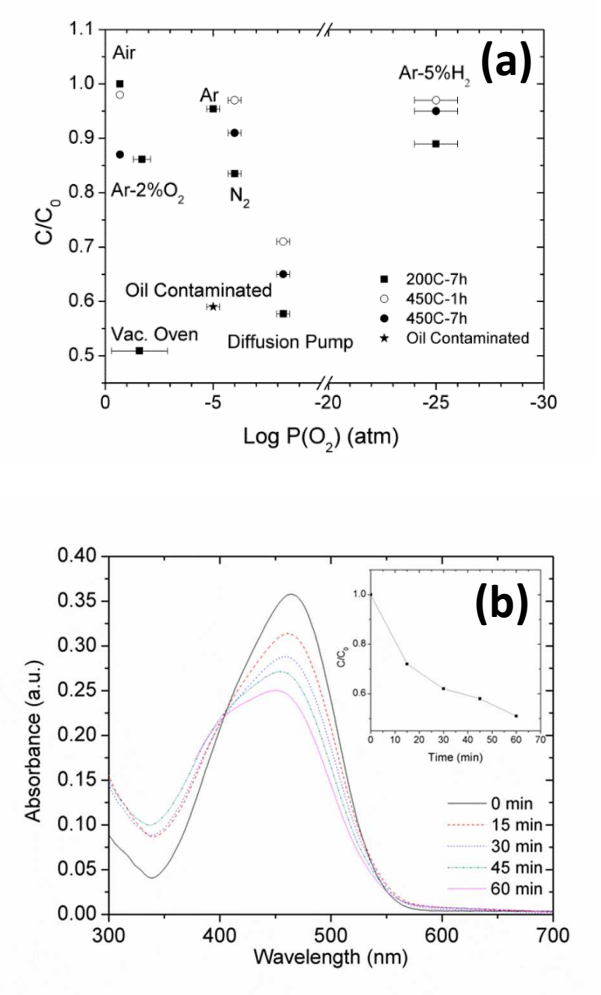

Figure 2.2 (a) Measured visible-light photocatalytic activities of TiO_2 that annealed using 15 different conditions. The *x*-axis represents the estimated oxygen partial pressures of the atmospheres used in the heat treatments. (b) Representative UV-vis absorption spectra during photodegradation of methyl orange using the vacuum-activated TiO_2 and (c) the corresponding C/C_0 (after backgroundremovals) *vs.* time.

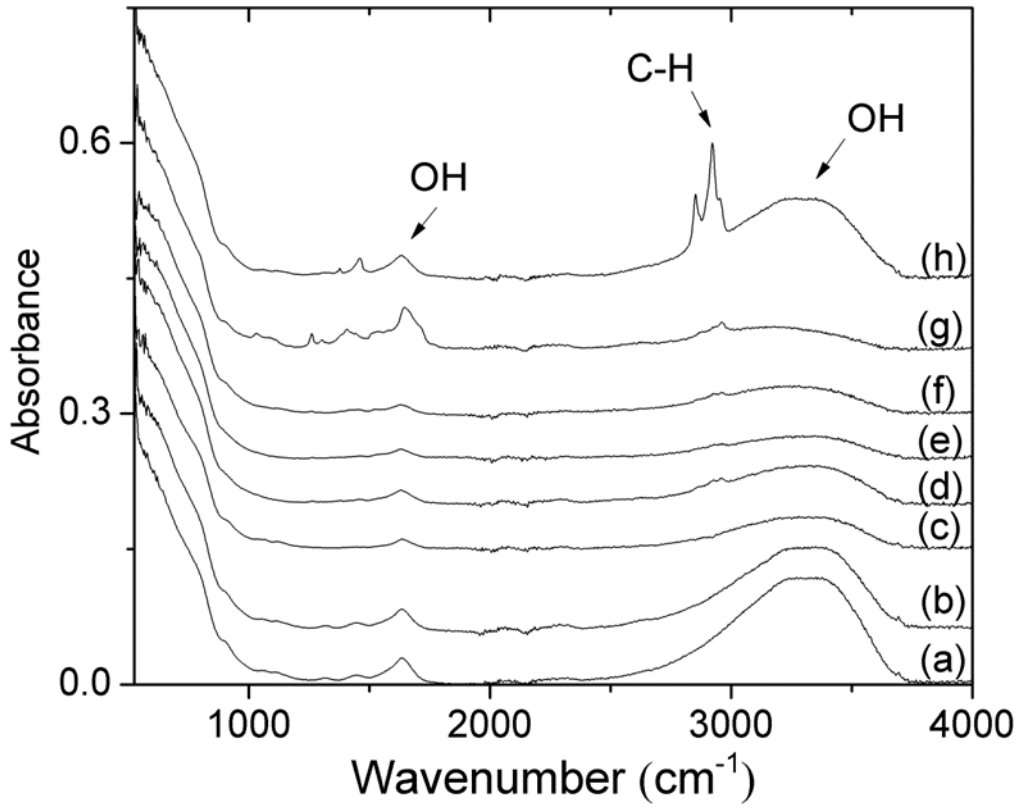

Figure 2.3 FTIR spectra of (a) pristine TiO_2 as well as TiO_2 annealed in (b) Ar and (c) dry air at 200 °C for 7 hours; in a tube furnace using a diffusion pump (d) at 450 °C for 7 hours, (e) at 450 °C for 1 hour and (f) at 200 °C for 7 hours; (g) in an vacuum oven at 200 °C for 7 hours; and (h) the "oil contaminated" TiO_2 annealed in Ar at 200 °C for 7 hours.

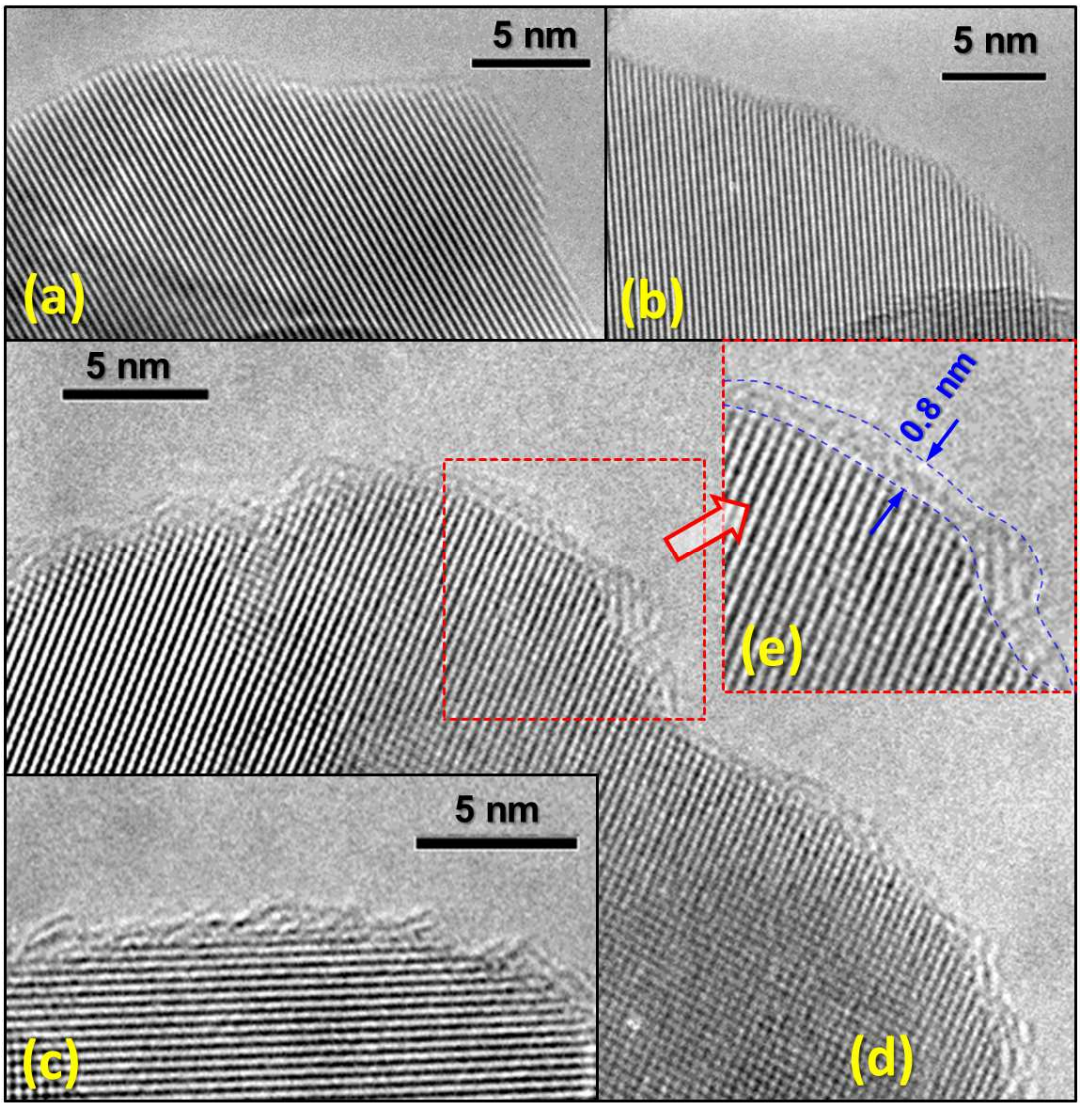

Figure 2.4 Representative HRTEM micrographs of surfaces of TiO_2 annealed in (a-b) a tube furnace flowing Ar–2% O_2 gas and (c-e) in an vacuum oven, respectively, at 200 °C for 7 hours.

Chapter 3. A facile nitridation method to improve the rate capability of TiO_2 for lithium-ion batteries

It is demonstrated that the rate capabities of TiO_2 anatase nanoparticles can be improved substantially by annealing in NH_3 at 450-500 °C. At a high nominal rate of 25C, the average discharge capacity of specimens annealed in NH_3 at 450 °C for 7h is more than double of the average capacity of the controlled specimens annealed in dry air under the same heat treatment condition. A critical comparison with literature shows that this simple and cost-effective low-temperature nitridation process leads to high-rate capacities better than those reported in prior studies. The enhanced high-rate capacities are attributed to moderate surface nitridation with less-disordered nitridated regions, which may enhance the surface electronic conductivity without forming discrete nanoscale amorphous TiN/TiO_xN_y layers to block the lithium transport.

3.1. Introduction

A series of recent studies[22–24] demonstrated that the formation of oxide-based, nanometer-thick, surface amorphous films (SAFs) can enhance the rate capabilities. As a unique high-temperature nanoscale wetting phenomenon, such SAFs can form spontaneously upon thermal annealing (driven by reduction of surface energies) with a self-selecting or “equilibrium” thickness on the order of 1 nm (in response to a balance of attractive and repulsive interface forces acting across the films)[13,24]; alternatively, these SAFs can be considered

as prewetting “surface phases”[13]. In a similar effort, Liu *et al.* annealed V_2O_5 xerogel electrodes in N_2 to form surface defects (which can be considered as another type of “surface phase”) to enhance the battery performance[25]. The assembly of these recent studies points us to a new direction of improving the rate capabilities of lithium-ion battery materials via facile thermal treatments with controlled doping or in controlled chemical environments, which is enabled by spontaneously-occurred surface modifications that are driven by surface thermodynamics.

TiO_2 has been studied extensively as an anode material for lithium-ion batteries due to its high abundance and nontoxicity. However, TiO_2 has intrinsically low Li ion diffusivity and electronic conductivity, which hinder reversible lithiation capacities, particularly at high rates. In 2008, Park *et al.* reported that thermal nitridation of $Li_4Ti_5O_{12}$ in NH_3 can enhance its rate capabilities via formation of nanoscale, conductive, amorphous layers of TiN/TiO_xN_y on the surfaces[26], and such layers exhibit similar character to those oxide-based SAFs [13,22–24]. In 2008, Han *et al*. also showed that a nitrogen plasma treatment can enhance the discharge capacity of TiO_2 nanotubes[27]. In 2011, Han *et al.* further reported that nitridation of TiO_2 hollow nanofibers via annealing in a NH_3 gas atmosphere at 600 °C enhance the rate capacity via forming similar TiN/TiO_xN_y SAFs[28]. TiN-based SAFs are expected to have high electronic conductivity to improve the rate capability of TiO_2, but TiN is electrochemically inactive with Li and thick, discrete or disordered TiN-based

surface phases may block Li transport. Thus, the surface nitridation process has to be optimized, which have not been conducted before.

In this study, a systematic approach was used to investigate the effect of nitridation of TiO_2 nanoparticles via annealing in NH_3 at different temperatures and various durations on the Li ion intercalation properties; we also conducted comparative annealing in dry air under the same conditions. This study suggests that annealing at lower temperatures of 450-500 °C in NH_3 (as compared to the 600-650 °C annealing used in prior studies[27,29]) can produce moderate surface nitridation (less disordered) without formation of discrete, nanoscale, TiN-based SAFs, which likely enhance electronic conductivity without blocking the lithium transport. Consequently, this study achieved the discharging capacities at ~25C that are better than those reported in prior studies [29–33] via a simple and cost-effective nitridation procedure with optimized heat treatment parameters.

3.2. Experimental Procedure

TiO_2 anatase powders (~10 nm) were purchased from MTI Corporation (Richmond, CA). During the thermal annealing, TiO_2 nanoparticles were loaded into alumina combustion boats, which were placed in a tube furnace flowing a controlled gas (Ar, dry air or NH_3). Before each annealing, the tube furnace was flowed with high-purity Ar for 1 h to remove the air and moisture. In a typical thermal treatment, the temperature was raised from the room temperature to 250 °C at a rate of 7.5 °C/min, hold for 1 h at 250 °C (to remove moisture in the

specimens), and raised at a heating rate of 5 °C/min to the desired (final) isothermal annealing temperature. Isothermal annealing temperatures of 450, 500 and 550 °C, respectively, were used in this study. Once reaching the final isothermal annealing temperature, the flowing gas was switched to NH_3 for nitridation. Specimens are also annealed in dry air for comparison. The final isothermal annealing duration was selected to be 1, 7 or 21 h. After the annealing was completed, the specimens were allowed to cool down under flowing Ar inside the tube furnace with power shut off.

The phase and crystallite size of the samples were evaluated by X-ray diffraction (XRD) using a Rigaku Ultima IV diffractometer with Cu K_α radiation (K_{α_1} = 1.54056), operating at 40 KV and 40 mA. Particle surfaces were characterized using high-resolution transmission electron microscopy (HRTEM) using a Hitachi 9500 microscope operating at 300 kV. HRTEM specimens were prepared by dispersing particles ultrasonically in isopropanol, placing a small amount of suspension onto holey carbon-coated Cu grids and letting dry.

Electrochemical properties of TiO_2 nanopowders were evaluated using coin cells assembled in an Ar-filled glovebox. To prepare working electrodes, a homogeneous mixture of active material, carbon black (99.9%, purchased from Alfa Aesar), and solution of Poly (vinylidene fluoride) (PVDF) (Sigma-Aldrich) in N-methyl-2-pyrrolidone (NMP) (binder) (Alfa Aesar), at a weight ratio of 80:10:10, was used. The mixture was uniformly pasted on Cu-foil (0.025 mm in thickness, 99.9%, Nimrod Hall), followed by overnight drying at 120 °C in

vacuum. Pure lithium metal discs (Sigma-Aldrich) were used as counter electrodes, and Celgard C480 membranes were used as separators. A liquid electrolyte of 1 M $LiPF_6$ in ethylene carbonate (EC)/dimethyl carbonate (DMC)/diethyl carbonate (DEC) (1:1:1, by volume) (MTI Corporation) was used. Electrochemical lithium insertion/extraction reactions were performed by an Arbin tester at different discharge rates, while all charge cycles were performed at the C/5 rate. Details of the coin cell construction and testing procedure can be found elsewhere[34]. A nominal rate of nC denotes an insertion/extraction of 1 Li in 1/nh with respect to the theoretical capacity of 330 mAh/g (noting that in literature, some used the best achievable capacity to calculate C-rates, which gave higher nominal C-rates).

3.3. Results and Discussion

A comparison of the rate performances of pristine (as-received) and various annealed TiO_2 powders at discharge rates of C/5, C, 5C, 25C and C/5 in a sequence is shown in Figure 3.1(a) Comparing with pristine TiO_2, annealing in NH_3 at 450 and 500°C for 7h substantially increases the discharging capacities at all rates. The average discharge capacity is increased by 8-10% at C/5, 10-15% at 1C, ~20% at 5C, and ~45% at 25C. Specifically, at the highest tested rate of 25C, the average discharge capacity is increased from ~38 mAh/g for as-received TiO_2 to ~55 mAh/g after annealing in NH_3 at 500 °C for 7h, which is ~120% greater than the average capacity (~25 mAh/g) of the controlled specimens annealed in dry air at 500 °C for 7h (Figure 3.1(a)). Since we

calculate the nominal C-rate with respect to the theoretical capacity of 330 mAh/g, the discharge capacity of ~55 mAh/g at the nominal 25C rate represents a full discharge in ~24 seconds (= 1/25h $\times$ 55 mAh/g / 330 mAh/g).

To systematically investigate the effect of nitridation temperature and duration, the averaged measured specific discharging capacities at 25C are plotted against nitridation time in Figure 3.1(b) for three different annealing temperatures. For annealing at 450 °C, the discharge capacity increases with increasing the nitridation time from 1 h to 7 h, and then decreases by further increasing the nitridation time to 21 h. For annealing at 500 °C, the discharge capacity decreases slightly with increasing the nitridation time from 1 h to 7 h, and then more substantially with longer annealing of 21 h. The discharge capacity *vs.* nitridation time curve at 550 °C shows a similar trend to that at 450 °C, but with substantially lower capacities.

As a benchmark, TiO_2 nanoparticles were annealed in NH_3 and dry air in the same conditions (at 400, 450 and 550 °C, respectively) for comparison (Figure 3.1(a)). Unlike annealing in NH_3, annealing in dry air decreases the discharging capacities slightly at all rates. A recent study[35] showed that annealing in air increased the capacity due to the increased crystallinity. However, in this case, the as-received TiO_2 nanoparticles already have high crystallinity and excellent reversible capacity of ~170 mAh/g at the rate of C/5; thus, further annealing in dry air did not further improve the capacity.

The discharging capacities at high rates (at ~25C nominal rate) achieved in this study via a simple nitridation treatment at the optimal heat treatment conditions (450 °C, 7h or 500 °C, 1h) are better that those reported in prior studies [29–33]; most notably, these include nitridated TiO_2 hollow nanofibers with specially-designed complex geometry to maximally enhance transport and more fabrication steps; the capacity of those nitridated TiO_2 hollow nanofibers is ~25 mAh/g at 10C, while this study achieved ~55 mAh/g (>2×) at an even higher rate 25C (2.5×)[28]. This discharge capacity of ~55 mAh/g at 25C is also better than the best achieved result of TiO_2 nanoparticles treated in H_2 (~40 mAh/g at 20C)[29]. After conducting a comprehensive literature survey and analysis, we found that this rate performance at ~25C is better than those achieved in prior studies, including TiO_2/carbon composites with high carbon loadings and smaller particles size[30], carbon coated TiO_2 using sucrose[31], Pt doped TiO_2 with a much smaller particle size of 4 nm[32], and TiO_2 nanotube/carbon composites[33].

The only better reported results for the discharge capacity at similar C-rates in literature were achieved by two much more complex composites: a "hierarchical mesoporous TiO_2: RuO_2 composite" with "efficient hierarchical mixed conducting networks" [35]and a "ultrathin TiO_2 nanotube/C" composite with smaller size (~ 3.5 nm inner diameter)[36], for which direct comparisons are probably not feasible (nor fair). It is interesting to note that even in those two reports[35,36], the performance reported here is still better than their "non-composite" controlled specimens, *i.e.*, comparable discharge capacities at 20-

30C were reported in Ref. 35 for 5-nm TiO_2 nanoparticles with high carbon loadings and in Ref. 36 with ultrathin TiO_2 nanotubes, both of which have smaller dimensions). Synthesis of those composites is presumably more complex and expensive.

Representative galvanostatic discharge/charge curves of TiO_2 powders annealed in dry air and NH_3 at 500 °C at different current densities are shown in Figure 3.2. Both sets of specimens show typical electrochemical characteristics of anatase TiO_2, exhibiting cathodic insertion of lithium at ~1.75 V and anodic extraction of lithium at ~1.95 V *vs.* Li/Li^+, which indicates the same charge/discharge mechanism. A close look at charge/discharge curves reveals that the potential separation between anodic extraction and cathodic insertion plateau is less for nitridated TiO_2 in comparison with TiO_2 annealed in dry air, which indicates better reversibility of Li^+ intercalation and deintercalation in nitridated TiO_2. By increasing the current densities (to 5C and 25C), the capacity contributed by the plateau part decreases, indicating possible surface Li storages.

XRD analysis confirmed that the TiO_2 powders annealed in air and ammonia are phase-pure tetragonal anatase, and there is no observable secondary phases by XRD (Figure 3.3); this is in agreement with previous reports that nitridation at temperatures lower than 550°C does not change the crystal structure of anatase TiO_2[28]. Particles sizes were determined to be 9-11 nm for peak broadening of X-ray diffraction based Scherrer equation using both

(101) and (200) peaks (Table I); there is no significant coarsening in all thermally treated nanoparticles. Considering there is no observable difference in the crystallite size for TiO_2 nitridated at 450-500 °C, it is interesting to note that TiO_2 nitridated at 550°C has significantly lower capacities. A similar phenomenon (of decreasing activity for annealing in NH_3) was observed for the visible-light activity of nitridated TiO_2[37], which was attributed to a change of the chemical state of N dopants in TiO_2 with increased concentration of Ti^{3+} in the surface and bulk of TiO_2 particles[37]; prior reports showing that excessive concentration of Ti^{3+} decreases the discharge capacity of TiO_2 nanoparticles via decreasing the concentration of Li^+ ions[29,38], which may explain the reduced capacities after nitridation at 550 °C.

Prior studies showed that annealing TiO_2 nanotubes[28], as well as $Li_4Ti_5O_{12}$ particles[26], in NH_3 at 600 and 650°C results in the formation of nanometer-thick, amorphous layers (or SAFs) of TiN/TiO_xN_y on the surfaces, which exhibit good electronic conductivity to enhance the rate capabilities (but are electrochemically inactive with lithium). HRTEM characterization showed that such discrete and disordered SAFs were not observed for TiO_2 nanoparticles nitridated at 450°C for 7h (Figure 3.4(c)-(d)), while the surfaces of nanoparticles nitridated at 550°C for 7h exhibit a low level of disorder (Figure 3.4(e)-(f)); the surfaces exhibit some similar disorder character to those nanoscale SAFs of TiN/TiO_xN_y observed TiO_2 nanotubes[28] and $Li_4Ti_5O_{12}$[26] nitridated at 600 and 650°C, but with thinner effective thickness and less

disordered surface structures. Consequently, it is reasonable to attribute the increased rate capability of TiO_2 annealed at 450-500 °C in NH_3 (achieved in this study) to some more moderate surface nitridation (with thinner surface nitridation region and less structural disorder in comparison with the TiN/TiO_xN_y SAFs formed after nitridation at 600 and 650°C[26,28]), presumably as a result of lower nitridation temperatures; it is known that various nitrogen species can form on the surfaces of TiO_2 nanoparticles via nitridation[37]. Although these surface nitridation regions formed at lower temperatures of 450-500 °C are more ordered and presumably thinner than the discrete amorphous layers or SAFs of TiN/TiO_xN_y formed 600 °C, it should still enhance the surface electronic conductivity; a better result achieved by this study (as comparing with those TiO_2 nanotubes nitridated at 600-650 °C[28]) may be related to thinner and less disordered surface nitridation regions (Figure 3.4) that do not block Li^+ transport.

3.4. Conclusions

We have systematically investigated the effect of nitridation temperature and time for annealing in NH_3 on the Li intercalation properties of anatase TiO_2. Nitridation at 450-500 °C increases the discharge capacities of TiO_2 nanoparticles substantially. Via this simple and cost-effective nitridation treatment, this study achieved the discharging capacities at ~25C that are better that those reported in prior studies with comparable synthesis/processing[28–33]. This study suggested that lower nitridation temperatures of 400-450 °C for

annealing in NH_3 (as compared to the typical 600-650 °C annealing used in prior studies) can lead to better results, which are attributed to more moderate surface nitridation with thinner and less-disordered nitridated regions that enhance electronic conductivity without blocking lithium transport.

Chapter 3, in part, is a reprint of the material “A facile nitridation method to improve the rate capability of TiO_2 for lithium-ion batteries” as it appears in Journal of Power Sources, Mojtaba Samiee, Jian Luo, 2014, 245, 594-598. The dissertation author was the primary investigator and wrote the first draft of manuscript.

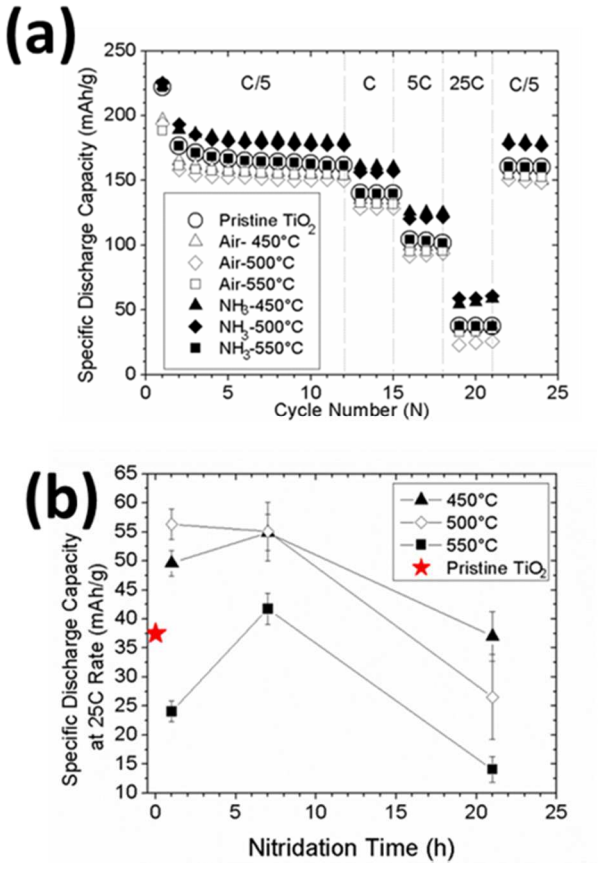

Figure 3.1. (a) Comparison of rate performances of pristine TiO_2 and TiO_2 annealed in dry air and NH_3 at 450 °C, 500 °C and 550 °C, respectively, for 7h. Discharge rates are labeled in the graph. (b) Effects of nitridation annealing time on specific discharge capacity at the 25C discharge rate for three sets of TiO_2 specimens annealed in NH_3 at 450 °C, 500 °C and 550 °C, respectively. In panel (b), each datum point represents the average of measurements of multiple specimens and the error bars are standard deviations.

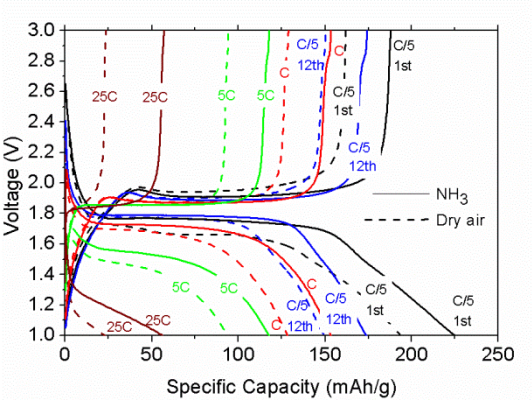

Figure 3.2 Selected galvanostatic charge/discharge profiles of TiO_2 annealed at 500 °C for 7h in dry air (dash lines) and NH_3 (solid lines) at different current densities.

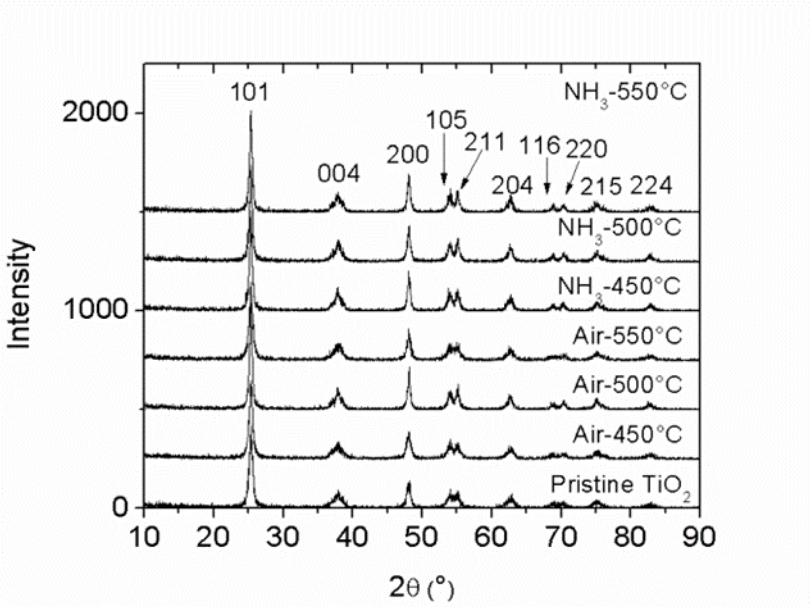

Figure 3.3 XRD patterns of pristine and annealed TiO_2. The annealing conditions are labeled.

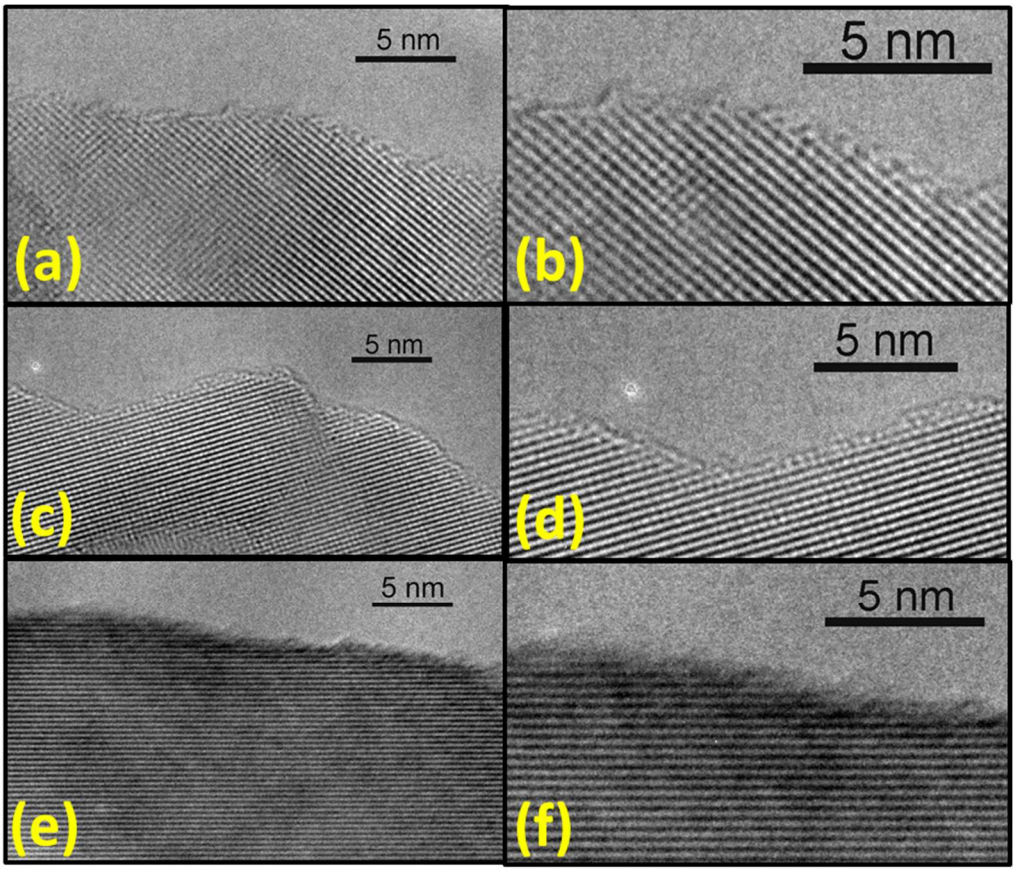

Figure 3.4 Representative HRTEM micrographs of surfaces of TiO_2 nanoparticles annealed at (a-b) 450 °C in air, (c-d) 450 °C in NH_3 and (e-f) 550 °C in NH_3, respectively, for 7 h.

Chapter 4. Pseudocapacitive Properties of Two-Dimensional Surface Vanadia Phases Formed Spontaneously on Titania

Pseudocapacitive properties of V_2O_5-based adsorbates supported on TiO_2 nanoparticles, which form spontaneously as two-dimensional (2-D) nonautonomous surface phases (complexions) at thermodynamic equilibria, have been systematically measured. Surprisingly, surface amorphous films (SAFs), which form naturally at thermodynamic equilibria at 550-600 °C with self-regulating or "equilibrium" thicknesses on the order of 1 nm, exhibit superior electrochemical performance at moderate and high scan rates (20-500 mV/s) that are of prime importance for supercapacitor applications, as compared with submonolayer and monolayer adsorbates formed at lower equilibration temperatures. This study suggests a new direction to design and fabricate a novel class of supercapacitors and other functional devices via utilizing 2-D interfacial phases that can form spontaneously via facile, cost-effective, and highly-scalable synthesis routes.

4.1. Introduction

Nanoscale surface engineering via the spontaneously-formed two-dimensional (2-D) surface phases (that were also named as "complexions" based on arguments that they are not Gibbs phases rigorously and cannot exist by themselves without the supporting bulk phases[39]) is emerging as a facile and generic method to improve the performance of a variety of functional materials

for energy related applications, including lithium-ion batteries,[22,40–42] oxygen-ion conducting nanowires,[43] and photocatalysts.[12,44] Classical examples of 2-D surface phases (complexions) are represented by monolayer and multilayer surface adsorbates that form spontaneously at thermodynamic equilibria. At high temperatures, surface adsorption can often occur in conjunction with premelting-like surface disordering; in this regard, the formation of a class of adsorbate-based surface amorphous films (SAFs) with self-selecting (equilibrium) thickness on the order of one nanometer, which form from coupled surface premelting and prewetting transitions, have been found in numerous oxide systems.[13] Thermodynamically, such 2-D surface phases (complexions) can possess structures and compositions that differ markedly from any bulk phases (e.g., SAFs are neither fully amorphous nor completely crystalline, despite they are called “amorphous” films; moreover, their average compositions can lie in the bulk miscibility gaps);[13] since they can possess atomic structure and chemistry that are *neither observed nor necessarily stable* as bulk phases, such 2-D surface phases can have distinct properties unattainable by any bulk phases.

Specifically, this study explores the feasibility of using 2-D surface adsorbates as a novel and economic class of pseudocapacitors, where the charge storage is based on fast surface redox reactions that occur only on the surfaces or in the near-surface regions. Here, a key technological motivation is that such 2-D surface phases can form spontaneously upon a facile “mixing and

annealing" process, so that the synthesis and fabrication are cost-effective and scalable. Moreover, understanding the pseudocapacitive properties of 2-D surface adsorbates (as a class of nonautonomous surface phases), which are in principle distinct from any bulk or conventional nanomaterials, is scientifically interesting and significant.

On one hand, there was already some evidence that surface modification can significantly affect the specific capacitance of carbon-based electric double layer capacitors.[45,46] On the other hand, supported oxide catalysts, where the "monolayer" adsorption of catalytic species, such as V_2O_5 and MoO_3, on a high-surface-area nanoparticles of supporting oxides, such as TiO_2 and Al_2O_3, have been widely used in the petroleum, chemical and environmental industries.[47–52]

Inspired by a supported monolayer catalyst (V_2O_5 on TiO_2), Epifani *et al.* recently reported that the submonolayer adsorption of VO_4^{3-} species on the surfaces of TiO_2 increases the voltage window, specific capacitance, and cycling stability of the capacitive performance, as well as the electrical conductivity of the material.[53] Since the capacitance of pure TiO_2 is < 1 F/g at 5 mV/s, the measured capacitance was attributed to the surface vanadia based species,[53] which should be at submonolayer levels based on the low annealing temperature of 250 °C.[47–52] These supported submonolayer vanadia catalysts can be considered as one (traditional) class of 2-D surface complexions, whose catalytic properties are modified by the interactions with the underneath metal oxide support. Epifani *et al.* adopted a low annealing temperature of 250 °C to

form submonolayer vanadia adsorbates. A series of recent studies further demonstrated that nanoscale SAFs (disordered multilayer adsorbates) of equilibrium thicknesses on the order on 1 nm will form spontaneously at thermodynamic equilibria at > 500 °C.[54,55] These nanoscale SAFs exhibit a self-limiting (equilibrium) thickness that is independent of synthesis procedures (equilibration time and the excess amount of V_2O_5, once the equilibrium was reached) but reversibly depends on the equilibration temperature.[54,55] It is scientifically interesting to investigate the pseudocapacitive properties of different types of 2-D surface phases, which is one major motivation of this study.

This present study investigated the electrochemical properties of three different types of 2-D surface vanadia phases, with a focus on surface complexions with higher levels of surface adsorptions and disorder that form at higher temperatures with significantly improved performance at moderate and high scan rates; in addition, this study measured the capacitances at a broader range of scan rates than those in the prior study.[53] Specifically, this study showed that the vanadia based surface monolayers, the typical supported catalysts used in the petroleum industry,[47–52] exhibit higher overall capacitance than submonolayer adsorbates reported by Epifani *et al.*,[53] even with the reduced surface areas due to higher annealing temperatures. More surprisingly, the nanoscale SAFs (disordered multilayer vanadia) that formed at even higher temperatures exhibit better electrochemical performance at moderate and high

scan rates of 50-500 mV/s, which are of prime importance for supercapacitor applications, despite drastic reductions in surface areas. In a broader context, these findings suggest new opportunities to design and cost-effectively fabricate a novel class of supercapacitors via utilizing on 2-D surface adsorbates that can form spontaneously via facile and scalable synthesis routes.

4.2. Experimental Procedure

4.2.1 Preparation of V_2O_5 coated TiO_2.

TiO_2 anatase powders (~10 nm, 99.99%) were purchased from MTI Corporation (Richmond, CA) and annealed at 250 °C for 4 h to remove moisture. Ammonium vanadate precursor (NH_4VO_3, 99.995%) was purchased from Alfa Aesar. The samples were prepared following a previous report.[55] Briefly, anatase powder was impregnated with a mixed solution of NH_4VO_3 and NH_4OH, and the mixtures were dried at 80 °C overnight. The dried specimens were annealed at 250, 400, 450, 500, 550 and 600 °C, respectively, for 4 h in a closed container to form submonolayer, monolayer and SAFs, and air quenched subsequently. After annealing, excess V_2O_5-enriched secondary phase form large flakes, which were carefully removed before characterization and electrochemical measurements. The overall composition of the remaining powder (without the secondary phase) was measured.

4.2.2 Characterization.

The phase and crystallite size of the samples were evaluated by X-ray diffraction (XRD) using a Rigaku Rotaflex diffractometer with Cu K_α radiation

(K_{α_1} = 1.54056), operating at 40 kV and 100 mA. Particle sizes were determined from XRD peak broadening using the Scherrer equation. A LaB_6 standard sample was used to remove the instrumental broadening. The BET surface areas of the powders were determined by nitrogen adsorption using Tristar 3000 (Micromeritics Instruments Corp.). The samples were degassed at 200 °C for 4 h prior to nitrogen adsorption-desorption measurements. The elemental analysis was performed by inductively coupled plasma-optically emission spectroscopy (ICP-OES) using a PerkinElmer 3700 optical emission spectrometer to determine the actual loading of vanadium. Typically, 20 mg of the sample was dissolved in concentrated acidic solution containing HF, H_2SO_4 and H_2O_2. Finally, the obtained solution was diluted in 10% HNO_3 aqueous solution before being analyzed by ICP-OES. X-ray photoelectron spectroscopy (XPS) measurements were carried out using a Kratos AXIS ULTRA^{DLD} XPS system equipped with an Al K_α monochromated X-ray source and a 165-mm electron energy hemispherical analyzer. The vacuum pressure was kept at $<3 \times 10^{-9}$ torr during the measurements and a neutralizer was applied to compensate the charging issue during the measurement. All the XPS spectra were referenced to the C 1s peak at 284.8 eV of the surface adventitious carbon.

4.2.3 Electrochemical Measurements.

Electrochemical properties were evaluated in symmetrical two-electrode Swagelok cells with 0.1 M K_2SO_4 and 8 M LiCl as the electrolytes. The working electrode was prepared by a homogeneous mixture of active material

(V_2O_5/TiO_2), carbon black (99.9%; Alfa Aesar), and a solution of Poly (vinylidene fluoride) (PVDF) (Sigma-Aldrich) in N-methyl-2-pyrrolidone (NMP) as the binder (Alfa Aesar), at a weight ratio of 80:10:10. The mixture was uniformly pasted on a Ni foam using a painting brush, followed by drying at 120°C in vacuum for 8 hrs. Celgard 3501 membrane was used as separator. The electrochemical properties and capacitance measurements of the samples were studied by cyclic voltammetry (CV) on a Solartron 1287 Potentiostat/Galvanostat. The following equation was used in order to determine the specific capacitance values by using the cyclic voltammetry method:

$$C = \int_{E_1}^{E_2} i(E)dE/(E_2 - E_1)mv \ , \qquad (3\text{-}1)$$

where C is the specific capacitance of individual sample. E_1 and E_2 are the cutoff potentials in cyclic voltammetry, and $i(E)$ is the instantaneous current. The integral $\int_{E_1}^{E_2} i(E)dE$ is the total charge obtained by integration of positive and negative sweep in cyclic voltammetry. $(E_2 - E_1)$ is the potential window width. m is the amount of vanadium loaded on each electrode. Galvanostatic constant current charge-discharge was performed in symmetric configuration of Swagelok cells at 600 mA/g using an Arbin tester. The average specific capacitance can be evaluated using the following equation:

$$C = 4(I\Delta t)/(m\Delta V) \ , \qquad (3\text{-}2)$$

where C is the specific capacitance, I is the discharging current (A), Δt is the discharging time, ΔV is the discharging voltage and m is the mass of active

material. Electrochemical Impedance Spectroscopy (EIS) was carried out using Solartron 1287 electrochemical interface coupled with a Frequency Response Analyzer (1255B) with an AC amplitude of 10 mV and a frequency range of 1 MHz to 2 mHz at open circuit potential of each sample. All the electrochemical studies described above were performed at room temperature (~25 °C).

4.3. Results

4.3.1. Characterization of V_2O_5-doped TiO_2 Nanoparticles.

As being expected, the measured Brunauer–Emmett–Teller (BET) surface area of TiO_2 nanoparticles decreases with increasing annealing temperature due to nanoparticle coarsening (Figure 4.1(a)). Specifically, increasing the annealing temperature from 250 °C to 400, 450, and 500 °C, respectively, reduces the surface area from 112.4 m^2/g to 87.5, 89.5, and 70.4 m^2/g, respectively, representing ~20-37% reductions. Moreover, the surface area is further reduced by 71% to 32.4 m^2/g, when the annealing temperature is increased to 550 °C. Finally, annealing at 600 °C further reduces the surface area by as much as 94 % to only 6.3 m^2/g. The reductions of surface areas are clearly evident in nitrogen adsorption–desorption isotherms (Figure 4.1(b)), where all the samples, except for the one annealed at the highest temperature of 600 °C, exhibit a typical type IV absorption behavior with distinct hysteresis loops that are characteristic of mesoporous and macroporous materials, and the measured pore size also increases with increasing annealing temperature (Table 4-1). The coarsening processes can also be evident by the narrowing of

X-ray diffraction (XRD) peaks for the specimens with increasing annealing temperatures (Figure 4.2(a)). No vanadium oxide peak was observed for any specimens; low-intensity XRD peaks attributed to the formation of minor TiO_2 rutile phase are observed only in the specimen annealed at 600 °C, but absent for all other specimens annealed at lower temperatures.

4.3.2. Formation of 2-D Surface Vanadia Phases at Different Equilibration Temperatures.

While the surface area of TiO_2 nanoparticles decreases, submonolayers, monolayers or multilayers (SAFs) of surface vanadia species form in sequence at thermodynamic equilibria with increasing equilibration temperature (Figure 4.1(a)). High resolution transmission electron microscopy (HRTEM) shows that nanometer-thick, V_2O_5-based SAFs form on the surfaces of the TiO_2 nanoparticles annealed at 550 and 600 °C (Figure 4.3(a)); the corresponding measured means of, and standard deviations in, the SAF thicknesses are plotted in Figure 4.1(a), which are based on the measurements conducted in a prior systematic HRTEM study.[54,55] The surface vanadia species formed at 500 °C or lower temperatures are below the detect limit of HRTEM (Figure 4.3(b)); however, the formation of monolayer and submonolayer surface vanadia species upon annealing at 250-500 °C has been well established by extensive prior studies of supported monolayer catalysts,[47–52] and it is further verified by our X-ray photoelectron spectroscopy (XPS) results shown in Figure 4.2(b).

Furthermore, XPS results indicate that the binding energy of vanadium species shifts towards the higher end, especially with SAF formation at 550 and 600 °C, as comparing with the ones annealed at lower temperatures, suggesting higher oxidation states of vanadium that may affect the capacitance.

4.3.3. Electrochemical Performance of Different 2-D Surface Vanadia Phases.

As shown in Figure 4.4(a) and 4.4(b), the integrated areas of CV plots for pure TiO_2 at both 5 and 100 mV/s are significantly smaller than the nanoparticles with surface vanadia (and essentially negligible), confirming that the capacitances are mostly from the 2-D surface vanadia species.

Moreover, Figures 4.4(c)-(h) illustrate that the specimen equilibrated at 400 °C (with surface vanadia monolayers) has the highest capacitances at low scan rates of 5 and 20 mV/s, while the specimen equilibrated at 600 °C (with nanoscale SAFs; Figure 4.3(a)) has the highest capacitances at higher scan rates of 100-500 mV/s. Although some resistive behaviors are observed for nanoparticles with surface vanadia specimens at submonolayer and monolayer levels at 100 mV/s or higher scan rates, the CV plots for the specimens with multilayers/SAFs are not distorted at these high scan rates. For figure clarity, CV plots of only three representative specimens with three different types of surface vanadia phases are displayed in Figure 4.4; additional CV plots for all six specimens measured at six different scan rates are presented in Figures 4.5.

Specific capacitances of six different specimens with different 2-D surface vanadia phases measured at six different scan rates (from 5 to 500 mV/s) were calculated and plotted in Figure 4.6(a) for comparison. At the lowest scan rate of 5 mV/s, the formation of full monolayers (via increasing the equilibration temperature from 250 to 400 °C) improves the specific capacitance by 25% to ~137 $F/g_{v_2O_5}$ (despite a ~22% reduction in measured BET surface area). Further increasing the equilibration temperature beyond 400 °C will reduce the specific capacitance per gram of active material gradually at this low scan rate of 5 mV/s, which is due to the reduction of surface area; Figure 4.6(b) further shows that the measured capacitance per BET surface area is virtually constant in the monolayer region regardless of the annealing temperatures and in fact increases with the SAF formation at higher temperatures.

At high scan rates, the specific capacitance increases monotonically with increasing the equilibration temperature; for example, at a scan rate of 200 mV/s, the measured specific capacitances are 8, 14.8, 14.23, 17.17, 40.26 and 49.19 $F/g_{v_2O_5}$, respectively, for the specimens annealed at 250, 400, 450, 500, 550 and 600 °C, respectively. This dependence on equilibration temperature is more significant for the measured specific capacitances per BET surface areas, as shown in Figure 4.6(b).

Cycling stability of specimens with different 2-D surface vanadia phases, measured at a constant current of 600 $mA/g_{total\ oxide}$, in 0.1 M K_2SO_4 electrolyte is shown in Figure 4.7(a). The gradual decaying of capacitances

during the cycling is presumably due to the dissolution of vanadia into K_2SO_4 electrolyte, and it can be mitigated by using other types of electrolytes. To demonstrate the feasibility of improved cycling stabilities, a significantly improved cycling performance with ~96% retention after 500 cycles was observed for the specimen annealed at 600 °C in an 8 M LiCl electrolyte (Figure 4.7(b)). Yet, 0.1 M K_2SO_4 (instead of 8 M LiCl) electrolytes were used in most of this study to test the intrinsic pseudocapacitive properties of 2-D surface vanadia phases to avoid complexity due to the possible intercalation of Li^+ ions into underneath TiO_2 particles.

The galvanic constant current charge-discharge curves (measured at 600 $mA/g_{total\ oxide}$) in 0.1 M K_2SO_4 are shown in Figure 4.8 where the deviations from ideal triangular shapes can be attributed to pseudocapacitive reactions due to 2-D surface vanadia phases (presumably involving subsurface redox reactions). The charge-discharge curves of the specimens with nanoscale SAFs are largely symmetric and they are prolonged over the specimens with submonolayers and monolayers of surface vanadia, revealing good capacitive behaviors.

Nyquist plots of AC impedance of all six specimens are shown in Figure 4.9. The specimens with submonolayers and monolayers of surface vanadia display two semi-circles at high- and mid-frequencies (with large second semi-circles at mid-frequencies), followed by spikes in low frequency regions, whereas the specimens with nanoscale SAFs exhibit typical pseudocapacitive

behaviors with small semi-circle at high frequencies, followed by spikes at mid-frequencies, as shown in the inset of Figure 4.9.

4.4 Discussion

A series of prior studies[50,54,55] have already demonstrated that a variety of 2-D vanadia phases, particularly the monolayers and nanoscale surficial films (a.k.a. disordered multilayer adsorbates or SAFs), can form on the surfaces of titania spontaneously at thermodynamic equilibria through facile, cost-effective, and scalable mixing and annealing processes. Once the thermodynamic equilibria are achieved, the surface configuration and absorption amount (i.e., the surface V coverage or the effective thickness of the surficial film) should be independent of synthesis procedure/history but is a function of the equilibration temperature.

Specifically, a nanometer-thick vanadia-based surficial film can form spontaneously at sufficiently high temperatures (550-600 °C in this case), driven by the reduction of surface energy:

$$\Delta\gamma \equiv \gamma_{\text{vanadia}} + \gamma_{\text{vanadia-titania}} - \gamma^{(0)}_{\text{titania}} < 0, \qquad (3\text{-}3)$$

where *h* is the film thickness and $\gamma's$ are interfacial energies.[13,54,55] Moreover, these nanoscale surficial films or SAFs appear to be largely disordered in HRTEM (Figure 4.3(a)) because the formation of crystalline surface vanadia films is frustrated by the high crystal-to-crystal interfacial energy that would

occur, although existence of partial orders in such surficial films is confirmed (even if they are named as surface "amorphous" films or SAFs).[54,55]

The stabilization of a subsolidus, quasi-liquid, surficial films (SAFs) can be conceived as if the increased free energy for forming the undercooled liquid film ($\Delta G_{\text{amorph.}}^{(\text{vol.})} \cdot h$) is over-compensated by $-\Delta\gamma$. In a pressure-balance model[13,54–56] that was adapted from the original Clarke model for equilibrium-thickness intergranular films,[57,58] the excess surface energy (referred to a "clean" titania surface without adsorption or $\gamma_{\text{titania}}^{(0)}$) can be expressed as:

$$\Delta\sigma(h) = \Delta\gamma + \Delta G_{\text{amorph.}}^{(\text{vol.})} \cdot h + \sigma_{\text{vdW-Ld}}(h) + \sigma_{\text{elec.}}(h) + \sigma_{\text{short-range}}(h) + \ldots \quad , \tag{3-4}$$

which includes the amorphization energy as well as the van der Waals London dispersion (vdW-Ld), electrostatic and short-range interfacial interactions. A surficial film may form spontaneously if $\Delta\sigma(h) < 0$, and the equilibrium thickness corresponds to a minimum in $\Delta\sigma(h)$.

The equilibrium thickness of the SAFs (a.k.a. disordered multilayer adsorbates) decreases with decreasing temperature because of the $\Delta G_{\text{amorph.}}^{(\text{vol.})} \cdot h$ term, which represents a constant attractive pressure that increases by ~1 MPa/K (approximately the volumetric fusion entropy of V_2O_5) with reducing temperature.[54] Thus, the nanometer-thick vanadia-based surficial will transit ("collapse") to monolayers (via a first-order surface phase-like transformation) at ~500 °C with a hysteresis loop (i.e., nanoscale SAFs form at ~500 °C with

increasing temperature but vanish at ~450 °C with decreasing temperature).[54] Thus, monolayers of surface vanadia form in specimens equilibrated at 400-500 °C (Figure 4.1(a)), the formation of which are well expected from extensive prior studies of V_2O_5 on TiO_2 monolayer catalysts;[47–52] the presence of surface vanadia is also verified by our XPS results (Figure 4.2(b)). We further estimate the nominal surface coverages of vanadium for these specimens by using the measured BET surface areas and overall composition measured by ICP. As shown in Table 4.1, the nominal surface coverages are estimated to be 5.68, 5.77, and 5.64 V atom/nm^2, respectively, for specimens annealed at 400, 450, and 500 °C, respectively, which is close to the theoretical monolayer coverage of ~8 V atoms per nm^2 (where the difference may be explained by the fact that surface vanadia has a different density).[52] The constant surface coverage (~5.6-5.8 V atom/nm^2) for specimens equilibrated in the temperature range of 400-500 °C is also an indication that an equilibrium monolayer coverage is reached at this plateau. In contrast, the nominal vanadium surface coverage is estimated to be 3.89 V atom/nm^2 for the specimen annealed at 250 °C, indicating the formation of submonolayers.

Compared with the recent study of Epifani *et al.* (of the pseudocapacitive properties of V_2O_5-based submonolayers formed at a lower temperature of 250 °C),[53] the current study illustrated that surface monolayers perform better at all scan rates; moreover, SAFs/multilayers perform significantly better at thigh scan rates. Specifically, using three electrodes cells, Epifani *et al.* recently reported

a specific capacitance of 125 $F/g_{v_2O_5}$ at a low scan rate 5 mV/s for a sample annealed at 250 °C (with submonolayers),[53] which is close to the value obtained in this investigation (~109 $F/g_{v_2O_5}$). A slight difference between the two values can be attributed either to the differences in electrode preparation procedures or different cell setups. However, cyclic voltammetry at higher scan rates has not been studied in that prior report,[53] although higher scan rates are of crucial importance for supercapacitor applications (as discharging within ~1 minute corresponds to typical scan rates of 20-40 mV/s).[59] This study showed that the measured capacitance for the submonolayer specimen (annealed at 250 °C) decreases rapidly with increasing scan rates in the range of 20 to 500 mV/s (Figure 4.10); specifically, it decreases from ~109 $F/g_{v_2O_5}$ at 5 mV/s to ~23 $F/g_{v_2O_5}$ at 50 mV/s and only ~5 $F/g_{v_2O_5}$ at 500 mV/s, which represent only ~20% (at the 10× scan rate) and ~5% (at the 100× scan rate), respectively, of the capacitance measured at the slow scan rate of 5 mV/s. As we will discuss in detail later, the lower high-rate performance may be related to diffusion-controlled process in this specimen. In case of specimen with complete monolayer (annealed at 500 °C), the measured capacitance decreases rapidly with increasing scan rates in the range of 50 to 500 mV/s (Figure 4.10); specifically, it decreases from ~120 $F/g_{v_2O_5}$ at 5 mV/s to 48 $F/g_{v_2O_5}$ at 50 mV/s and only 8 $F/g_{v_2O_5}$ at 500 mV/s, which represents 40% (at the 10X scan rate) and 6% (at 100X scan rate), respectively, of the capacitance measured at the low scan rate of 5 mV/s. In contrast, for the specimen annealed at 600 °C with

SAF formation, the measured capacitance decreases from ~82 $F/g_{v_2O_5}$ at 5 mV/s to ~65 $F/g_{v_2O_5}$ at 50 mV/s and ~34 $F/g_{v_2O_5}$ at 500 mV/s, which represent ~79% (at the 10× scan rate) and ~41% (at the 10× scan rate), respectively (Figure 4.10).

All three specimens with monolayers of surface vanadia (formed at 400-500 °C, with ~5.6-5.8 vanadium atoms per nm^2; Table 4.1) exhibit similar capacitances at each scan rates (Figure 4.3(a) and Table 4.1, as well as Figure 4.3(b) for capacitances normalized to per unit BET surface area), which outperforms the specimen with submonolayer surface vanadia formed at a lower temperature of 250 °C (with ~3.9 vanadium atoms per nm^2; Table 4.1), despite ~20-37% reductions in BET surface areas after annealing at higher temperatures (Figure 4.1(a)).

Moreover, the specimen with nanoscale SAF formation (multilayer vanadia adsorbates; see Figure 4.6(a) and Figure 4.7(a)) outperformed specimens with submonolayers and monolayers of surface vanadia at moderate and high scan rates of 50-500 mV/s. To benchmark the pseudocapacitive properties of 2-D surface vanadia phases, we first compare them with electrospun V_2O_5 fibers. Specific capacitances of nanoscale SAFs are significantly higher than those reported for electrospun V_2O_5 nanofibers of ~500-800 nm in diameters (tested in $LiPF_6$ in EC/DEM),[60] particularly at high scan rates (*e.g.*, ~5-6× at 50-100 mV/s) but are ~20% lower than the K-intercalated layered V_2O_5 nanofibers of ~120 nm in diameters (with ~20 wt. % C added,

tested in a more concentrated electrolyte of 2M KCl);[61] noting that quantitative comparisons may be difficult because different electrolytes and carbon loading (and a low electrolyte concentration of 0.1 M K_2SO_4 and relative low carbon loading of 10 wt. % were used in this study to probe the intrinsic pseudocapacitive properties of 2-D surface vanadia phases). However, the capacitances are still significantly lower than nanometer-thick V_2O_5 coated on mesoscale ITO scaffold [62] or mesoscale ITO scaffold[63] via atomic layer deposition (ALD) or other sophisticated synthesis routes with fine processing controls; the differences are presumably due to the much high conductivities of ITO and carbon nanotubes. Yet, the 2-D surface vanadia phases can form spontaneously via on abundant TiO_2 nanoparticle supports via a cost-effective and scalable synthesis method (that can be extended to many other materials systems), thereby having advantages in both cost and manufacturability.

Here, the scalability and potential low costs are related to the fact that TiO_2 nanoparticles have already been produced cost-effectively in a large scale; furthermore, the proposed V_2O_5/TiO_2 supercapacitor electrode materials can be fabricated via simply mixing and annealing cheap TiO_2 nanoparticles with V-containing salts, which can (again) be done in a large-scale production easily (as the petroleum industry is already doing for making V_2O_5/TiO_2 based catalysts). In addition, V_2O_5/TiO_2 is only one of the possible systems and there are many other existing (or potentially new) oxide systems that form similar (or even different types of) 2-D surface phases, which may have good/better electrochemical properties and should be explored in future studies.

This study also reveals some intriguing and fascinating scientific findings about pseudocapacitive properties of 2-D surface vanadia phases. An interesting observation from Figure 4.6 and Table 4.1 is at the higher scan rates of 50-500 mV/s, the measured capacitances generally increase with increasing annealing temperature, despite of the significant reductions of BET surface areas. Take the measurements conducted at the scan rates of 100 mV/s as an example, the measured capacitance is ~13 $F/g_{v_2O_5}$ for the specimen equilibrated at 250 °C with an BET surface area of ~112 m^2/g. After annealing at 400-500 °C, the BET surfaces areas are reduced by ~20-37% to ~70-90 m^2/g with the formation of monolayers, but the measured capacitances increase by >280% to ~49-51 $F/g_{v_2O_5}$. Furthermore, after annealing at 550 and 600 °C, the BET surfaces areas are further reduced by ~71% and ~94% to ~32 m^2/g and ~6 m^2/g, respectively, with the formation of nanoscale SAFs, but the measured capacitances further increase by >300% (>4X) to ~55-59 $F/g_{v_2O_5}$. These results are in contrast with numerous previous reports of higher specific capacitances for materials with higher specific surface areas for both electric double layer capacitance[64–66] as well as pseudocapacitance materials. [67–69] Nonetheless, the somewhat unusual behaviors at high scan rates can be explained by charge transfer processes. Specifically, in specimens with submonolayer and monolayer 2-D surface phases with high surface areas, the interaction of electrolyte and TiO_2 nanoparticles becomes more significant compared with specimen with multilayers/nanometer-thick SAFs which has a

much lower surface area. The small semicircles observed at high frequencies in Nyquist plots of all specimens are due to the electrode/electrolyte interface (electrode resistance) which is also very similar for different specimens with different 2-D surface phases. However, specimens annealed at 250-500 °C exhibit additional large semicircles at mid-frequencies, whose diameters are correlated with the surface area of the specimens. The specimen with submonolayers and highest surface area has the highest charge transfer resistance and specimens with monolayers with lower surface area has smaller charge transfer resistance while the specimens with multilayers/nanoscale SAFs have a very small charge transfer resistance. The charge transfer resistance is known to be correlated with the surface area and conductivity of the active material.[70]

Improvements in redox reaction kinetics and electrochemical activity are also evident for specimens with formation of nanoscale SAFs, as compared with specimens with submonolayers and monolayers of 2-D surface vanadia phases, which are indicated by the shifts of the onset potential of oxidation peaks in Figures 4.4 and 4.5. This is also in agreement with the XPS results (Figure 4.2(b)), where a chemical shifts towards the high-energy end indicates higher oxidation states of vanadium with higher concentrations of 5+ vanadium cations with the formation of nanoscale SAFs. It has been reported that fully oxidized V (5+) surface VO_x species are more efficient for redox reactions.[71] DFT calculations has also shown that loading vanadium oxide on titania results in

band gap reduction improving the electronic properties of vanadium oxide which can lead to possible change in the reactivity of the catalyst.[72] Band gap engineering is shown to improve the electrical properties of materials for supercapacitor applications.[73]

The significantly-better performances of specimens with nanoscale SAFs at high scan rates, as compared with specimens with monolayers of surface vanadia phases, also suggest possible subsurface redox reactions, which may be facilitated by the fact that these nanoscale SAFs are partially ordered with more open structures than the normal glasses;[13,54,55] a recent study showed that such partially-ordered and partially-disordered SAFs strained on curved surfaces may enhance the ionic transport in nanowires,[43] and it is possible that a similar effect may promote ion transport and enable/enhance subsurface redox reaction in the current case.

Finally, it should be noted that this study intentionally used low vanadium contents (where all vanadia species are on the surfaces) to ensure the measurements of intrinsic behaviors of 2-D surface vanadia species. Using higher vanadium contents can further increase the specific capacitance per total oxides.[74] In addition, both the specific capacitance and the cycling stability can be further improved by using different types of electrolytes, as shown in a previous report[75] as well as demonstrated in Figure 4.7(b) of this study. The primary scientific goal of this study is to understand the pseudocapacitive properties of 2-D surface vanadia species (*vs.* optimizing the whole system) as

an example to demonstrate the potential of 2-D surface phases. Yet, this study demonstrated that the pseudocapacitive properties of vanadia-based nanoscale SAFs supported on TiO_2 are significantly better that those of the submonolayer vanadia adsorbates reported in a recent pioneering study by Epifani *et al.* that first pinpointed the possibility of utilizing surface vanadia species as pseudocapacitors,[53] particularly in the moderate and high capacitance regions (20-500 mV/s) that are of practical importance. We again emphasize that such 2-D surface vanadia species can form spontaneously (via a facile and scalable "mixing and annealing" process) on the surfaces of the abundant TiO_2 anatase nanoparticles, which can be produced cost-effectively in a large quantity; the relevant synthesis and processing routes via utilizing spontaneously-formed 2-D surface phases (that can be extended to many other materials systems) are generally economic and have excellent scalability and manufacturability.

4.5. Conclusions

In summary, we have investigated the pseudocapacitive properties of 2-D vanadia phases that form spontaneously on the surfaces of TiO_2 nanoparticles during annealing. Annealing at low temperatures (< 300 °C) results in high surface area nanoparticles with submonolayers of 2-D surface vanadia and small pore sizes, with a good capacitance at a low scan rate of 5 mV/s decaying rapidly with increasing scan rate. Annealing at medium temperatures of 400-500 °C results in specimens with 20-37% lower surface areas and high surface V coverages of monolayers of 2-D vanadia, which improved specific capacitances per unit active material at all rates. Nanoscale

surficial vanadia films (SAFs or multilayer adsorbates) form at high equilibration temperatures of 550-600 °C, which lead to significantly-better performances at moderate and high scam rates (20-500 mV/s), despite the significant reduction of surface areas.

This study suggests a new direction to design and cost-effectively fabricate a novel class of supercapacitors based on 2-D surface adsorbates that can be made via facile and scalable synthesis routes. A related general scientific goal is to utilize 2-D interfacial phases to achieve distinct and unique properties, which has recently been demonstrated for lithium-ion batteries,[22,40–42] oxygen-ion conducting nanowires,[43] and photocatalysts;[12,44] this study further extends it to supercapacitors. The facile synthesis and processing routes via utilizing spontaneously-formed 2-D surface phases can be further extended to various other materials systems with excellent scalability and manufacturability.

Chapter 4, in part, is a reprint of the material “Pseudocapacitive Properties of Two-dimensional Surface Vanadia Phases Formed Spontaneously on Titania” as it appears in ACS applied materials and interfaces, Mojtaba Samiee, Jian Luo, 2016, 8, 12871-12880. The dissertation author was the primary investigator and wrote the first draft of manuscript.

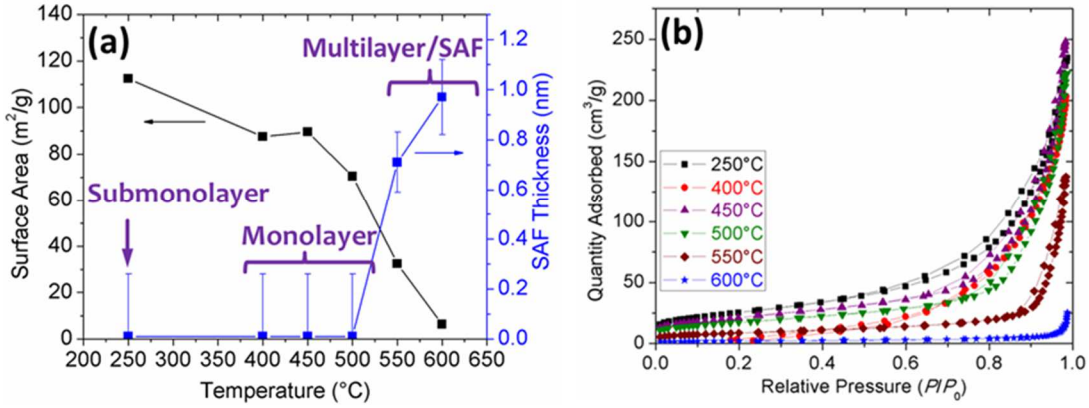

Figure 4.1 (a) The measured BET surface areas and the thicknesses (or equivalent thicknesses) of the 2-D vanadia phases formed on the surfaces of TiO_2 nanoparticles vs. annealing/equilibration temperatures. For specimens annealed at 500 °C or lower, the 2-D surface vanadia phases are not discernible in HRTEM (< 0.3 nm); the corresponding horizontal bars represent the equivalent thicknesses calculated from the nominal surface coverages of V listed in Table 1, assuming (for simplicity) that the density of 2-D surface vanadia phase is identical to that of bulk V_2O_5; (b) Nitrogen adsorption-desorption plots for specimens annealed at different temperatures.

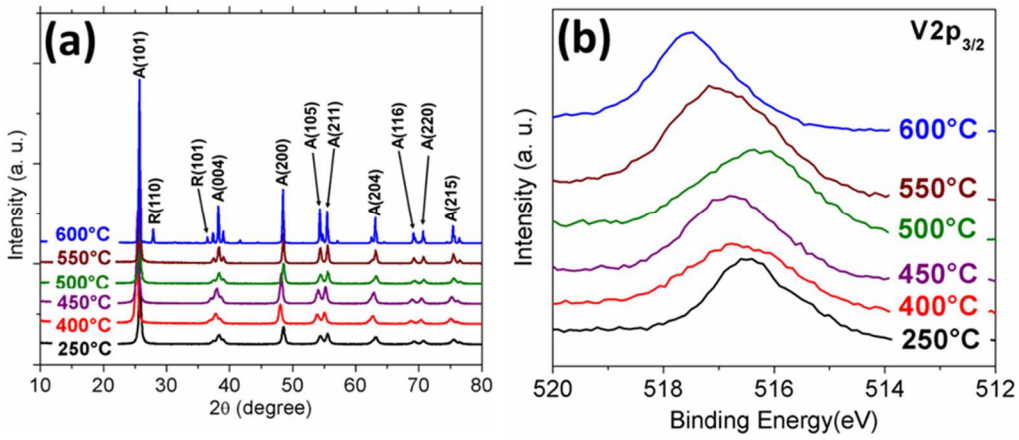

Figure 4.2 (a) X-ray diffraction (XRD) patterns of specimens annealed at different temperatures. Anatase and rutile phases are labeled by A and R respectively. No peaks related to vanadium oxides were observed. (b) XPS spectra of V2p3/2 peaks for specimens equilibrated at different temperatures, confirming the presence of surface vanadium species for all cases.

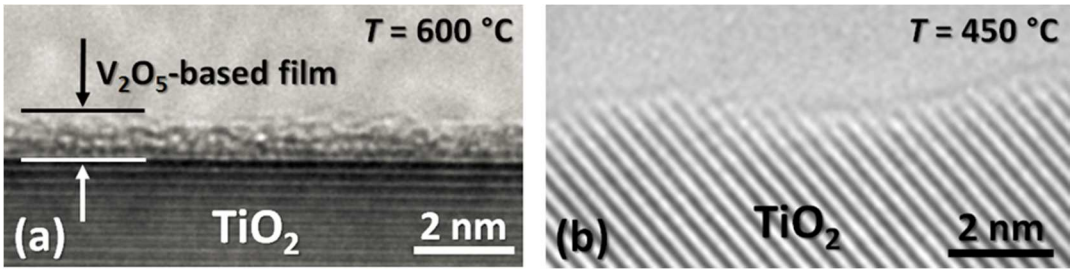

Figure 4.3 (a) A representative, nanometer-thick, vanadia-based SAF formed on TiO_2 in a specimen annealed at 600 °C. (b) A representative "clean" surface of TiO_2 nanoparticles for specimens equilibrated at 250-500 °C (450 °C for this specific case), where monolayers (or submonolayers) of 2-D surface vanadia phases are not discernible in HRTEM but have been detected by XPS (Figure 2b).

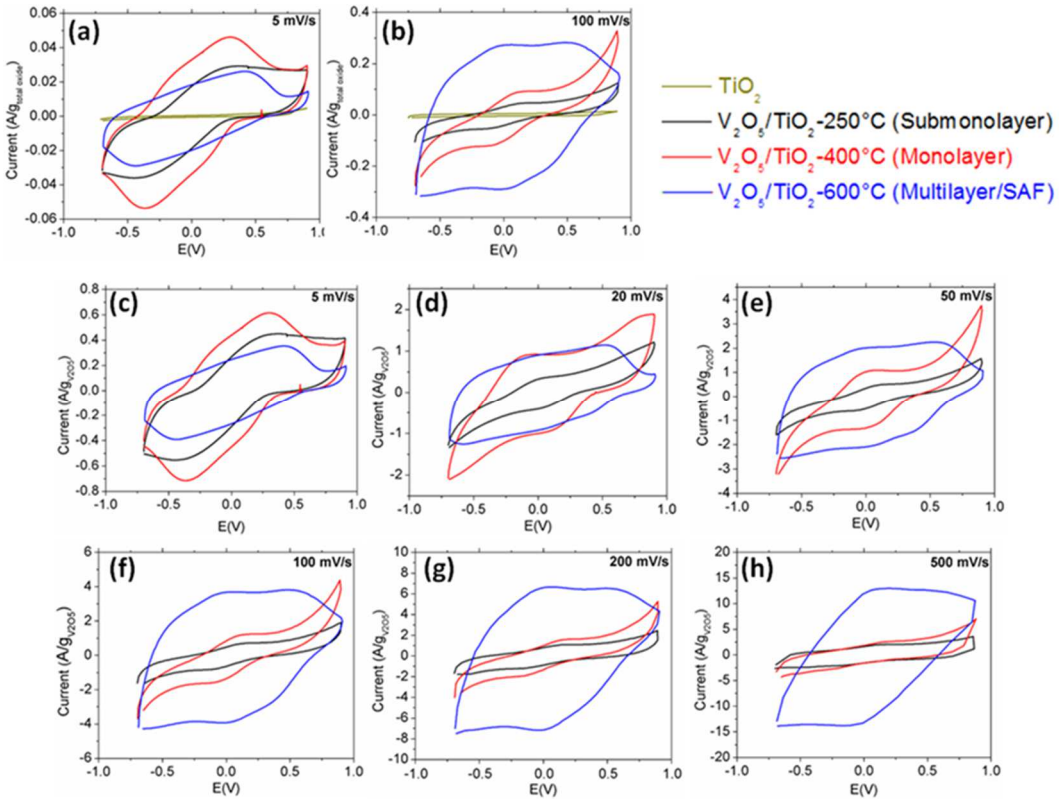

Figure 4.4 Cyclic voltammograms of pure TiO_2 nanoparticles and nanoparticles with 2-D surface vanadia phases, normalized to per gram of total oxide, measured at the scan rates of (a) 5 mV/s and (b) 100 mV/s in 0.1 M K_2SO_4 electrolyte. Cyclic voltammograms of three representative specimens, normalized per gram of vanadia, measured at the scan rates of (c) 5 mV/s, (d) 20 mV/s, (e) 50 mV/s, (f) 100 mV/s, (g) 200 mV/s, and (h) 500 mV/s in 0.1 M K_2SO_4 electrolyte, respectively. Additional data are reported for all six specimens equilibrated at 250, 400, 450, 500, 550 and 600 °C in Figures S1-S6 in the supporting information (and the data of only three representative specimens are displayed here for figure clarity).

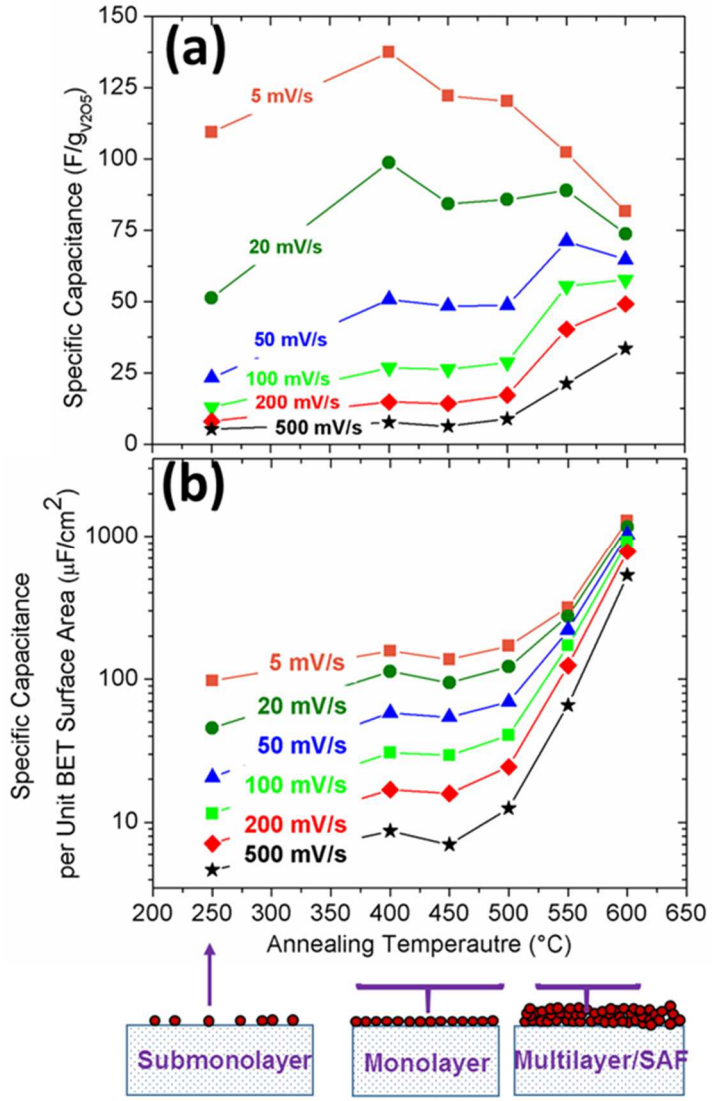

Figure 4.5 (a) Specific capacitance vs. the equilibration temperature curves, measured at six different scan rates in 0.1 M K_2SO_4 electrolyte. Configurations of 2-D surface vanadia phases formed at these equilibrated temperatures are schematically illustrated. (b) Measured specific capacitances per unit BET surface area of specimens annealed at different temperatures and tested at six different scan rates.

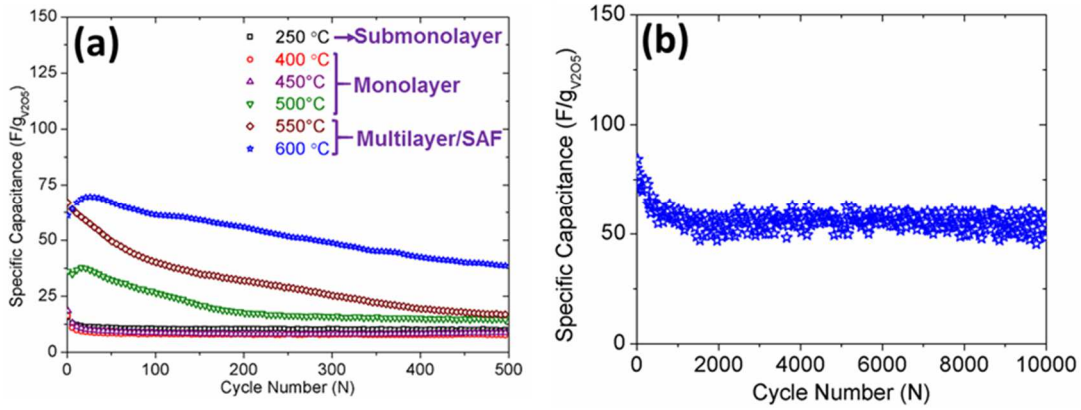

Figure 4.6 (a) Cycling stabilities of six different specimens (equilibrated at six different temperatures with three different types of 2-D surface vanadia phases) tested at a constant current of 600 mA/g in 0.1 M K_2SO_4. (b) Cycling stability of specimen with multilayer/SAF 2-D surface phase in an 8 M LiCl electrolyte, showing that the decaying of capacitance during cycling as a result of dissolution of vanadia in 0.1 M K_2SO_4 solution can be mitigated by using other types of electrolytes to reduce and prevent the dissolution of vanadia species.

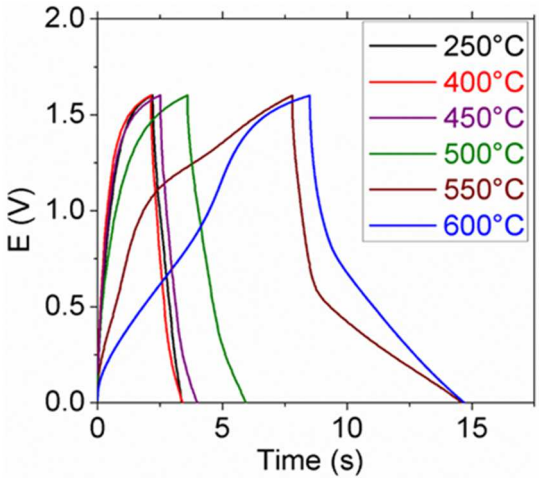

Figure 4.7 Comparison of galvanostatic constant current charge-discharge curves of different specimens annealed at different temperatures measured at 600 $mA/g_{total\ oxide}$ in 0.1 M K_2SO_4 electrolyte.

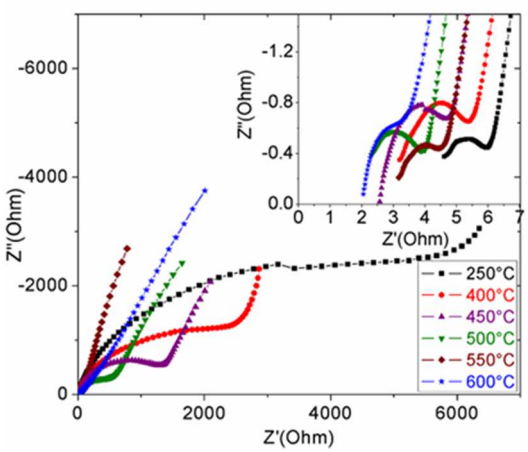

Figure 4.8 AC impedance plots of these six specimens. The inset shows the semi-circles for these six samples at high frequencies (in an expanded view near the origin point).

Table 4.1 Measured vanadium content (V:Ti atomic ratio measured from ICP), BET surface area, nominal surface coverage, and specific capacitance of six samples equilibrated at different temperatures with three different types of 2-D surface vanadia phases, measured at six different scan rates. Nominal surface coverages were estimated from measured V:Ti ratio and BET surface area, assuming spherical particles.

Annealing Temperature (°C)	V:Ti Atomic Ratio (ICP)	BET Surface Area (m^2/g)	Average Pore Size (nm)	Nominal Surface Coverage (# of V atom/nm^2)	Specific Capacitance ($^F/_{g_{V_2O_5}}$) Scan Rate =					
					5 mV/s.	20 mV/s.	50 mV/s.	100 mV/s.	200 mV/s.	500 mV/s.
250 (Submonolayer)	16.3	112.4	13.0	3.89	109.38	51.23	23.23	12.92	8	5.23
400 (Monolayer)	14.2	87.5	14.3	5.68	137.47	98.8	50.8	26.83	14.8	7.68
450 (Monolayer)	13.7	89.5	17.2	5.77	122.18	84.36	48.46	26.28	14.23	6.28
500 (Monolayer)	17.8	70.4	19.6	5.64	120.33	85.83	48.67	28.67	17.17	8.83
550 (SAF)	13.8	32.4	26.3	15.73	102.34	88.96	71.17	55.45	40.26	21.3
600 (SAF)	14.3	6.3	63.0	77.66	81.62	73.78	64.73	57.57	49.19	33.51

Chapter 5. Divalent-doped NASICON: Improving the ionic conductivity via simultaneously optimizing the phase and chemistry of the primary and secondary phases

NASICON is one of the most promising sodium solid electrolytes that can enable the assembly of cheaper and safer sodium all-solid-state batteries as alternative energy solutions to Li-ion batteries. Numerous dopants in NASICON have enhanced the total ionic conductivity above 1 mS/cm at room temperature. However, a fundamental understanding of how and why these dopants enhance the ionic conductivity is still lacking. In this study, we perform a combined experimental and computational investigation into the effects of aliovalent doping in NASICON on both bulk and grain boundary ionic conductivity. Our results show that the dopants with low solid solubility limits in NASICON solid solution lead to the formation of a conducting secondary phase at grain boundaries, thereby improving effective grain boundary conductivity that is otherwise hindered by the poorly-conducting Na_3PO_4 and ZrO_2 secondary phases in undoped NASICON. This is accompanied by a change in the Si/P ratio in the primary NASICON bulk phase, thereby transforming monoclinic NASICON to rhombohedral NASICON. Based on our findings, we have been able to synthesize NASICON chemistries with optimized total ionic conductivities in excess of 2 mS/cm. This study suggests a new general direction to improve the ionic conductivity of (possibly a variety of) solid electrolytes via simultaneously optimizing the primary bulk phase (via stabilizing a preferred phase and/or doping) and controlling the grain boundary segregation and secondary phase(s).

5.1. Introduction

The development of all-solid-state rechargeable alkali-ion batteries is an important step towards safer, higher energy density storage for large-scale applications such as automotive and grid storage. A key component in such an energy storage device will be the solid-state electrolytes with extremely high alkali ionic conductivities, also known as alkali superionic conductors, with room temperature conductivities in excess of 1 mS/cm being a typical target.

Among the known superionic conductors, the NAtrium Superlonic CONductor (NASICON) family of compounds, with general formula $Na_{1+x}Zr_2Si_xP_{3-x}O_{12}$ ($0 \leq x \leq 3$, and Zr can be substituted with other metals or mixture of metals), which has first been developed by Hong and Goodenough in 1976,[76,77] are arguably one of the most well-known and studied. Originally conceived as a replacement for β-alumina in high-temperature Na-S batteries, NASICON-based compounds have nevertheless garnered significant interest for low/room-temperature applications as electrodes and solid electrolytes for both Li and Na-ion rechargeable batteries.[78–81] Unlike sulfide solid electrolytes,[82–86] NASICONs are oxides, which are considerably more air and moisture stable.[87–90] However, the major challenge for NASICONs thus far are their typically moderate-to-low *total* (bulk plus grain boundary) ionic conductivities at room temperature (~0.1 mS/cm) due to the poorly-conducting ZrO_2 phases formed at grain boundaries.[91–95] Tetragonal Na_3PO_4 is another phase formed at grain boundaries of NASICONs with different synthesis procedures that has received much less attention in literature.[79,88]

There are two known phases of NASICONs – a rhombohedral $R\bar{3}c$ phase and a monoclinic C2/c phase that is formed, for example, by $Na_{1+x}Zr_2Si_xP_{3-x}O_{12}$ for $1.8 \leq x \leq 2.2$ at temperatures below 160 °C – that are related to each other by a small rotational distortion. Figure 5.1 shows the rhombohedral and monoclinic crystal structures, which comprises corner-sharing SiO_4/PO_4 tetrahedra and ZrO_6 octahedra. In the rhombohedral form, two distinct Na sites M_1 and M_2 form a 3D diffusion network, while the monoclinic distortion splits the M_2 sites into M_2^{α} and M_2^{β} sites.

Recently, there have been several efforts aimed at improving the ionic conductivity of NASICONs by aliovalent doping.[79,80,96] Jolley et al. studied the effect of aliovalent dopants (Ni^{2+}, Zn^{2+}, Al^{3+}, Fe^{3+}, Y^{3+}) on the ionic conductivity of NASICON. Although all dopants provided room temperature conductivities higher than undoped NASICON, only Co^{2+} doped NASICON provided a conductivity of higher than 1 mS/cm (1.55 mS/cm) at room temperature.[79] However, a Co-based NASICON is unlikely to be a good solid electrolyte candidate due to the redox active nature of Co metal. More recently, Ma et al. synthesized Sc^{3+}-doped NASICON that achieved an overall ionic conductivity of 4.0 mS/cm at room temperature, which is very similar to the value (3.7 mS/cm) obtained in a proprietary compound NASICON reported by Ceramatec,[80,97] although Sc is neither an earth-abundant nor a cost-effective doping element. Ma et al. attributed the improvement in bulk conductivity to a higher Na concentration in doped NASCION on account of substitution of Zr^{4+}

ions with M^{3+}/M^{2+} ions, and the enhancement in grain boundary conductivity to the improved microstructure from the solution-assisted solid-state synthesis procedure. However, the improvement in grain boundary conductivity can also be inferred from normalized Nyquist plots of aliovalent-doped NASICON synthesized by solid-state reaction method.[79]

In this work, we present a comprehensive experimental and first principles study of the effect of earth-abundant divalent dopants such as Mg^{2+} and Ni^{2+} on the ionic conductivity of NASICON $Na_{1+x}Zr_2Si_xP_{3-x}O_{12}$, with an emphasis on understanding the underlying mechanisms of conductivity improvements, particularly the interplays between doping, solubility, segregation, and formation of secondary phases. Unlike previously held assumptions, we will demonstrate conclusively that the NASICON structure has in fact limited solubility for divalent dopants, but higher solubility in the secondary precipitation phases at grain boundaries, such as Na_3PO_4. We show that instead, divalent dopants modify the primary-secondary phase equilibria by modifying the Si/P ratio (and consequently, the Na concentration and space group) in the bulk and creating diffusion-assisting defects in the secondary phase at grain boundaries. A maximum conductivity of 2.7 (± 0.3) mS/cm was achieved with a Mg-doped NASICON with Si/P ratio of 2.2 which should be a viable candidate solid electrolyte for room-temperature rechargeable all-solid-state sodium-ion batteries. These insights pave the way for further composition tuning of earth-abundant NASICON compounds. Moreover, this study

demonstrated the importance of simultaneous optimizing the primary (bulk) and secondary phases to achieve better overall performance, guided by the modeling of both phase formation and conductivity (vs. an overly-simplified assessment of the “doping” effect on conductivity via considering only the consequence of substituting cations in the primary bulk phase), which represents a strategy that should be generally adopted to improve other solid electrolytes.

5.2. Experimental Methods

5.2.1. Synthesis

NASICON specimens with a nominal composition of $Na_{3+2x}Zr_{2-x}M_xSi_2PO_{12}$ (M = Mg^{2+}, Ni^{2+}) were prepared by a solid-state procedure using Na_2CO_3 (Fisher Scientific, 99.5 %), ZrO_2 (Fisher Scientific, laboratory grade), SiO_2 (Alfa Aesar, 99.9%), $NH_4H_2PO_4$ (Sigma Aldrich, 99.99%), and MgO (Alfa Aesar, 99.95%) or NiO (Alfa Aesar, 99.998%) as precursors. The precursors were mixed using planetary ball mill in isopropanol for 24 h and then dried in an oven at 85 °C overnight. Calcination was performed at 1150 °C for 5 h with a heating rate of 5 °C/min in air. The calcined powders were manually ground using a pestle and mortar, followed by further grounding in a planetary ball mill in isopropanol for 48 h. The NASICON powders were then pressed using uniaxial pressing at about 2 metric tons (at a pressure of ~62 MPa) to form pellets of about 20 mm diameter and 3-4 mm thickness. Sintering was performed at 1230 °C and 1300 °C for 24 h with a heating rate of 5 °C/min for $Na_3Zr_2Si_2PO_{12}$ and $Na_{3.2}Zr_2Si_{2.2}PO_{12}$ series specimens, respectively. Pellets

were covered with synthesized NASICON powders of the same composition to reduce evaporation.

5.2.2. Characterization

X-ray diffraction (XRD) measurements of the specimens were performed using Cu K_α radiation to identify the crystalline phases. The microstructures of the cross sections of sintered pellets were observed using Scanning Electron Microscopy (SEM, FEI XL30) equipped with an energy-dispersive spectroscopy (EDS) analysis system (iXRF).

5.2.3. Conductivity measurement

Na-ion conductivity was measured with electrochemical impedance spectroscopy (EIS) using an impedance analyzer (Solartron 1255B) in the frequency range of 1 MHz to 1 Hz at 25, 0, -20, -40, -60 and -80 °C with Pt blocking electrodes sputtered on both sides of the pellets inside a temperature test chamber (LR Environmental Equipment Company) in air. Grain boundary, bulk and total conductivity were determined by fitting Nyquist plots (Figure 5.2 and 5.3) using the Z-View software (Scribner, Inc.). Activation energies for specific grain boundaries, bulk and total conductivities were determined from fitting Arrhenius plots (Figure 5.4 and 5.5).

5.3. Computational methods

5.3.1. Density functional theory calculations

All density functional theory (DFT) calculations were performed using Vienna Ab-initio Simulations Package (VASP)[98] within the Projector Augmented Wave (PAW) method. The Perdew-Burke-Ernzerhof (PBE) generalized gradient

approximation was used to model the exchange-correlation functional. A plane-wave cut-off of 520 meV was applied with a *k*-point mesh 4 × 4 × 2. An electronic energy tolerance of 5×10^{-5} eV/atom was used to relax the crystal structures. The Python Materials Genomics (pymatgen)[99] package was used for all input file generation and post-processing of results.

5.3.2. Diffusion energy barrier calculations for bulk undoped and doped NASICON

Vacancy diffusion barriers in a conventional NASICON cell were calculated using the climbing-image nudged elastic band (CI-NEB) method.[100] A Monkhorst-Pack *k*-point grid of 4 × 4 × 2 was used. Atomic positions were relaxed until forces were smaller than 0.02 eV/Å. Charge neutrality, where necessary, was maintained via a compensating background charge.

5.3.3. Ab initio molecular dynamics (AIMD) simulations of Na_3PO_4

Due to the disorder in cubic Na_3PO_4, the conductivity of Mg doped c-Na_3PO_4 was calculated using AIMD simulations. Non-spin-polarized AIMD simulations were conducted in the *NVT* ensemble at 800, 900, 1000, 1100, 1200 K. A plane-wave energy cutoff of 520 eV and Γ centered 1×1×1 *k*-point mesh was adopted with 2 fs time steps. An in-house AIMD workflow software[101,102] was used to automate the calculations. The diffusivity (*D*) of Na^+ was calculated using the equation:

$$D = \frac{1}{2dt}\langle[\Delta\vec{r}(t)]^2\rangle$$

where *d* is the dimensionality of diffusion; $[\Delta\vec{r}(t)]^2$ is the average mean square displacement (MSD) over a time duration *t*. The ionic conductivity, σ, is calculated using the Nernst-Einstein equation:

$$\sigma = \frac{\rho z^2 F^2}{RT} D_o e^{-\Delta E_a / kT}$$

where ρ is the molar density of diffusing Na ions in the unit cell; z = 1 is the charge of Na ions; *F* is the Faraday's constant; R is the gas constant and *T* is the temperature. D_o and ΔE_a are constants computed by fitting an Arrhenius relationship between diffusivities and temperatures. Room temperature diffusivity and conductivity were extrapolated from the computed quantities.

5.3.4. Dopant formation energy (E_f)

In order to determine which phase Mg segregates/dopes, we calculate the dopant formation energy, E_f, from first principles calculations. E_f is a measure of the thermodynamic energy cost function required to dope a host. It is defined as:

$$E_f = E_{doped} - E_{pristine} - \sum_{i=1}^{n} \mu_i N_i \qquad (1)$$

wherein, E_{doped} is the energy of the doped chemistry, $E_{pristine}$ is the energy of the undoped chemistry and μ_i is the chemical potential of the dopant. In the case of Mg doping of NASICON, we considered two possibilities:

(a) $Na_3Zr_2Si_2PO_{12}$ + 0.25 Mg + 0.5 Na → $Na_{3.5}Zr_{1.75}Mg_{0.25}Si_2PO_{12}$ + 0.25 Zr

(b) Na_3PO_4 + 0.25 Mg → $Na_{2.5}Mg_{0.25}PO_{12}$ + 0.5 Na

wherein, equation (a) is the doping reaction expected when Mg substitutes Zr in NASICON while equation (b) is the doping reaction when Mg substitutes Na in Na_3PO_4.

5.4. Results

5.4.1. Synthesis and phase identification

NASICON ($Na_3Zr_2Si_2PO_{12}$) doped with different nominal atomic concentrations (0-0.9 at. %) of Mg were synthesized using solid-state methods (see Methods section for details). Henceforth, all Mg concentrations refer to at. % of Mg per formula unit of $Na_3Zr_2Si_2PO_{12}$. It should be noted in this work, the term “doped” is used loosely to refer to NASICON synthesized with different overall atomic concentrations of Mg precursor added; as outlined in subsequent sections, both experimental and theoretical evidence demonstrate that the bulk NASICON crystal has limited solubility for Mg.

Figure 5.6(a) shows the X-ray diffraction patterns of the undoped and Mg-doped NASICONs. In agreement with previous experimental reports, Na_3PO_4 and ZrO_2 phases are the main impurities in undoped NASICON as well as Mg-doped NASICON specimens.[79] Slow-scan XRD experiments reveal that the peak correlated with monoclinic C2/c NASICON (at about 19 degrees) is evolving even at low Mg dopant concentrations (Figure 5.6(b)). The change in the shape of this peak has previously been used to study the phase transformation in NASICON from monoclinic (C2/c space group) to rhombohedral ($R\bar{3}c$ space group) at high temperatures. In addition, the intensity of the peak associated with cubic γ-Na_3PO_4 phase (at about 21 degrees)

increases with increasing nominal concentrations of Mg in the specimen (Figure 5.6(c)). A phase profile fitting of the XRD pattern reveals the three main phases formed in the 0.128 at. % Mg-doped specimen to be C2/c NASICON, ZrO_2 and Mg-doped γ-Na_3PO_4 (Figure 5.6(d)). Further increase in Mg concentration leads to transformation of the NASICON from the monoclinic to rhombohedral phase, eventually resulting in decomposition to $Na_4Zr_2(SiO_4)_3$, $NaMgPO_4$ and ZrO_2 phases in specimen at 0.9 at. % of Mg. A very similar trend is also observed in XRD patterns of Ni-doped NASICON specimens (Figure 5.7).

5.4.2. Microstructure analysis

Figure 5.8 shows an SEM image of the microstructure of 0.256 at. % Mg-doped NASICON. Three different phases with distinct contrasts are observed in the SEM images. The phase with a very bright contrast can be attributed to ZrO_2 phase. EDS analysis reveals that Mg is not uniformly distributed in these phases and is mostly segregated in a phase depleted of Si and enriched in Na. Due to the overlap of Zr L_α (2.04 KeV) and P K_α (2.02 KeV) lines, the EDS elemental maps of Zr and P looks identical therefore one elemental map is shown for P/Zr elements in Figure 5.8(e). The non-uniform distribution of Mg is also observed in specimen with lower concentration of Mg (0.128 at. %), as shown in Figure 5.9. These observations suggest that Mg has a low solubility in the NASICON structure, and instead tends to dissolute more (preferentially “segregate”) to the Si-poor secondary phase at grain boundaries. The non-uniform distribution of dopant is also observed in Ni-doped NASICON specimens (Figure 5.10).

To confirm these observations, we calculated the dopant formation energies of Mg in both the bulk phase ($Na_3Zr_2Si_2PO_{12}$) and the precipitation phase at grain boundaries (γ-Na_3PO_4) using DFT calculations. In the bulk $Na_3Zr_2Si_2PO_{12}$ phase, the Mg dopant is found to prefer the Zr site with the creation of charge-compensating Na interstitials, with a dopant formation energy of 1.12 eV for a Mg:O ratio of 0.0208. In the secondary γ-Na_3PO_4 phase that forms at grain boundaries, Mg substitutes for Na with the creation of vacancies with a lower dopant formation energy of 0.85 eV at a much higher Mg:O ratio of 0.0625. These DFT results suggest that Mg doping should preferentially dissolute (segregate) into the secondary γ-Na_3PO_4 precipitation phase at grain boundaries than the bulk $Na_3Zr_2Si_2PO_{12}$ phase, especially if Na loss during high temperature synthesis reduces the Na chemical potential, which would promote the formation of Na vacancies over Na interstitials.

5.4.3. Ionic Conductivity

Figure 5.11(a) shows the total ionic conductivity of Mg-doped NASICON (0-0.9 at. %) at room temperature (25 °C). The total ionic conductivity increases slightly at low concentrations of Mg reaching a maximum ionic conductivity of 2.05 mS/cm at 0.128 at. % of Mg and decreases with a further increase in the Mg concentration. The bulk conductivity, apparent grain boundary conductivity, and specific grain boundary conductivity determined via Brick Layer Model (BLM) are also shown in Figure 5.11(a). We may observe that bulk conductivity increases sharply with 0.064 at. % Mg doping, but remains constant with further increase in the Mg concentration. The grain boundary conductivity, on the other

hand, peaks at 0.128 at. % Mg, and decreases with higher Mg concentrations. These trends are also reflected in the bulk, grain boundary and total activation barriers for Na conduction (Figure 5.11(b)). The minimums in grain boundary and total activation barriers are observed at 0.128 at. % Mg, and increases with higher Mg concentrations.

5.4.4. Role of Mg doping on bulk and grain boundary conductivity: Hypotheses supported by AIMD modeling

From the results in the preceding sections, we may surmise that although Mg does not have significant solubility in the bulk $Na_3Zr_2Si_2PO_{12}$ phase, it nevertheless has a significant impact on both the bulk and grain boundary conductivities and activation energies. These seemingly contradictory observations can be reconciled by considering the effect of Mg on the synthesized primary (bulk) and secondary (grain boundary) phase equilibria. It is well-known that the NASICON structure exists in a range of compositions with formula $Na_{1+x}Zr_2Si_xP_{3-x}O_{12}$ with different Si/P ratios and correspondingly different Na concentrations. We therefore propose that the addition of the MgO precursor results in the formation of a bulk phase with a higher Si/P ratio (and higher Na concentration) and a Mg-doped Na_3PO_4 secondary phase.

To understand the role of Si/P ratio on the activation energy, we performed climbing image-nudged elastic band calculations (CI-NEB) to determine the alkali vacancy diffusion energy barriers for monoclinic NASICON $Na_{1+x}Zr_2Si_xP_{3-x}O_{12}$ for$1.75 \leq x \leq 2.25$. It has been well established that outside this range of Si concentration, NASICON chemistries have much lower ionic

conductivities.[76,103,104] Table 5.1 tabulates the vacancy diffusion energy barriers for NASICON chemistries with x = 1.75, 2.0 and 2.25. At x = 2, the maximum barrier along the percolating path (Figure 5.12) was found to be 183 meV. When P content is increased to 1.25 (x = 1.75), the energy barrier in the local environment increases significantly to 385 meV. Conversely, when the Si content is increased to x = 2.25, the barrier decreases slightly to 180 meV. The CI-NEB barrier plots can be found in Figure 5.13 and Figure 5.14. Thus, within the monoclinic range of Si concentration, it is important that molar concentration of Si must be higher than 2.0 to achieve maximum bulk conductivity.

To investigate the effect of Mg doping on the conductivity of the secondary γ-Na_3PO_4 phase (distributed at grain boundaries), *ab initio* molecular dynamics (AIMD) calculations were carried out on Mg-doped γ-Na_3PO_4 ($Na_{2.5}Mg_{0.25}PO_4$) as well as t-Na_3PO_4. Figure 5.15 shows the Arrhenius relationship of diffusivity with temperature for γ-$Na_{2.5}Mg_{0.25}PO_4$. The extrapolated bulk conductivity of $Na_{2.5}Mg_{0.25}PO_4$ at room temperature (300 K) is 0.047 mS/cm, and the predicted activation energy is 376 meV. In contrast, t-Na_3PO_4 exhibits negligible diffusivity even at 800-1200K in the AIMD simulations (Figure 5.16), and its activation energy has previously been reported to be ~760 meV.[105] The modest ionic conductivity of Mg-doped γ-Na_3PO_4 helps in decreasing the effective grain boundary resistance of Na diffusion in the GB as compared to the (insulating) secondary ZrO_2 and t-Na_3PO_4 phases in undoped NASICON GBs.

5.4.5. Experimental validation of hypotheses and synthesis of high-conductivity NASICON

To further confirm the above hypotheses experimentally, monoclinic NASICON with a higher nominal Si/P ratio of 2.2/0.8 were synthesized with and without Mg doping. The undoped NASICON, with a nominal formula of $Na_{3.2}Zr_2Si_{2.2}P_{0.8}O_{12}$, was found to have a bulk ionic conductivity of 5.66 mS/cm, slightly higher than that of undoped $Na_3Zr_2Si_2PO_{12}$ with Si:P ratio of 2 (5.06 mS/cm). Further, the maximum total ionic conductivity achieved in Mg-doped NASICON (Si-2.2 version: 2.7 mS/cm at 0.0625 at. % Mg) is about 30 % higher than the one achieved in Mg-doped NASICON (Si-2.0 version: 2.05 mS/cm at 0.125 at. % Mg). Note that the maximum total ionic conductivity in the Si-2.2 version is obtained at much lower concentration of Mg compared to the Si-2.0 version given that even a small depletion of P from the bulk into the secondary Na_3PO_4 phase at grain boundaries is likely to result in a change from the monoclinic structure to the lower-conductivity rhombohedral structure.[76] Similar synthesis of Ni doped NASICON with Si:P ratio of 2.2/0.8 was found to achieve a maximum ionic conductivity of 2.3 mS/cm, as shown in Figure 5.17.

5.5. Discussion

In this work, we demonstrated the synthesis of a high-conductivity monoclinic C2/c NASICON via the introduction of aliovalent dopants such as Mg^{2+} and Ni^{2+}. We present clear experimental and computational evidence that the effect of aliovalent dopants are more complex than that has been previously assumed. The commonly held assumption in previous works is that any dopants

introduced would sit in either the Zr^{4+} or Na^{+} sites, resulting in a modification of the bulk activation barriers and/or Na^{+} concentration. Our EDS results and calculated dopant formation energies suggest that dopants are more likely to incorporate into a secondary phase at grain boundaries, such as Na_3PO_4, and any effect on the bulk activation barriers result from changes in the Si:P ratio within the bulk. Indeed, CI-NEB calculations confirm the lowering of the bulk activation barriers with increase in Si/P ratio, subject to the restriction that Si/P must be less than 2.2 to prevent transformation to the lower-conducting rhombohedral phase. This is consistent with previous experimental results by Ahmad et al. reporting maximum room temperature bulk ionic conductivity for the NASICON for a Si/P ratio of 2.2/0.8.[103] On the other hand, CI-NEB calculations performed on Mg-doped NASICON (where Mg is assumed to sit in the Zr site) find that bulk activation barriers in the vicinity of the dopant increases significantly from 183 meV to 407 meV (Figure 5.18(a)), directly contradicting previously held assumptions that aliovalent dopants decrease the bulk activation energies. Similarly, CI-NEB calculations performed on Ni-doped NASICON also shows that the activation energy increases to 458 meV in the vicinity of the dopant (Figure 5.18(b)).

Though the introduction of aliovalent dopants does have an indirect effect on the bulk conductivity by modifying the Si/P ratio, it has a far more important effect on the effective grain boundary conductivity. Like many oxide superionic conductors, the bulk conductivity is not the limiting bottleneck in the NASICON phases, and bulk conductivities in excess of 1 mS/cm have been reported by

Ahmad et al. since 1987.[103] The EIS results in this work (Figure 5.11) clearly show a substantial improvement in the effective grain boundary conductivity upon doping, which is validated by AIMD simulations showing significant improvement in the conductivity of the secondary phase at grain boundaries. Indeed, it is our belief that similar effects are present in previous reports of enhanced total conductivity in NASICON with other dopants such as Sc^{3+} and Y^{3+}.[79,97,106] Table 5.2 shows the dopant formation energies in the bulk NASICON and the predicted secondary phase (that presumably precipitates at grain boundaries) for these dopants; similarly, a higher dopant solubility is predicted for the secondary phase compared to the primary bulk phases.

It should be noted that during the course of this manuscript preparation, a very recent report of Mg-doped NASICON published, claiming a conductivity of 3.5 mS/cm at room temperature for a low doping level of 0.05 at. % Mg;[107] however, our measurements showed that specimens with a similar composition (0.064 at. % Mg) only have conductivity of ~ 1.3 mS/cm, which we believe to be a more reasonable value since at these low doping concentrations, the nominal concentration of Na is lower than undoped NASICON (Si-2.2 version). In addition, the conductivity of undoped NASICON is not reported in that study, making it difficult to assess the actual improvement upon doping and effects of other factors. We also notice an unusual high contact resistance (120 Ω) in the Nyquist plot in that report,[107] which should have been deducted from total resistivity to calculate the conductivity of Mg-doped NASICON, but may cause

some measurement errors. Moreover, authors attributed the improvement in conductivity to the increased bottleneck size (being related to a pseudo-hexagonal ring consisting of alternating three ZrO_6 octahedra and three SiO_4/PO_4 tetrahedra) for ion conduction, which is likely an overly-simplified explanation. While isovalent doping can be purely attributed to structural changes,[108] it is generally believed that the effects of aliovalent doping on conductivity involves complex interactions of an increased concentration of mobile species, as well as modified electronic density and framework structure, albeit the additional (yet important) effects on solubility, phase transformation, and secondary phase discovered in this study. For example, a recent study of Al-doped $LiTi_2(PO_4)_3$[109] has shown that the activation energy along the diffusion pathway actually increases in the vicinity of the dopant. Our CI-NEB calculations performed on Mg/Ni-doped NASICON (where Mg/Ni is assumed to sit in the Zr site) also finds that bulk activation barriers in the vicinity of the dopant increases significantly as discussed above. Similar to previous reports,[80] a high GB conductivity was also reported, for which the authors did not provide any explanation.[107]

Separating the bulk and GB conductivities, we have shown that the effective GB conductivity of Mg-doped NASICON is also improved in comparison with undoped NASICON. Such improvements in the GB conductivity of aliovalent-doped NASICON has been observed previously (in the normalized Nyquist plots in Figure 1(a) and (b) in reference 79 and Table 2

in reference 80); but, unfortunately, these observations have not been fully recognized and elaborated in previous studies.[79,80] The high GB resistivity of NASICON is mostly attributed to the secondary ZrO_2 phase precipitated at GBs due to evaporation of Na and P during high temperature synthesis and sintering of NASICON.[93–95] However, the ZrO_2 phase is also reported to form in NASICON sintered by Field Assisted Sintering Technique (FAST) with very short exposure to high temperatures.[110] It is difficult to separate out the GB and bulk conductivity at high temperatures for superionic conductors due to electrode effects and inductions from connections and measurement cell.[111] A similar behavior, i.e., a very low resistivity of grain boundaries at high temperatures and high resistivity at intermediate and low temperatures, was reported for NASICON.[93,104] Na_3PO_4 is another phase that often precipitate at grain boundaries of NASICON. Its cubic phase (γ phase) stabilized at high temperatures is considered as solid electrolyte for high temperature applications (Na-S batteries)[105,112–114], while its low-temperature phase (tetragonal Na_3PO_4) has an extremely low ionic conductivity at intermediate and low temperatures. The low conductivity is attributed to the compact crystal structure of Na_3PO_4 and low concentrations of Na vacancies. As shown in this work, aliovalent dopants such as Mg^{2+} tend to displace Na in the secondary Na_3PO_4 phase at grain boundaries, creating Na vacancies. We further speculate that this Na displacement from the GB phase results in the injection of Na into the vacant sites in the NASICON crystal structure. This is somewhat analogous to previously investigated mixed-phase ionic conductors show a higher ionic

conductivity than those of the parent phases in Ag^+ ionic conductors[115,116] and in F^- ion conductors[117–119]. It is possible that a unilateral distribution of charge carrier (Na^+) from Mg-doped Na_3PO_4 phase into vacant sites in NASICON structure that improves the ionic conductivity of NASICON. Comparing normalized Nyquist plots at 25 °C for Mg 0.128 at. % and Mg 0.256 at. % specimens (Figure 5.2), it is obvious that both bulk and grain boundary conductivity decreases at higher concentrations due to coarsening of Mg-doped Na_3PO_4 phase. This is presumably due to 1) a depletion of P in the primary NASICON bulk phase and formation of $R\bar{3}c$ NASICON that decreases the bulk conductivity and 2) a decrease in volume fraction of NASICON/Mg-doped Na_3PO_4 interface. The conductivity drop at high concentrations of aliovalent-doped NASICON (Sc^{3+}-doped NASICON)[80] was previously attributed to decrease in Na vacant sites in NASICON structure; we speculate that the maximum conductivity achieved in Mg-doped NASICON is limited by size and distribution of secondary Mg-doped Na_3PO_4 phase at grain boundaries in NASICON, following to a percolation theory for composite ionic conductors.

It is also possible that a Na_3PO_4-based, nanoscale, interfacial phase formed in doped NASICON materials, serving as an additional reason for improved effective grain boundary conductivity. A similar case has been reported previously, where the formation of 1-4 nm-thick, LaP_3O_9-based, interfacial phases at grain boundaries in $LaPO_4$ increased the proton conductivity by more than 10 times.[120] Moreover, the formation of $Li_4P_2O_7$- or

Li_3PO_4-based nanoscale surface phases have been shown to improve the rate capabilities of Li-ion batteries,[22,42] pseudocapacitors[121] and a similar surface phase was recently found to improve the oxygen ionic conductivity of nanofibers by more than 1000 times.[43] See a recent review for relevant discussion.[122] Unfortunately, these NASICON materials are extremely sensitive to electron and ion beams, preventing us from making good TEM specimens for direct atomic-resolution characterization of grain boundaries. Thus, it is impossible to confirm whether a similar Na_3PO_4-based, nanoscale interfacial phase formed and played a role in improving the grain boundary ionic conductivity in the current study; further discussion is unwarranted at this time.

Finally, this work suggested that there are significant opportunities to improve both bulk and grain boundary conductivity of solid electrolytes via controlling the microstructure (e.g., the size and distribution of the secondary phase precipitated at grain boundaries) as well as interfacial engineering. In addition, prior studies have been successfully taken advantages of two-dimensional heterostructures[1] or textured columnar grains[123] to achieve much improved conductivities along one direction, and similar levels of controlled (well-defined) hetero-phase structures or interfaces (possibly with nanostructures) may help to achieve even higher Na ionic conductivity for Mg/Ni doped NASICON. The assembly of this and early studies collectively suggest the important opportunities to achieve superior ionic conductivities via control

microstructure and interfaces, in addition to the phase and doping of the primary bulk phases.

5.6. Conclusion

To summarize, we have studied the effects of aliovalent doping on both bulk and GB conductivity of NASICON using both experimental and computational techniques. Based on these studies, Mg and Ni doped NASICONs with the optimized total ionic conductivities of 2.7 mS/cm and 2.1 mS/cm, respectively, were synthesized. Our results show that dopants have a higher tendency to form a Na_3PO_4-based secondary phase at grain boundaries with higher concentrations of the Mg or Ni dopant. This simultaneously leads to a change in the Si/P composition in the bulk phase, which increases the bulk ionic conductivity initially (but eventually ending up with lower conducting $R\bar{3}c$ phase NASICON with high doping level). More importantly, the dopant containing Na_3PO_4-based secondary phase formed at grain boundaries reduces the effective grain boundary resistance, thereby increasing the total ionic conductivity. This study suggests significant opportunities to improve the total conductivity via controlling the phase and chemistry of both the primary and secondary phases via doping as well as the interfaces and microstructure.

Chapter 5, in full, is a reprint of the material currently under review for publication “Divalent-doped NASICON: Improving the ionic conductivity via simultaneously optimizing the phase and chemistry of the primary and secondary phases” Mojtaba Samiee, Balachandran Radhakrishnan, Zane Rice,

Zhi Deng, Ying Shirley Meng, Shyue Ping Ong, Jian Luo. The dissertation author was the co-primary investigator and wrote majority part of this paper excluding theoretical calculations.

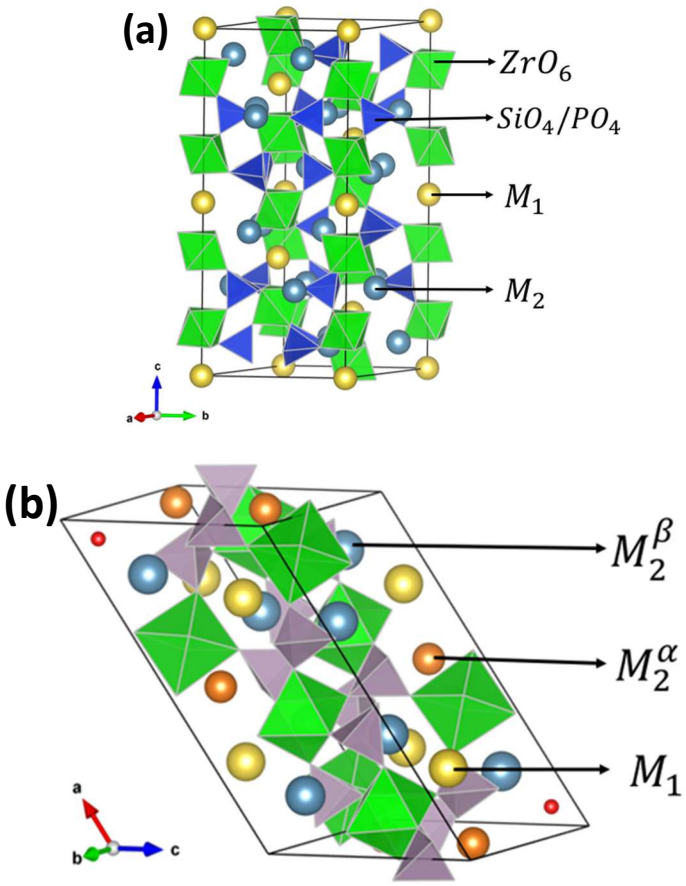

Figure 5.1 Conventional unit cells of NASICON. (a) Rhombohedral structure (b) Monoclinic structure. The rhombohedral structure has two distinct Na^+ sites: M_1 and M_2. The local Si/P environment and the monoclinic distortion splits the M_2 sites into two different sites: M_2^{α} and M_2^{β} labeled in the figure.

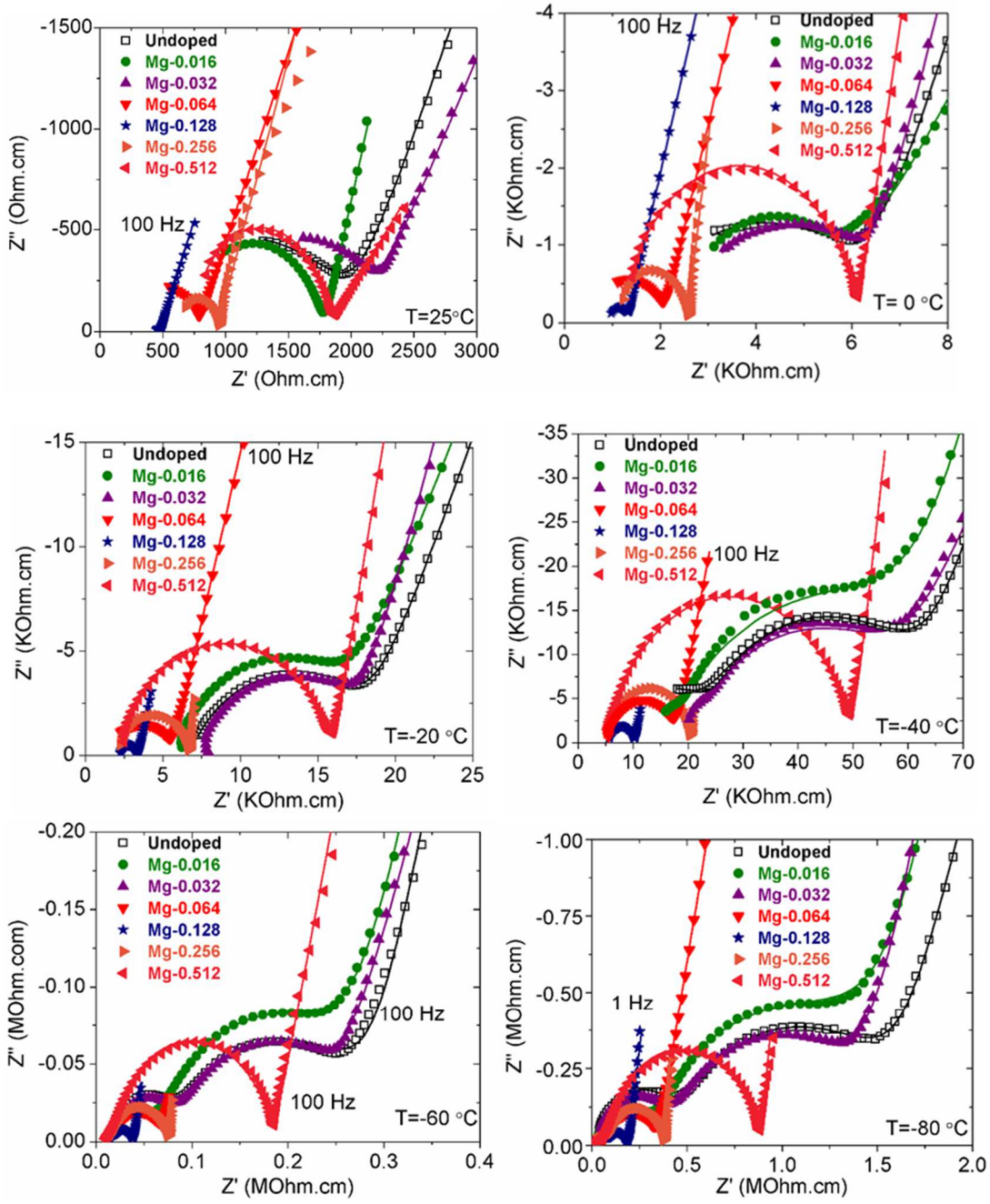

Figure 5.2 Nyquist plots of undoped and Mg-doped NASICON ($Na_3Zr_2Si_2PO_{12}$) along with fitted results (solid lines) at different temperatures.

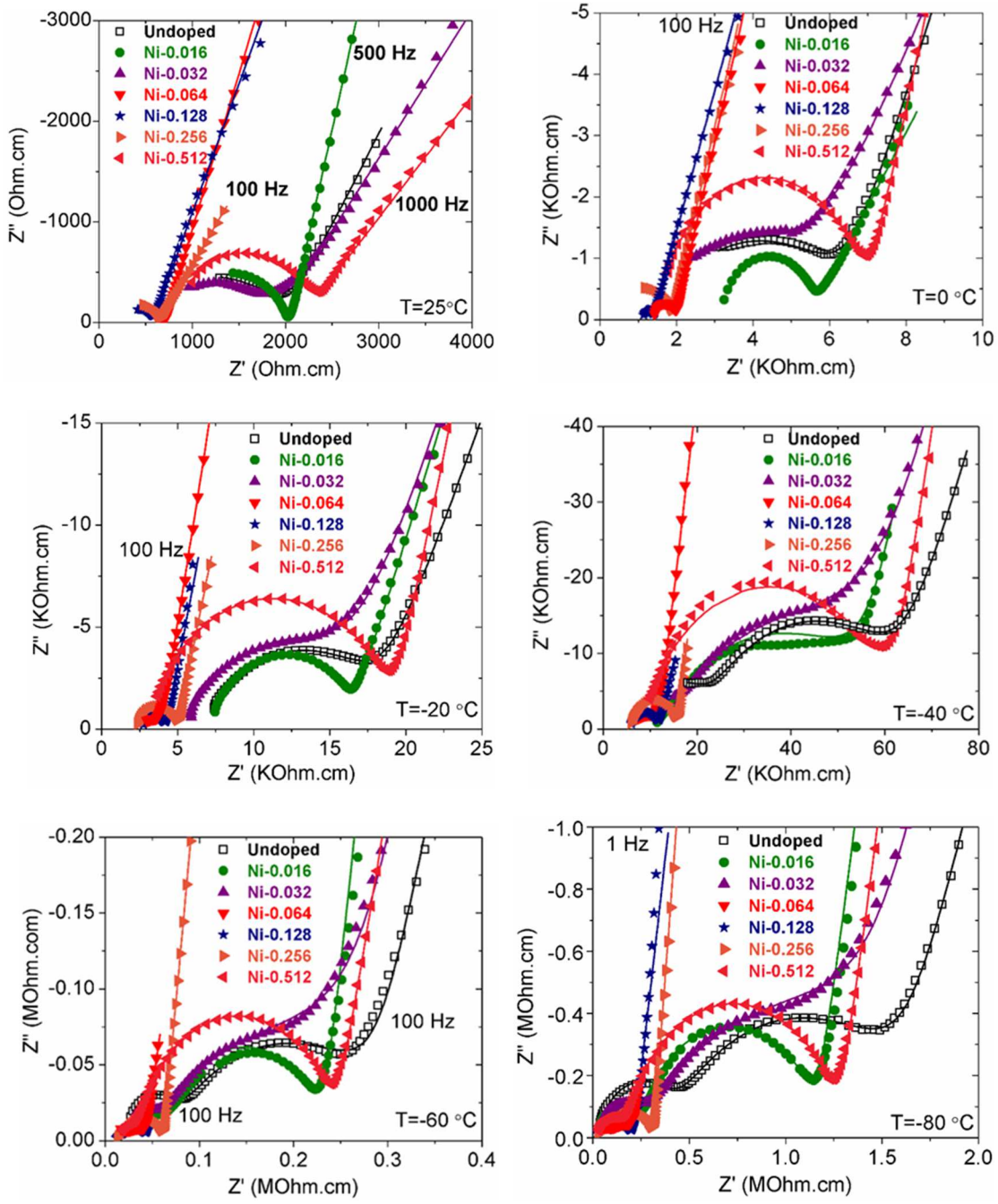

Figure 5.3 Nyquist plots of undoped and Ni-doped NASICON ($Na_3Zr_2Si_2PO_{12}$) along with fitted results (solid lines) at different temperatures.

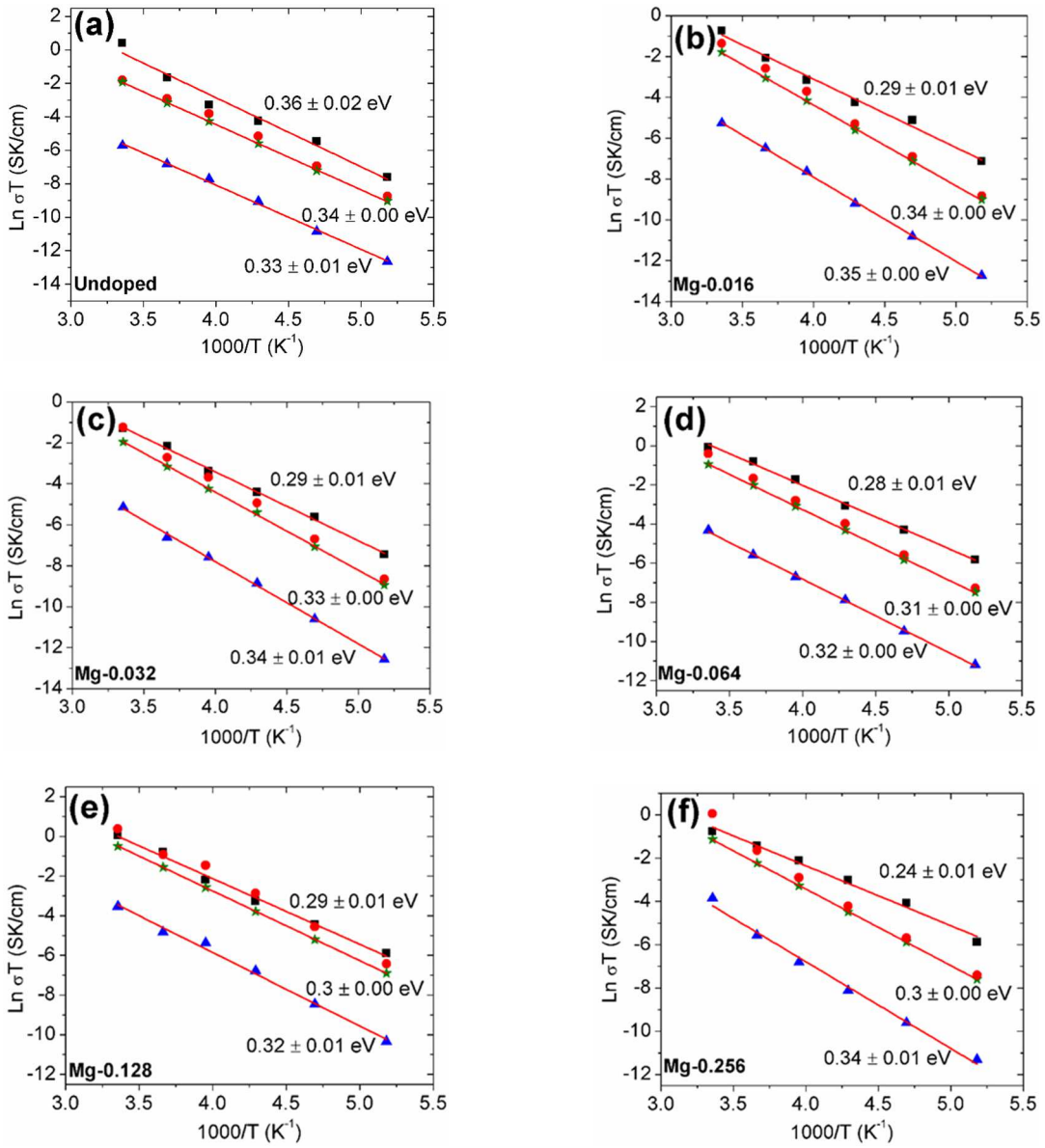

Figure 5.4 Arrhenius plots for bulk conductivity (black squares), total conductivity (green stars), grain boundary conductivity (red circles) and specific grain boundary conductivity (blue triangles) for (a) undoped and Mg-doped NASICON ($Na_3Zr_2Si_2PO_{12}$) with atomic percentage of (b) 0.016, (c) 0.032, (d) 0.064, (e) 0.128 and (f) 0.256.

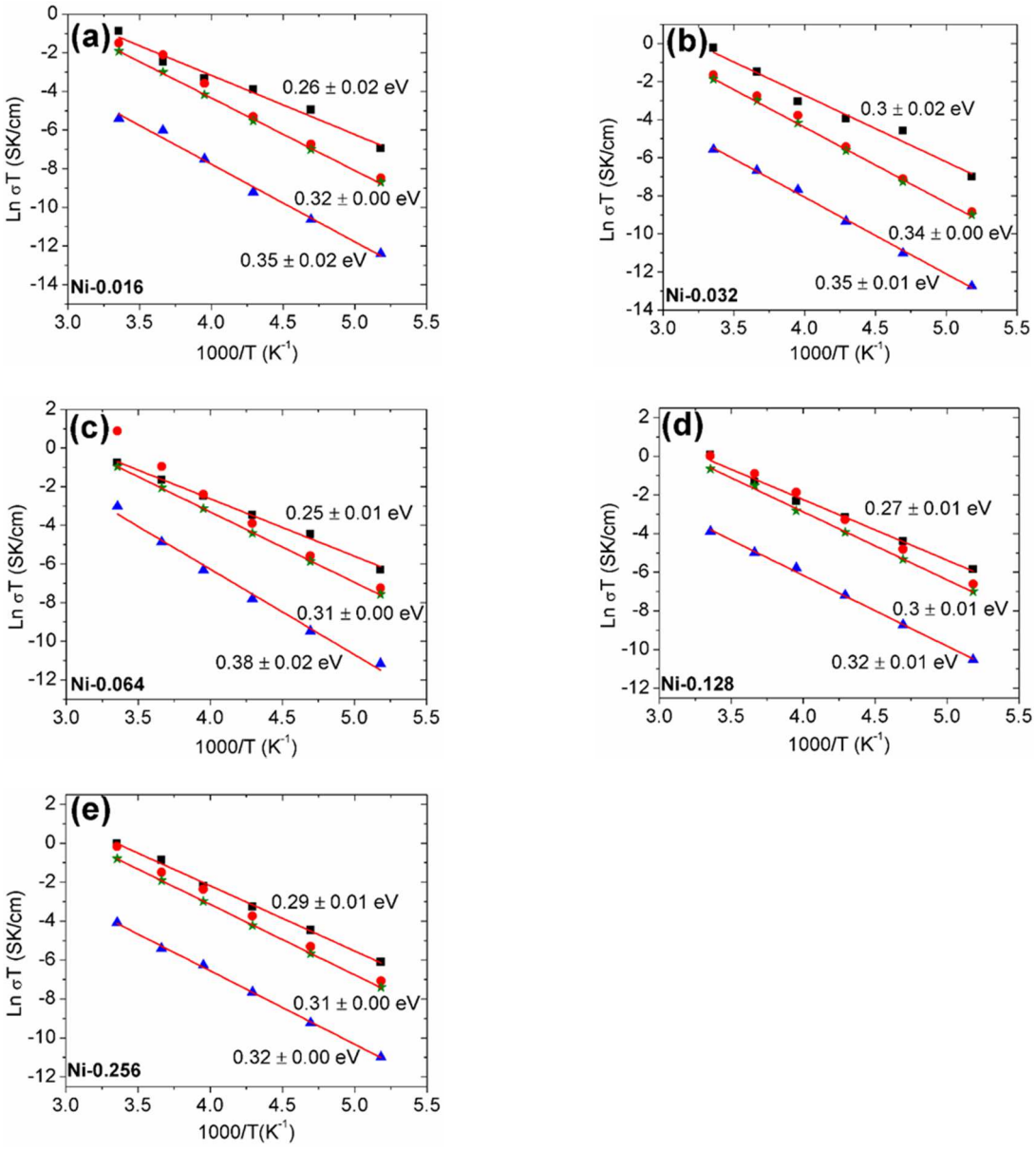

Figure 5.5 Arrhenius plots for bulk conductivity (black squares), total conductivity (green stars), grain boundary conductivity (red circles) and specific grain boundary conductivity (blue triangles) for Ni-doped NASICON ($Na_3Zr_2Si_2PO_{12}$) with atomic percentages of (a) 0.016, (b) 0.032, (c) 0.064, (d) 0.128 and (e) 0.256.

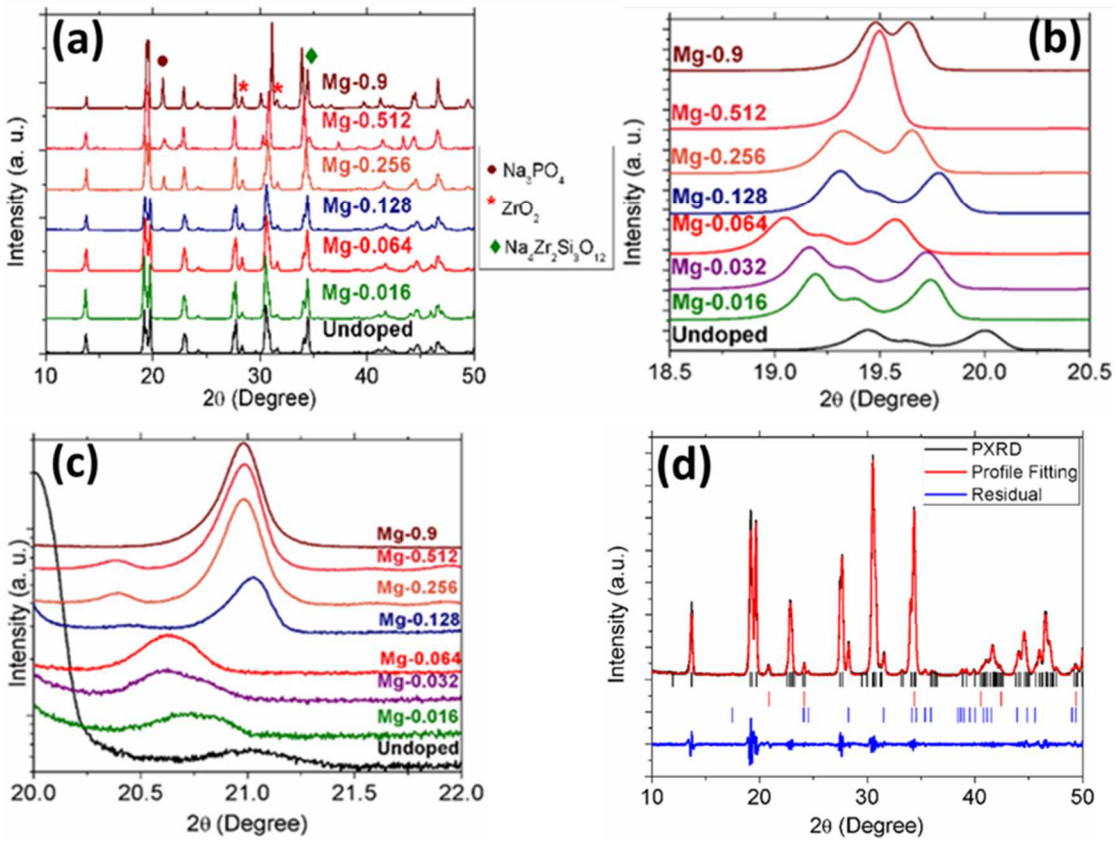

Figure 5.6 Phase identification of undoped and Mg-doped NASICON. (a) XRD pattern of undoped and Mg-doped NASICON with different atomic percentages of Mg; (b) High-resolution XRD patterns showing the evolution of NASICON crystal structure from C2/c (monoclinic) to $R\bar{3}c$ space group (rhombohedral) in Mg-doped NASICON specimens with different Mg concentration; (c) High-resolution XRD patterns showing the Na_3PO_4 phase peak in undoped and Mg-doped NASICON specimens with different Mg concentration; (d) Phase profile fitting of Mg-doped NASICON ($Na_{3.256}Mg_{0.128}Zr_{1.872}Si_2PO_{12}$) representing three main phases formed: C2/c NASICON, ZrO_2 and Mg-doped γ-Na_3PO_4.

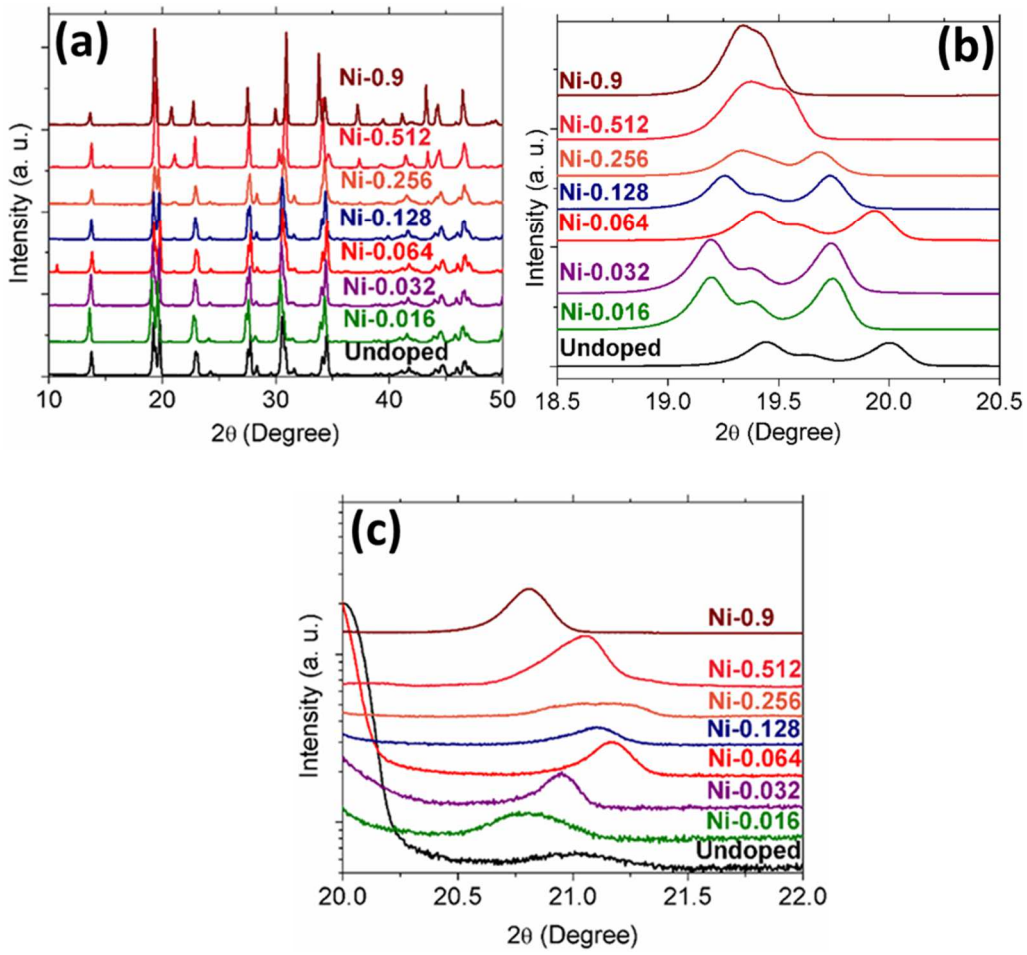

Figure 5.7 Phase identification of undoped and Ni-doped NASICON. (a) XRD pattern of undoped and Mg-doped NASICON with different atomic percentages of Ni; (b) High-resolution XRD patterns showing the evolution of NASICON crystal structure from C2/c (monoclinic) to $R\bar{3}c$ space group (rhombohedral) in Ni-doped NASICON specimens with different Ni concentration; (c) High-resolution XRD patterns showing the Na_3PO_4 phase peak in undoped and Ni-doped NASICON specimens with different Ni concentration.

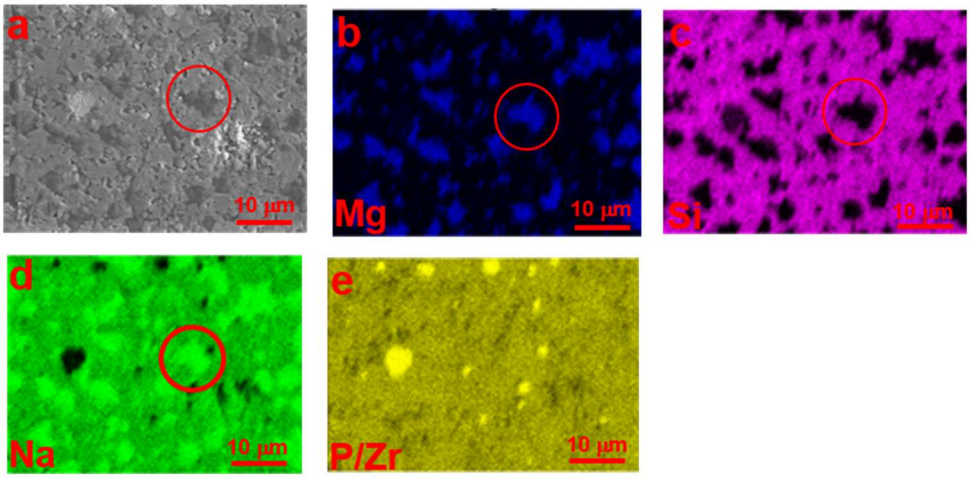

Figure 5.8 (a) SEM image of Mg-doped NASICON ($Na_{3.512}Mg_{0.256}Zr_{1.744}Si_2PO_{12}$), along with individual EDS maps for (b) Mg, (c) Si, (d) Na, (e) P/Zr. Due to the overlap of Zr L_α (2.04 KeV) and P K_α (2.02 KeV) lines, the EDS elemental maps of Zr and P looks identical.

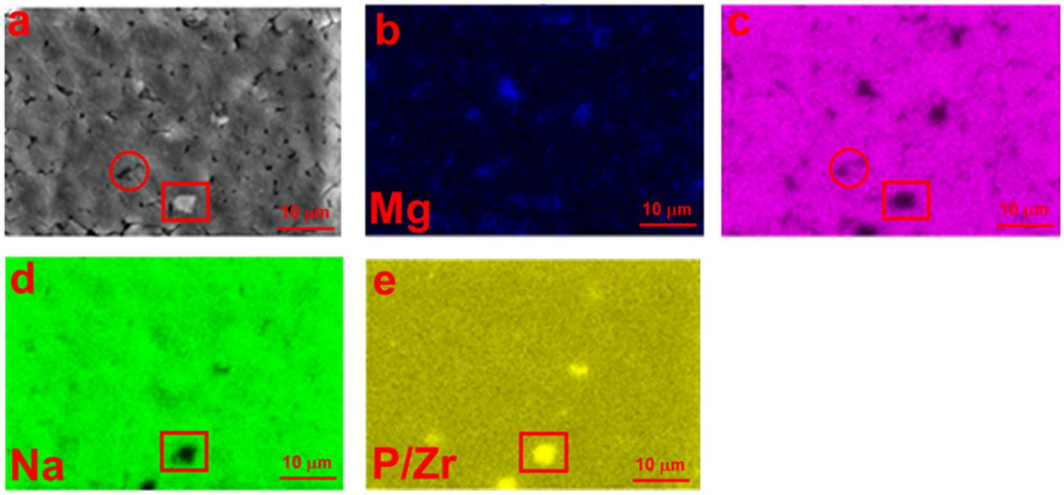

Figure 5.9 (a) SEM image of Mg-doped NASICON ($Na_{3.256}Mg_{0.128}Zr_{1.872}Si_2PO_{12}$) along with individual EDS maps for (b) Mg, (c) Si, (d) Na, (e) P/Zr elemental maps. Due to the overlap of Zr L_α (2.04 KeV) and P K_α (2.02 KeV) lines, the EDS elemental maps of Zr and P looks identical.

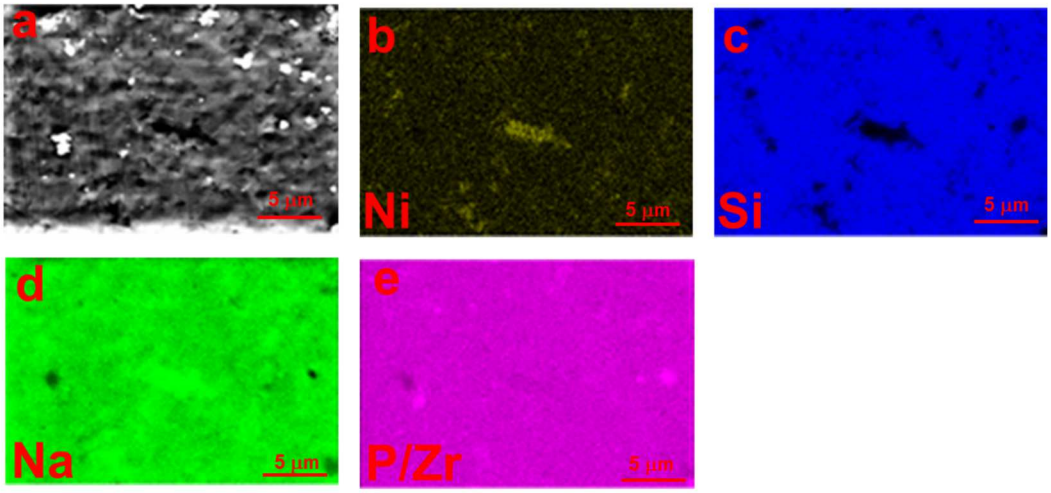

Figure 5.10 (a) SEM image of Ni-doped NASICON ($Na_{3.128}Ni_{0.064}Zr_{1.936}Si_2PO_{12}$) along with individual EDS maps for (b) Ni, (c) Si, (d) Na, (e) P/Zr elemental maps. Due to the overlap of Zr L_α (2.04 KeV) and P K_α (2.02 KeV) lines, the EDS elemental maps of Zr and P looks identical.

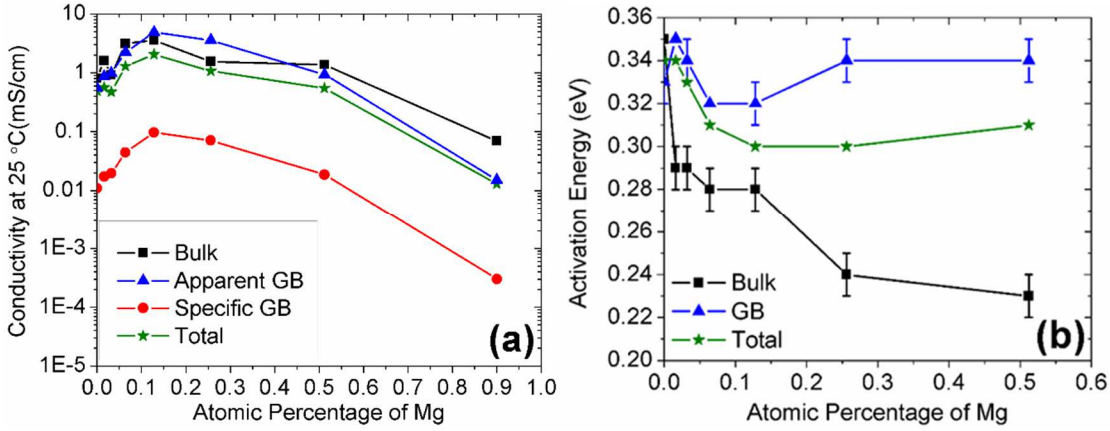

Figure 5.11 (a) Bulk, apparent GB conductivity, specific GB conductivity and total ionic conductivity at room temperature (25 °C) for undoped and Mg-doped NASICON ($Na_3Zr_2Si_2PO_{12}$ based series). The estimated errors of conductivities are ± 10%. (b) Activation energies of grain boundary, bulk and total conductivities for undoped and Mg-doped NASICON ($Na_3Zr_2Si_2PO_{12}$ based series). Error bars are standard errors based on 95% confidence level.

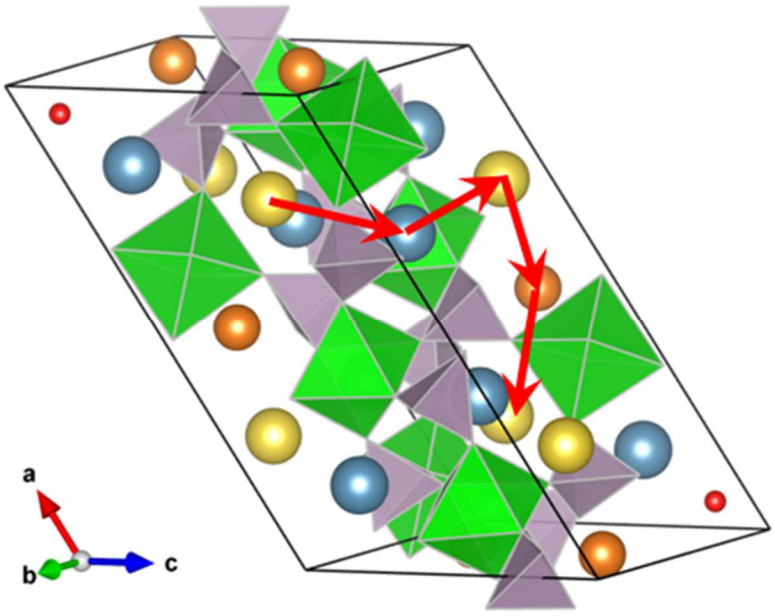

Figure 5.12 3D percolating diffusion pathway in the monoclinic NASICON. The diffusion pathway can be represented as M_1-M_2^{α}-M_1-M_2^{β}-M_1 shown by the red arrow.

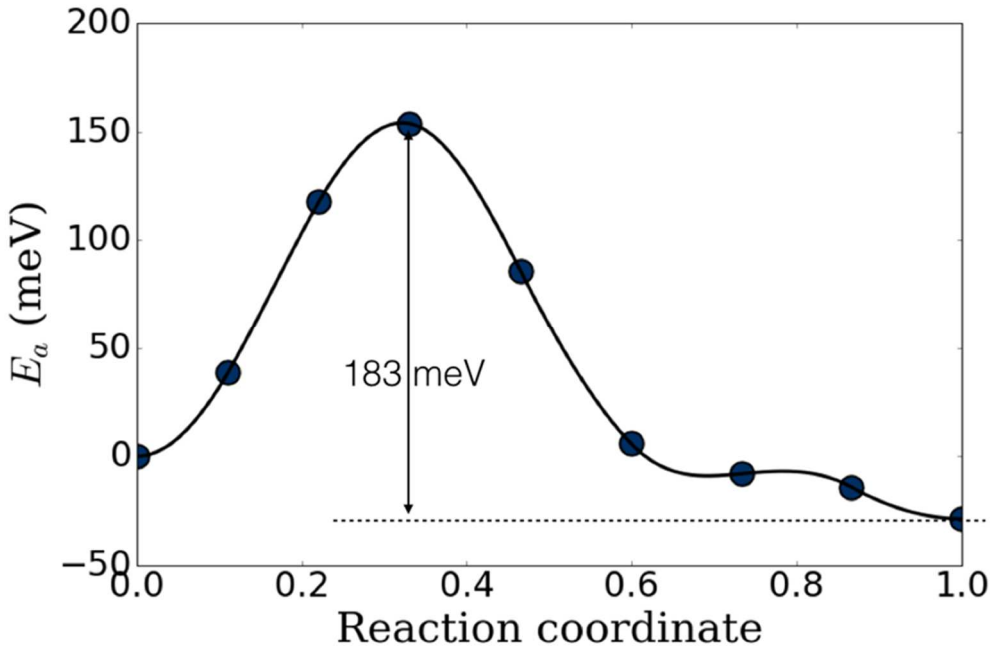

Figure 5.13 Vacancy barrier energy in $Na_3Zr_2Si_2PO_{12}$ computed from CI-NEB calculations. The barrier plotted corresponds to the maximum barrier along the percolating pathway shown in Figure 5.12.

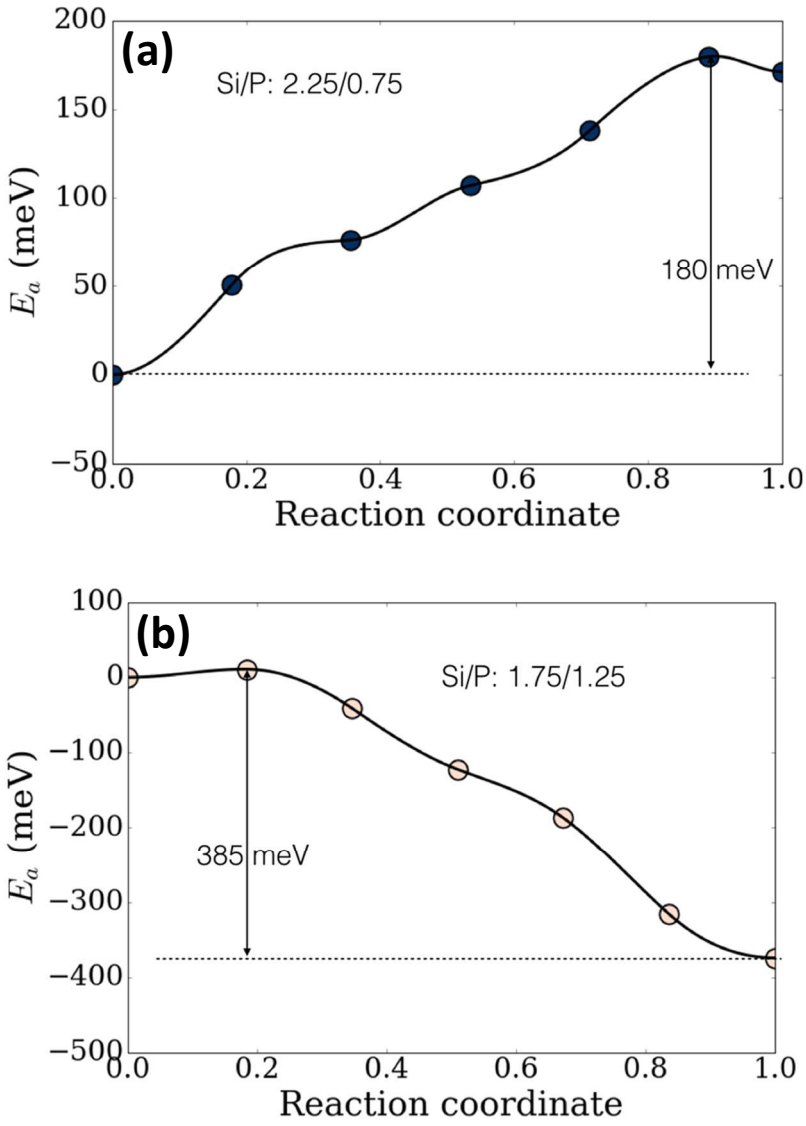

Figure 5.14 Vacancy barrier energy in (a) $Na_{3.25}Zr_2Si_{2.25}P_{0.75}O_{12}$ and (b) $Na_{2.75}Zr_2Si_{1.75}P_{1.25}O_{12}$ computed from CI-NEB calculations. The calculated barriers correspond to the paths that are influenced by the introduction of Si and P as compared to $Na_3Zr_2Si_2PO_{12}$ to achieve the Si-excess and P-excess chemistries respectively. In the P-excess case, no vacancy was introduced as the P substitution of Si led to creation of a vacant site.

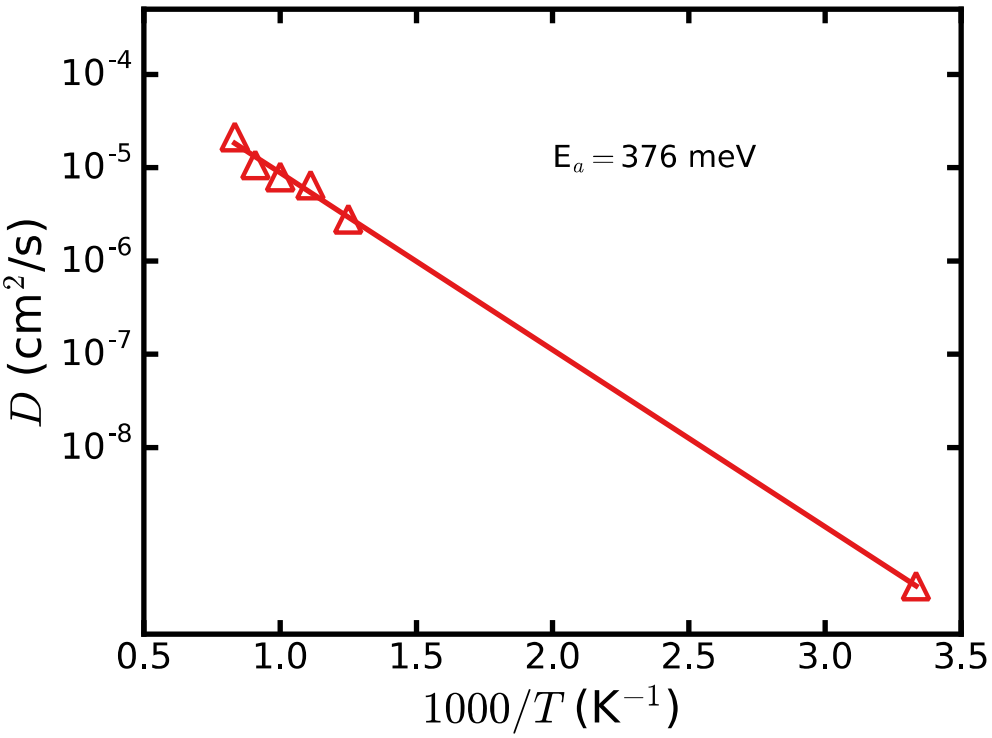

Figure 5.15 Arrhenius plot of diffusivity in $Na_{10}MgP_4O_{12}$ computed from *ab initio* molecular dynamics. Simulations were performed at 800, 900, 1000, 1100 and 1200 K with room temperature diffusivity being calculated via extrapolation.

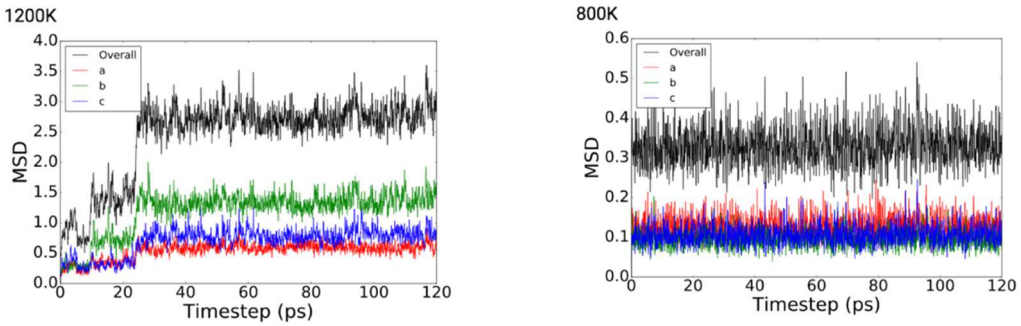

Figure 5.16 Mean square displacement plots of Na^+ ions from AIMD simulations of t-Na_3PO_4. The low displacements at 800 and 1200 K show that undoped t-Na_3PO_4 has extremely low ionic conductivity.

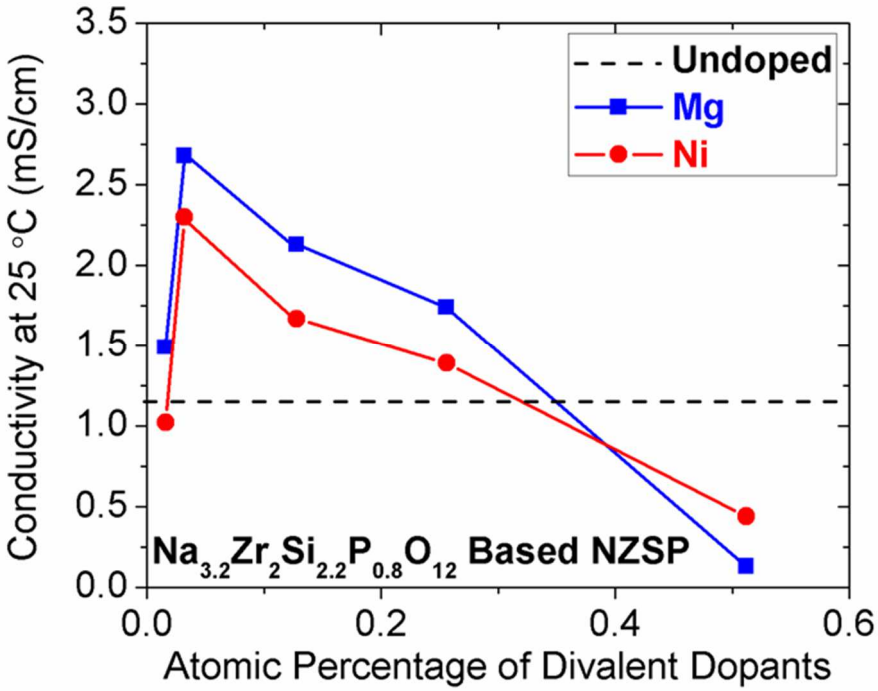

Figure 5.17 Total ionic conductivity at room temperature (25 °C) of undoped and doped (Mg/Ni) NASICON ($Na_{3.2}Zr_2Si_{2.2}P_{0.8}O_{12}$) with different atomic percentages of Mg/Ni.

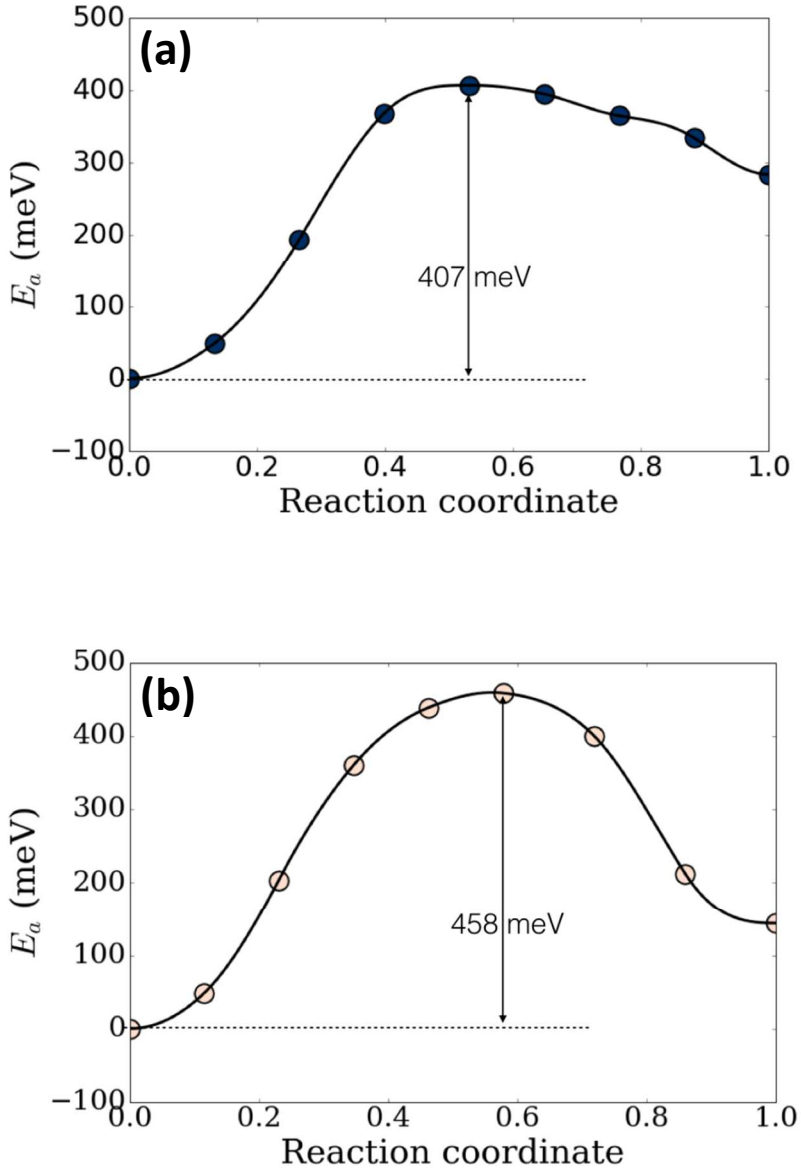

Figure 5.18 Vacancy barrier energy in (a) $Na_{14}Zr_7MgSi_8P_4O_{48}$ and (b) $Na_{14}Zr_7NiSi_8P_4O_{48}$ computed from CI-NEB calculations in the vicinity of the Mg/Ni dopant. Other diffusion pathways are assumed to remain the same as in in $Na_3Zr_2Si_2PO_{12}$.

Table 5.1 Climbing Image Nudged Elastic Band (CI-NEB) calculation of vacancy diffusion barriers in NAICON chemistries. Si/P compositions of 1.75/1.25 and 2.25/0.75 were constructed from the structure of Si/P: 2.0/1.0 by substituting one Si/P in $Na_{12}Zr_8Si_8(PO_{12})_4$ accompanied by the addition of vacancy/Na^+ appropriately. In the case of Si/P: 2.25/0.75 and Si/P:1.75/1.25, the barriers were computed in the vicinity of the substituted Si/P as compared to the nominal composition of Si/P:2.0/1.0. It is assumed that the other paths in the framework are not affected by the introduction of Si/P and the accompanying Na+/vacancy respectively.

Si/P Composition	Si/P: 1.75/1.25	Si/P: 2.0/1.0	Si/P: 2.25/0.75
CI-NEB Barrier (meV)	385	183	180

Table 5.2 Dopant formation energy in $Na_{3.25}Zr_{1.75}M_{0.25}Si_2PO_{12}$, predicted grain boundary phase containing the dopant and their formation energies. NASICON, in general, has Na_3PO_4 and ZrO_2 as grain boundary (GB) products. Formation energies presented here are based on first principles computations of the Materials Project database.

Dopant	Bulk doping		Predicted GB phase with dopant	
	Chemistry	Dopant formation energy (eV)	Chemistry	Formation energy (eV)
Yttrium	$Na_{13}YZr_7Si_8P_4O_{48}$	1.24	YPO4	-3.5
Scandium	$Na_{13}ScZr_7Si_8P_4O_{48}$	1.08	$Na_3Sc_2(PO_4)_3$	-3.09

Chapter 6. Direct observation of space charge layers at grain boundaries of Y-doped $BaZrO_3$

Low ionic conductivity of Y-doped $BaZrO_3$ is due to the blocking behavior of grain boundaries in this material. The resistive behavior of grain boundaries is attributed to low symmetry at grain boundaries, higher BaO evaporation at grain boundaries compared with bulk and also space charge theory. Using mostly current-voltage measurement techniques and in different conditions (dry and wet atmospheres, oxidizing and reducing atmospheres, different dopant concentrations, as sintered and annealed material); space charge theory is used to explain the distribution of dopants at grain boundaries and electrical properties of grain boundaries in this material. In this work, inline electron holography is used to characterize the grain boundary electrostatic potential and space charge layers at grain boundaries of Y-doped $BaZrO_3$. An average electrostatic potential of 0.8 V is obtained for BZY1 and BZY15 in dry condition which is slightly higher than values reported for Y-doped $BaZrO_3$ in dry condition. Combining phase images obtained at slightly different tilt angles could help to remove the artifacts from dynamic electron diffraction and improve the accuracy of potentials obtained by this method.

6.1. Introduction

Implementation of Y-doped $BaZrO_3$ in electrochemical devices such as hydrogen fuel cells is prevented mainly due to the poor ionic conductivity although it has a higher chemical stability and a higher bulk conductivity compared with other solid state electrolytes. Using mostly indirect experimental techniques which are usually based on impedance or current-voltage measurements, poor conductivity is mainly attributed to the high grain boundary resistivity. The blocking character of grain boundaries in Y-doped $BaZrO_3$ is attributed to BaO evaporation (stronger BaO loss at GB compared with bulk)[124,125], lower degree of symmetry in GB (symmetry decrease in acceptor doped $BaZrO_3$ lowers the bulk conductivity)[126] and space charge theory[127–131] . However, the correlation between the electrical properties of grain boundaries and their chemical composition in Y-doped $BaZrO_3$ in different cases (dry and wet atmospheres[132], oxidizing and reducing atmosphere[127], sintered and annealed BZY[128], strongly reduced BZY[129], different dopant concentration[130]) is consistent with the interpretation in terms of the space charge model. According to space charge model, accumulation of positively charged defects such as oxygen vacancies at grain boundary core results in a positively charged grain boundary core which according to space charge theory would form a negatively charged layers depleted from positively charged defects (i.e. oxygen vacancies, protons) on both sides of grain boundaries reducing the grain boundary conductivity[133]. Depending on distribution of Y dopants at grain boundaries, either Gouy-Chapman or Mott-Schottky is used to model the electrical

properties of grain boundaries[128]. The positive core charge at grain boundaries originates largely from high concentration of oxygen vacancies at grain boundary core caused by otherwise too short O-O bond distances in core structure [133,134] although segregation of protons is also important for the formation of space charges in grain boundaries of hydrated $BaZrO_3$ [131]. However, in pretty much all of these studies the effective grain boundary thickness ($\delta = 2\lambda$ or $2\lambda^*$; where λ and λ^* are the thickness of space charge layer in Gouy-Chapman or Mott-Schottky models) was estimated assuming Brick Layer Model (BLM) (using the relation, $\frac{C_{gb}}{C_b} = \frac{d}{\delta}$ in which C_{gb} and C_b are capacitance values of grain boundaries and bulk respectively and d and δ are grain size and depletion width in space charge model or grain boundary effective thickness). Furthermore, electrostatic potential at grain boundary core is then estimated using Mott-Schottky or Gouy-Chapman models depending on defect distributions at grain boundaries. However, Fleig and Maier[135] have shown that deviations from BLM due to “detour-effect” (current-detours around blocking grain boundaries occur if this lowers the impedance) and also “enhanced-area-effect” (referring to the fact that the current attempts to make use of a large effective grain boundary area) could influence the overall impedance of low conducting grain boundaries which technologically are of more importance to study.

In this study, Inline electron holography is used to determine the electrostatic potential at single grain boundaries of Y-doped $BaZrO_3$. In most of

TEM techniques, only amplitude of electron wave is being recorded however the whole image (both amplitude and phase of electron wave function) is recorded in electron holography. Variation in electrostatic and magnetic fields affects the phase of the electron wave function. However, it is physically impossible to directly measure the phase of electron wave function and it has to be measured indirectly[136]. A total of twenty possible modes of electron holography involving conventional TEM and STEM is distinguished which several of them have been demonstrated experimentally[137]. Details of different techniques used for imaging electric and magnetic fields based on TEM and STEM can be found elsewhere[138]. As of today, most often techniques used in conventional TEM are Fresnel imaging in combination with a transport-of-intensity equation (TIE) reconstruction and electron holography and Differential Phase Contrast (DPC) in STEM[138]. Differential Phase Contrast (DPC) in STEM has recently been used to visualize and quantify the projected, built-in electric field in the p-n junction[139]. This technique is also shown to be capable of detecting the electric field variations due to dopant concentration steps within both p-type and n-type regions[139]. DPC images are formed by taking the difference between the signals recorded on detector segments diametrically opposed about the optical axis, and thereby map variations in beam deflection and/or asymmetric intensity redistribution in the diffraction plane as the probe is scanned across the specimen[138,139]. While DPC images are obtained in STEM and in-focused mode it requires a suitable segmented-type detectors. Moreover, DPC STEM images can be monitored as live-images during the

experiment without any post-acquisition processing. The best contrast in DPC images are obtained from detector segments perpendicular to p-n junction (or interface of interest) therefore it is critical to orient the interface to have two detector segments perpendicular to interface plane. In this technique, care has to be taken at very high resolution (when the angular separation of Bragg beams is smaller than the beam's convergence angle. In this case, diffracted beams and zero order beam overlap and interfere causes inhomogeneities within the diffraction disk[138]. However, electron holography techniques offer a high field sensitivity and at the same time excellent spatial resolution. This technique depends on the interference of two (or more) coherent electron waves that combine to produce interferogram or hologram. This interference pattern must then be processed to retrieve or reconstruct the complex electron wave function[138]. Off-axis electron holography which has been used almost exclusively in electron microscopy studies, performed at the edge of thin area of the sample, uses a charged wire with positive potential (electrostatic biprism) to bend the two partial electron waves (external reference wave and the object wave) traveling on either side of wire towards one another and form an interference pattern. In inline holography, a series of images at different defocus distances (Δf_i) from the focal plane will be used and the object wave is its own reference wave; therefore can be performed anywhere within the sample. Inline holography experiments use the electron microscope in its standard configuration, but for quantitative work require the microscope to be equipped

with an energy filter which allows the holograms to be recorded with an energy selecting slit no wider than about 10 eV [140,141].

In inline holography, a number of images (N>3) with small and large defocus are required for an optimum transfer of phase information. Higher spatial frequency information are transferred in images with small defocus while images with high defocus contain information on large distance interference and are therefore required to retrieve low spatial frequencies. A small defocus step between images of through-focal series facilitates the image alignment. An electric field parallel or antiparallel to the electron trajectory causes a constant phase shift of the wave compared to the wave's part which does not transmit the region containing the field. This is the origin of Fresnel's fringes which can be observed at the grain boundaries. The interference of complex wave functions is employed in order to reconstruct the phase image[142,143]. The iterative reconstruction process starts with a guess of the object wave, simply using the amplitude of the image with the smallest defocus and keeping its phase at zero, and involves the following iterations steps:

1- The current estimate of the object wave is propagated to each of the N focal planes with defocus Δf_n according to (assuming an aberration-corrected microscope or sufficiently small enough objective aperture is used);

$$\Psi_{\Delta f}(\vec{r}) = FT^{-1}\left[\Psi_0(\vec{q})\exp\left(-i\chi(q,\Delta f)\right)\right], \qquad (1)$$

where $\chi(q,\Delta f)$ is coherent transfer function considering the objective lens aberrations (defocus and spherical aberration).

2- By comparing the simulated intensity with the experimental one in each plane with defocus Δf_n, a new estimate of image wave is obtained. For simulated and experimental image wave

$$I_{\Delta f}^{Sim}(\vec{r}) = \left|\Psi_{\Delta f}(\vec{r})\right|^2 \otimes E_S(\vec{r}, \Delta f), \quad (2)$$

$$d\Psi_{\Delta f}(\vec{r}) = \sqrt{I_{\Delta f}^{Exp}(\vec{r})} - \sqrt{I_{\Delta f}^{Sim}(\vec{r})}\,, \quad (3)$$

$$\Psi'_{\Delta f}(\vec{r}) = \frac{[|\Psi_{\Delta f}(\vec{r})| + d\Psi_{\Delta f}(\vec{r})]\Psi_{\Delta f}(\vec{r})}{|\Psi_{\Delta f}(\vec{r})|}\,, \quad (4)$$

where $E_S(\vec{r}, \Delta f)$ is the spatial coherence envelope function considering the effect of spatial and temporal incoherency of the beam on image intensity.

3- A new estimate of the object wave is obtained by back propagation of the image waves $\Psi'_{\Delta f}(\vec{r})$ by inverting Eq. (1) and a subsequent weighted averaging of the corresponding object waves.

The above steps are executed within a loop until a preassigned convergence criterion is reached[142,143].

6.2. Experimental Procedure

Y-doped $BaZrO_3$ (1 at. % and 15 at. % Y) powders were synthesized by solid-state reaction method using $BaCO_3$ (Acros Organics, 99%), Y-stabilized ZrO_2 (Sigma Aldrich, 3mol % and 8mol %) were used as precursors. The precursors were mixed using planetary ball mill in isopropanol media. The powders were then dried in drying oven at 85 °C and calcined at 1100 °C for 1.5 h. The calcined powders were then ground in planetary ball mill for 2 hrs and additional two cycles of calcination at 1300 °C for 2 hrs with grinding in between were used to prepare a single phase Y-doped $BaZrO_3$ nanopowders. Spark

Plasma Sintering (SPS)/ Field Assisted Sintering Technique (FAST) was used to prepare dense pellets at 1600 °C for 5 min at 60 MPa with heating rate of 100 °C/min.

The TEM foils for electron holography was prepared by standard FIB lift-out and thinning procedure using FEI Scios Dual Beam FIB/SEM. Inline electron hologram of grain boundaries were collected using an FEI Titan 80-300 KeV TEM with a small objective aperture to avoid grain reflections. A 21-member focal series was acquired using a 1000 nm defocus step with defocus ranging from -10000 nm to 10000 nm. All images were recorded on a 2048×2048 pixel charge-coupled device (CCD) camera (Gatan, Inc.). Reconstruction of in-line electron holograms was performed using full resolution wave reconstruction (FRWR) software[142,143], which takes into account the modulation transfer function (MTF) of the CCD camera, partial spatial coherence and defocus-induced image distortions. In our reconstructions, at least 200 reconstruction loops is used to obtain the final phase image.

The reconstructed phase images were then used to calculate the mean inner potential (MIP) according to the following expression;

$$\Delta\phi(r) = \phi(r) - \phi(r_0) = C(E)\int_{-\infty}^{\infty}[V(r) - V(r_0)]dz, \qquad (5)$$

wherein, $C(E)$, is an electron-energy-dependent interaction constant given by

$$C(E) = \left(\frac{2\pi}{\lambda}\right)\left(\frac{m_0c^2+E}{E(2m_0c^2+E)}\right) \qquad (6)$$

where λ, E and E_0 are the electron wavelength, kinetic energy and rest mass energy, respectively. The value of $C(E)$ is 6.53×10^6 rad V^{-1} m^{-1} at an accelerating voltage of 300 kV. The local specimen thickness (t) was determined from projected GB thickness (t_{proj}) and the angle of tilt (18°)

$$t = \frac{t_{proj}}{\sin(\theta)} \quad (7)$$

Average electrostatic potential was then fitted to space charge model (Mott-Schottky in this case) and it is used to determine the grain boundary electrostatic potential.

6.3. Results and Discussion

Figure 6.1 shows the typical bright-field TEM images of a grain boundary within BZY1 ($BaY_{0.01}Zr_{0.99}O_{12-x}$) specimen which were acquired at different defocus values ($\Delta f\sim$ -10000 nm, $\Delta f\sim$ -5000 nm, $\Delta f\sim$ 0 nm, $\Delta f\sim$ 5000 nm and $\Delta f\sim$ 10000 nm). The five acquired images are part of the through focal series used for reconstruction of phase image. Symmetric Fresnel fringes formed on either side of grain boundary due to change in local average electrostatic potential indicates that the selected grain boundary is in edge-on condition or close to edge-on condition.

Figure 6.2(a) and (b) represents the reconstructed phase image and phase profile of the same grain boundary represented in Figure 6.1. Note that image is rotated for illustration purposes only. The sharp drop at grain boundary core could be attributed to change in chemistry (segregation of impurities at

grain boundary core), reduction of density (excess volume associated with grain boundaries), etc. The relative phase difference in two adjacent grains on either side of the grain boundary (Figure 6.2) could also be attributed to the dynamical diffraction conditions due to the differences in crystal orientations of each grain. Combining focal series for a range of slightly different incident beam directions (or sample tilts) is reported to overcome the dynamical diffraction artifacts[144]. The thickness of TEM specimen was estimated by comparing the thickness of GB projection in tilted images. Figure 6.3 shows the selected grain boundary and neighboring grains at 0 degree tilt (Fig. 6.3(a)) and 18 degree tilt (Fig. 6.3(b)). Comparing the grain boundary thickness projection in two different images and using equation (7); the foil thickness is determined to be 34 nm.

Mean Inner Potential (MIP) maps were then obtained by dividing the phase image with foil thickness and interaction constant. As expected potential map looks identical to phase image (Figure 6.4) since it is linearly related to phase image (equation 5). Although the grain boundary core potential is affected by change in chemical composition and density of grain boundary core it is possible to use the two hills on either side of grain boundary in potential map to characterize the space charge layers adjacent to grain boundary core. According to space charge theory and in case of as-sintered Y-doped $BaZrO_3$, a Mott-Schottky model can be used to predict the electrical properties of grain boundaries[128]. In Mott–Schottky cases with moderate and high potentials the agreement between analytical and numerical solutions of Poisson equation is found to be satisfactory[145]. Equation (8) is reported to accurately reproduce the

potential of numerical approach both at distances close to interface and large distances from interface.

$$V = -\frac{\rho_0}{2\varepsilon_r\varepsilon_0}x^2 - E_0x + V_0 \ , \qquad (8)$$

According to this equation and at $= 0$; $V = V_0$, $\frac{d^2V}{dx^2} = -\frac{\rho_0}{\varepsilon_r\varepsilon_0}$ and $\frac{dV}{dx} = -E_0$ where V_0, ρ_0 and E_0 are the potential, charge and electric field at the edge of grain boundary (not grain boundary core)[145]. Therefore, this equation is used to fit the electrostatic potential hills on one side of each investigated grain boundaries in this work. Note that only data points from the hills adjacent to grain boundaries are fitted to this equation and data points affected by sharp dip at grain boundary core and/or large distances from grain boundary core is not considered in these fittings (Figure 6.5). As shown in Figure 6.5, an electrostatic potential of 1.32 and 1.36 V are obtained for grain boundary core which is much higher than value reported in literature using impedance measurements[124,127,146–150]. This is to be expected since the reported value from impedance measurements is an average value over a large number of grain boundaries and it is estimated assuming Brick Layer Model (BLM).

Figures 6.6-6.11 represent the MIP maps on one side of few grain boundaries within BZY1 specimen along with their electrostatic potential fittings using equation (8). An average of 0.88 ± 0.4 V is obtained for grain boundary electrostatic potential in BZY1 in dry condition (without water incorporation).

Figures 6.12-6.16 show the MIP maps of grain boundaries within BZY15 specimen along with their electrostatic potential fittings using equation (8). An average of 0.84 ± 0.4 V is obtained for grain boundary electrostatic potential in BZY15 in dry condition.

Grain boundary electrostatic potential in Y-doped $BaZrO_3$ is shown to be either temperature independent[127] or changes slightly by increasing temperature[148]. Therefore, it seems reasonable to compare the electrostatic potential obtained at room temperature in this work with grain boundary electrostatic potential obtained in previous reports using impedance measurements mostly at intermediate and high temperatures. Slightly different values are reported for grain boundary electrostatic potentials in Y-doped $BaZrO_3$ in literature. Iguchi et al. reported a barrier height of 0.29 to 0.57 V for Y-doped $BaZrO_3$ with Y concentration of (5, 10, 15 and 20 mole pct.). The barrier height is reported to decrease slightly by increasing dopant concentration in wet Ar atmosphere. While Chen at al. reported a barrier heights of 0.4, 0.5 and 0.8 V for BZY with Y concentration of 5, 8 and 20 mole pct respectively in wet N_2 atmosphere. Comparing with different reports, it is shown than grain boundary barrier height is changing between 0.9 to 0.4 V depending on mole concentration of yttrium (Figure 6.17). The values obtained in this work are well within the range reported in literature although grain boundary electrostatic potential does not change by molar concentration of yttrium which could be attributed to dynamic electron diffraction. Combining phase images for a range of slightly different incident beam (sample tilt) may help to overcome dynamic electron diffraction. Using

DFT calculations, a grain boundary potential of 0.4-0.45 V and 0.6 V are obtained for different symmetric tilt grain boundaries in $BaZrO_3$ without any dopants and in dry condition[131,133]. It has also shown that some grain boundaries have a lower grain boundary potential in dry atmosphere in compare with wet atmosphere while other grain boundaries have almost the same potential in both dry and wet atmosphere. This has been attributed to tendency of proton segregation in different grain boundaries. Nevertheless, the segregation of protons to grain boundaries is claimed to be an important part of space charge layers at grain boundaries of Y-doped $BaZrO_3$[131]. This discrepancy can also be observed in experimental results where a lower potential is reported for Y-doped $BaZrO_3$ (BZY10) in dry atmosphere (0.2 V) compared with wet atmosphere (0.5 V)[127] while in other cases grain boundary potential does not differ significantly between dry and wet conditions[129]. Comparing with values reported in literature, electrostatic potentials obtained in this work seems to be higher than previous works where grain boundary electrostatic potential is obtained using impedance spectroscopy and/or current-voltage measurement techniques. This can also be observed in space charge layer thickness as well. Grain boundary effective thickness ($\delta = 2\lambda$ or $2\lambda^*$; where λ and λ^* are the thickness of space charge layer in Gouy-Chapman or Mott-Schottky models) is reported to be about only few nanometers (< 10 nm). Therefore, the thickness of space charge layer is even less than 5 nm in previously reported studies while in our measurements electrostatic potential hills observed 10-20 nm away from grain boundary core which results in grain boundary thickness of 20-40 nm which is significant

comparing with particle size (< 100 nm) required for effective sintering of Y-doped $BaZrO_3$[151].

6.4. Conclusions

Space charge layers at grain boundaries of Y-doped $BaZrO_3$ is characterized for the first time using inline electron holography. While the average potential obtained from limited number of grain boundaries investigated for BZY1 (0.88 V) and BZY15 (0.84 V) is well within the range previously reported using impedance and/or current-voltage measurement techniques, it does not change by the concentration of yttrium dopants. This could either be attributed to dynamic electron diffraction which affects the Mean Inner Potential (MIP) maps obtained from holography or due to the limited number of grain boundaries investigated. Space charge layer is also observed to be thicker than the ones reported in previous reports which seems to be significant compared with particle sizes required for effective sintering of Y-doped $BaZrO_3$. Combining phase images of grain boundaries at different tilt angles may help to remove the artifacts from dynamic electron diffraction to obtain even more accurate grain boundary electrostatic potential.

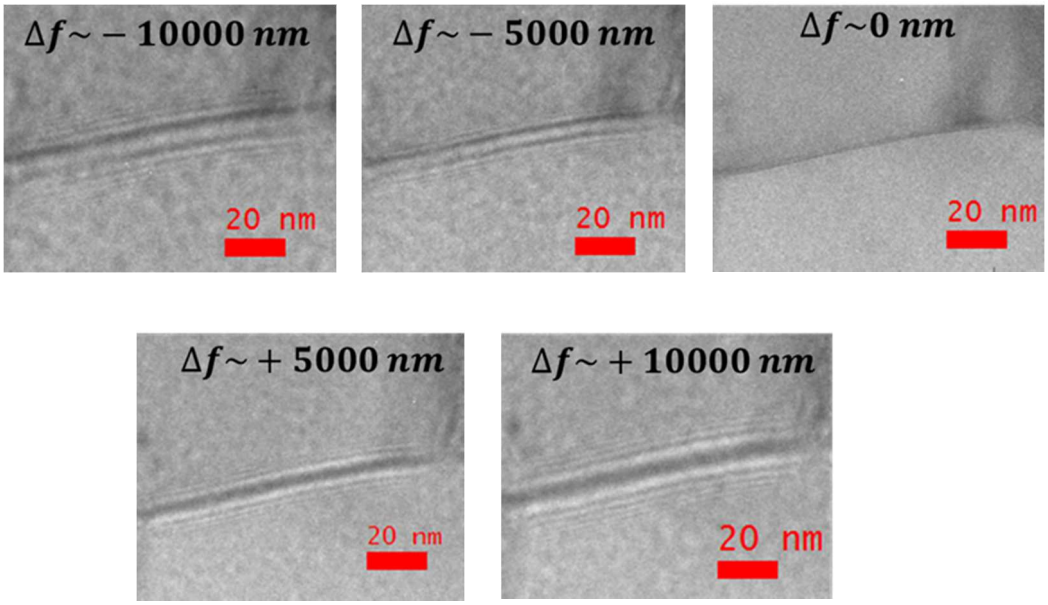

Figure 6.1 Five bright-field TEM images of a grain boundary within BZY1 specimen acquired at different defocus values. These five images are part of a 21-membered through focal series images obtained from -10000 nm to +10000 nm defocus values with 1000 nm defocus step.

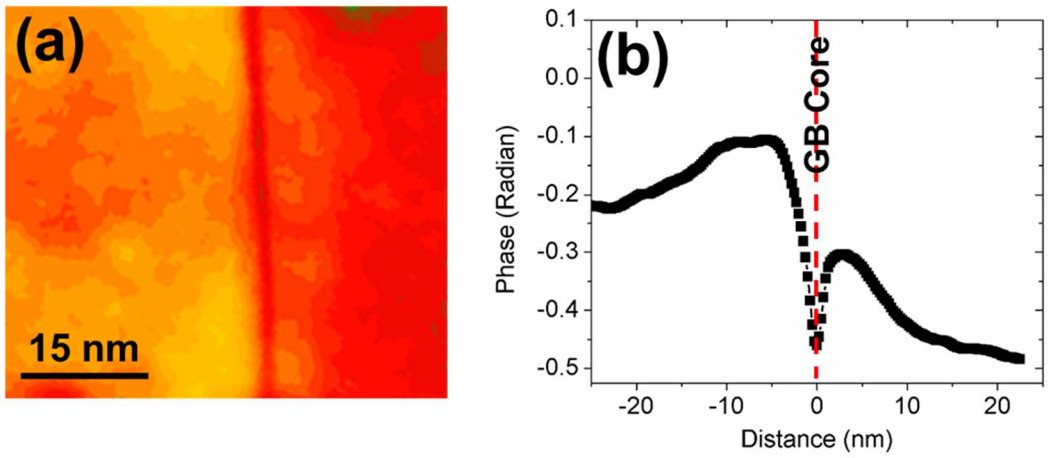

Figure 6.2 (a) Phase image and (b) phase profile of a grain boundary in BZY1 specimen reconstructed from focal series images represented in Figure 6.1.

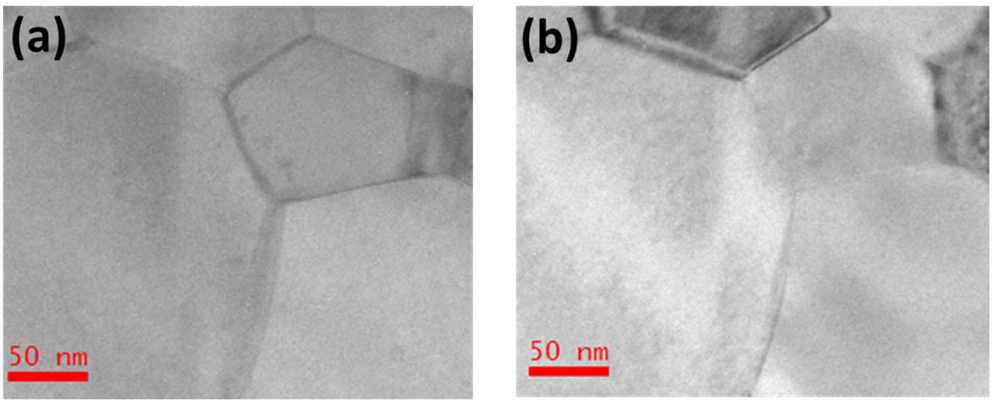

Figure 6.3 Selected grain boundary for phase reconstruction and neighboring grains at (a) 0 degree tilt and (b) 18 degree tilt. The thickness of grain boundary projection is used to estimate the TEM foil thickness using equation (7).

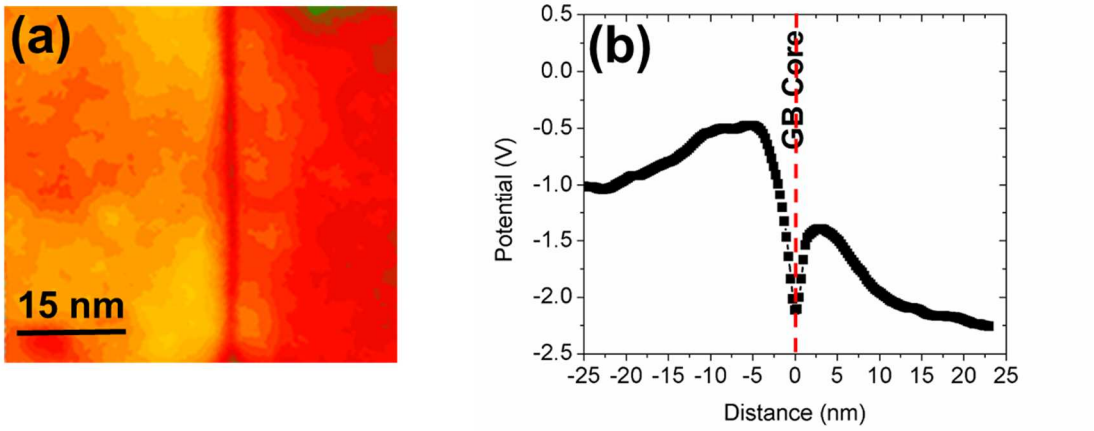

Figure 6.4 (a) Mean Inner Potential (MIP) map and (b) MIP profile of a grain boundary in BZY1 specimen calculated from phase map and profiles presented in Figure 6.2.

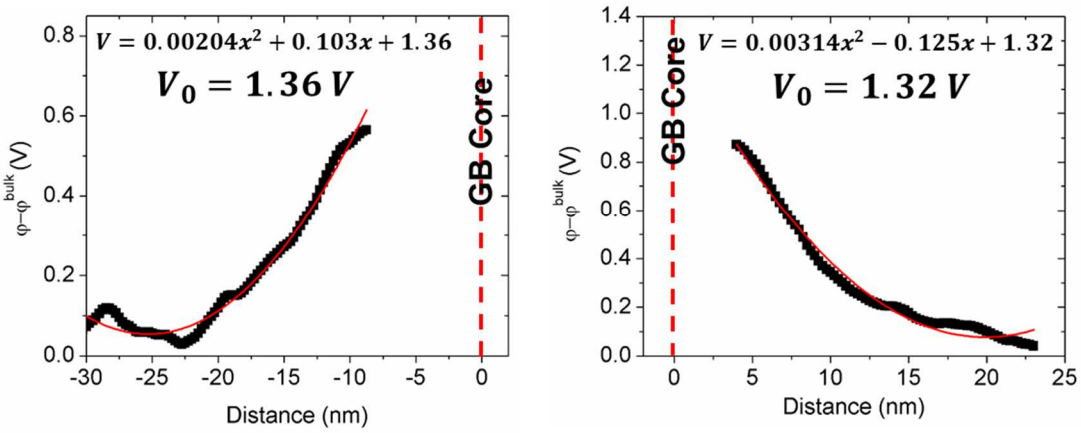

Figure 6.5 Space charge layer potential profiles fitting assuming Mott-Schottky case using equation (8) to determine the electrostatic potential at edge of grain boundary on either side of grain boundary.

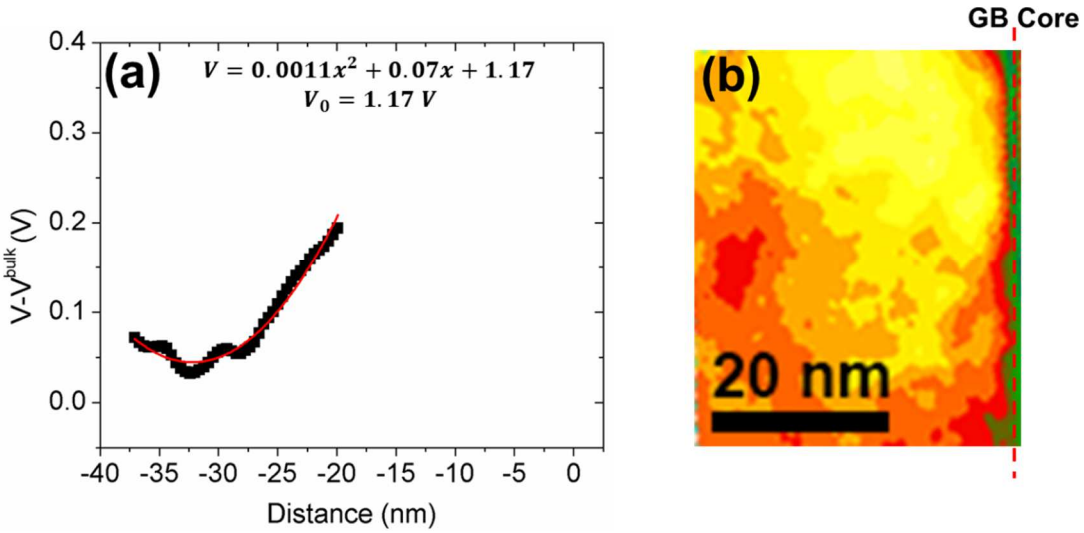

Figure 6.6 (a) Space charge layer potential profile fitting and (b) Mean Inner Potential (MIP) map of a grain boundary in BZY1 specimen. A grain boundary potential of 1.17 V is obtained for this grain boundary.

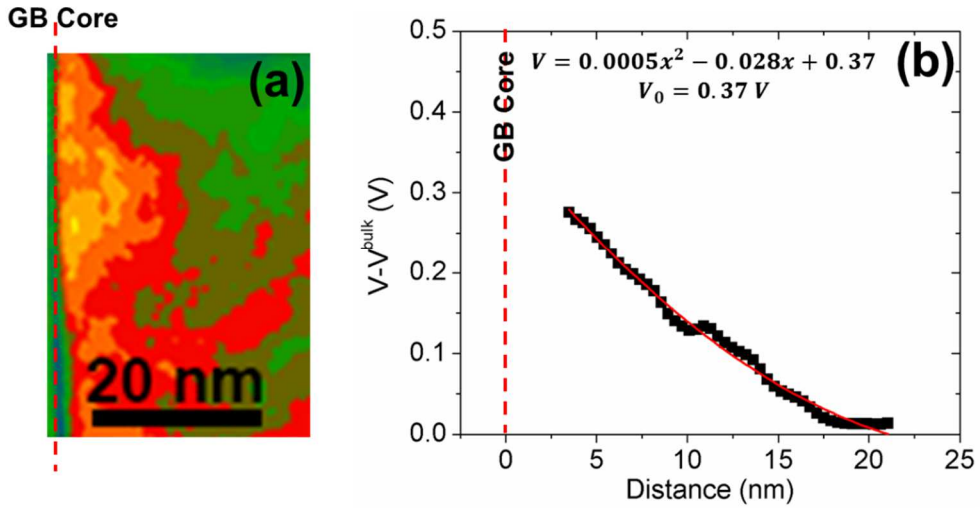

Figure 6.7 (a) Mean Inner Potential (MIP) map of a grain boundary in BZY1 specimen and (b) space charge layer potential profile fitting. A grain boundary potential of 0.37 V is obtained for this grain boundary.

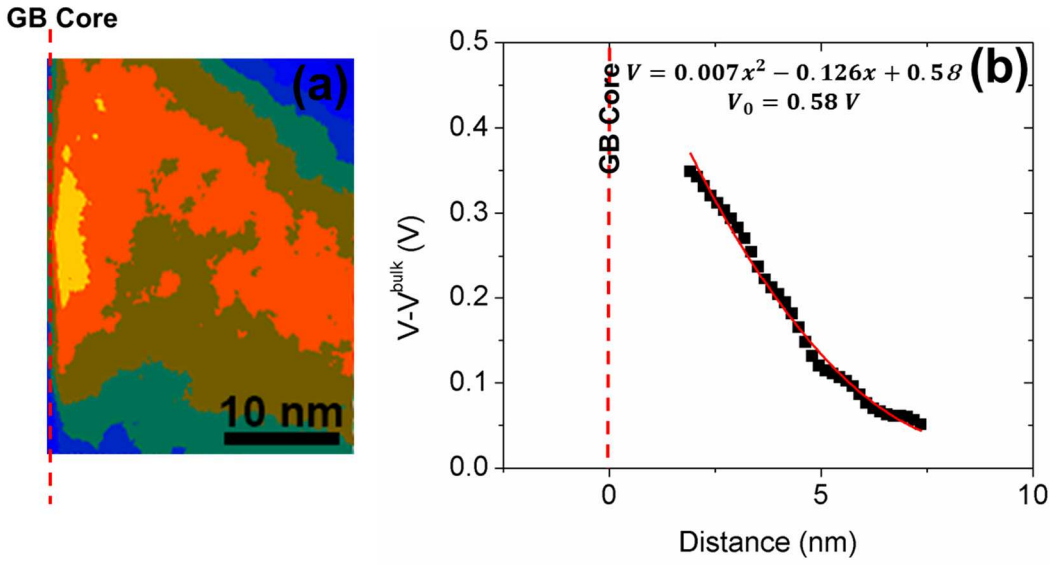

Figure 6.8 (a) Mean Inner Potential (MIP) map of a grain boundary in BZY1 specimen and (b) its space charge layer potential profile fitting. A grain boundary potential of 0.58 V is obtained for this grain boundary.

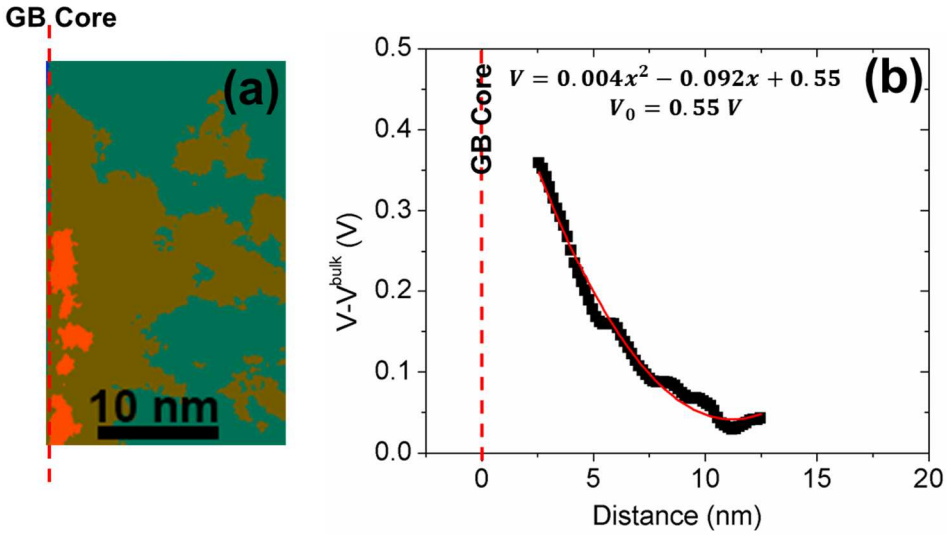

Figure 6.9 (a) Mean Inner Potential (MIP) map of a grain boundary in BZY1 specimen and (b) its space charge layer potential profile fitting. A grain boundary potential of 0.55 V is obtained for this grain boundary.

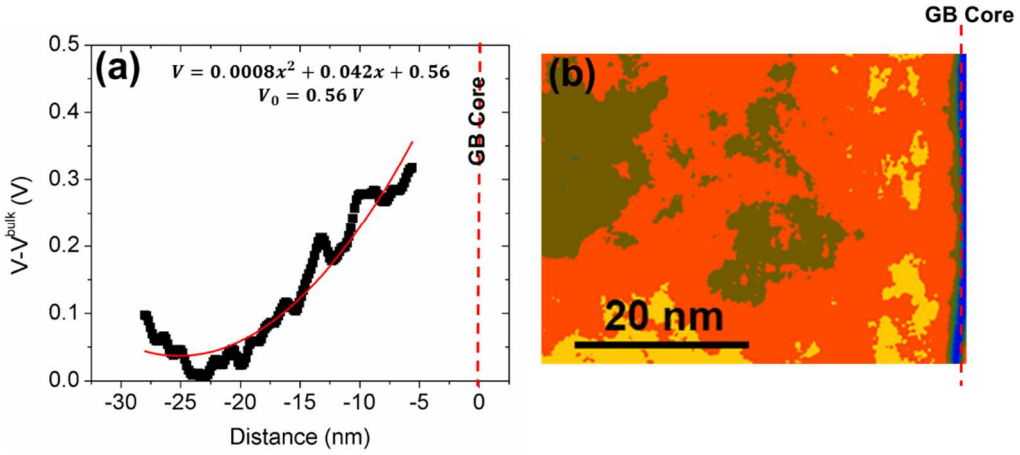

Figure 6.10 (a) Space charge layer potential profile fitting and (b) Mean Inner Potential (MIP) map of a grain boundary in BZY1 specimen. A grain boundary potential of 0.56 V is obtained for this grain boundary.

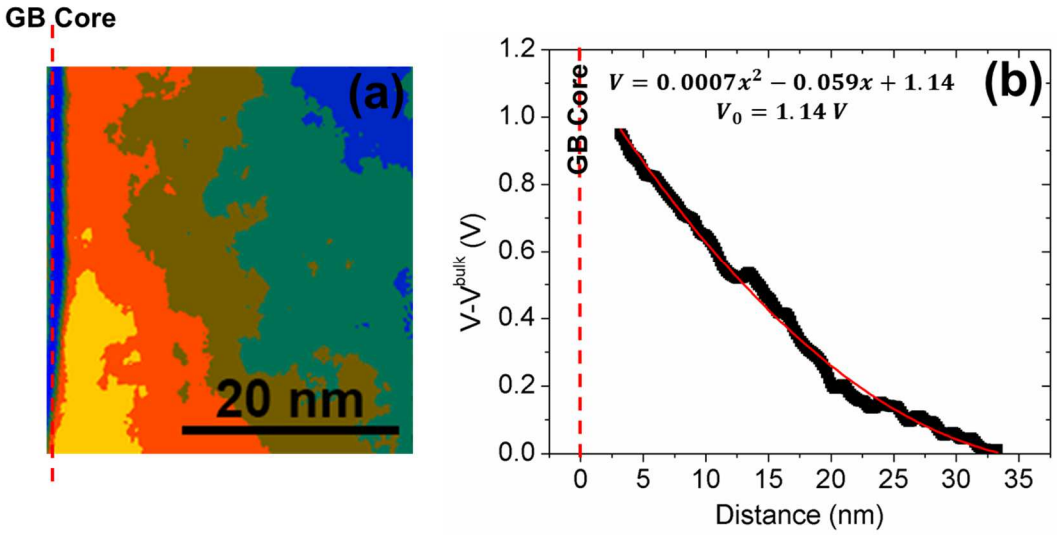

Figure 6.11 (a) Mean Inner Potential (MIP) map of a grain boundary in BZY1 specimen and (b) its space charge layer potential profile fitting. A grain boundary potential of 1.14 V is obtained for this grain boundary.

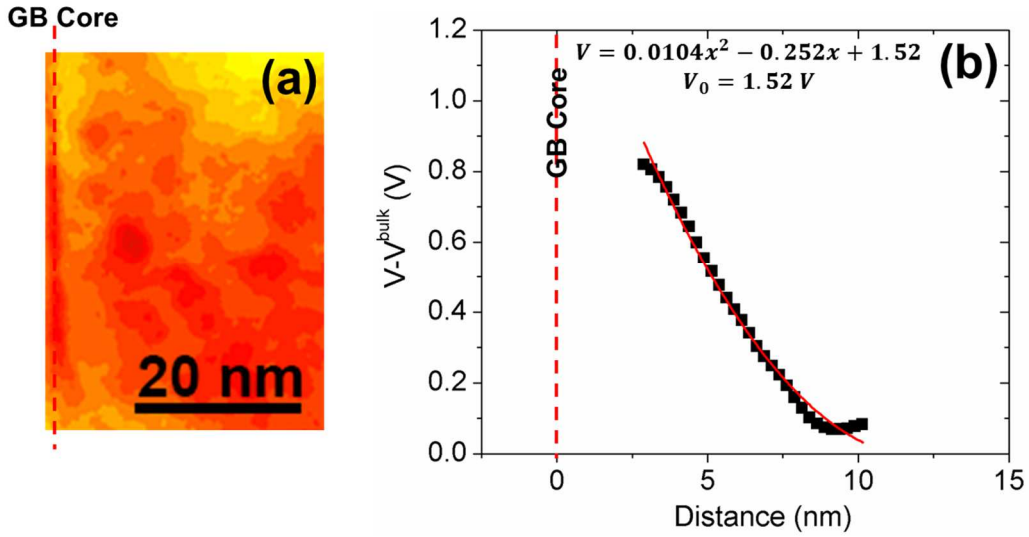

Figure 6.12 (a) Mean Inner Potential (MIP) map of a grain boundary in BZY15 specimen and (b) its space charge layer potential profile fitting. A grain boundary potential of 1.52 V is obtained for this grain boundary.

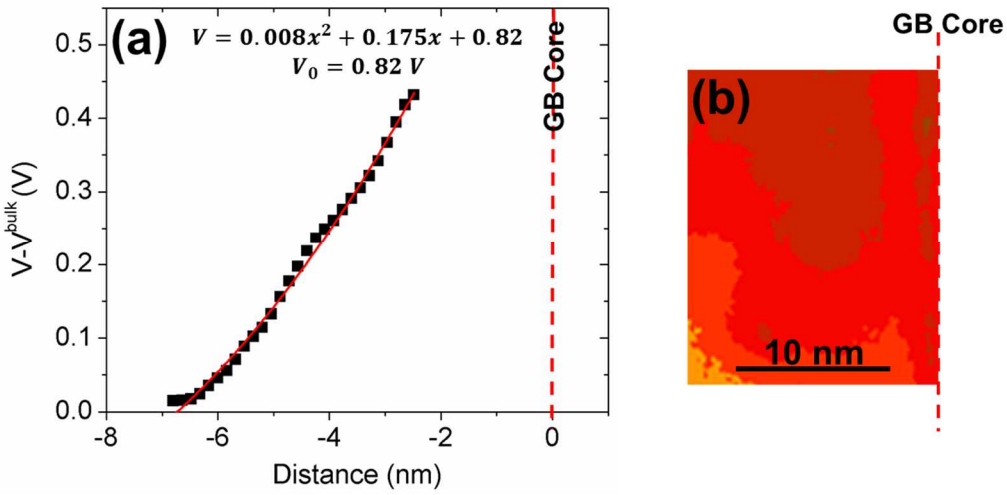

Figure 6.13 (a) Space charge layer potential profile fitting and (b) Mean Inner Potential (MIP) map of a grain boundary in BZY15 specimen. A grain boundary potential of 0.82 V is obtained for this grain boundary.

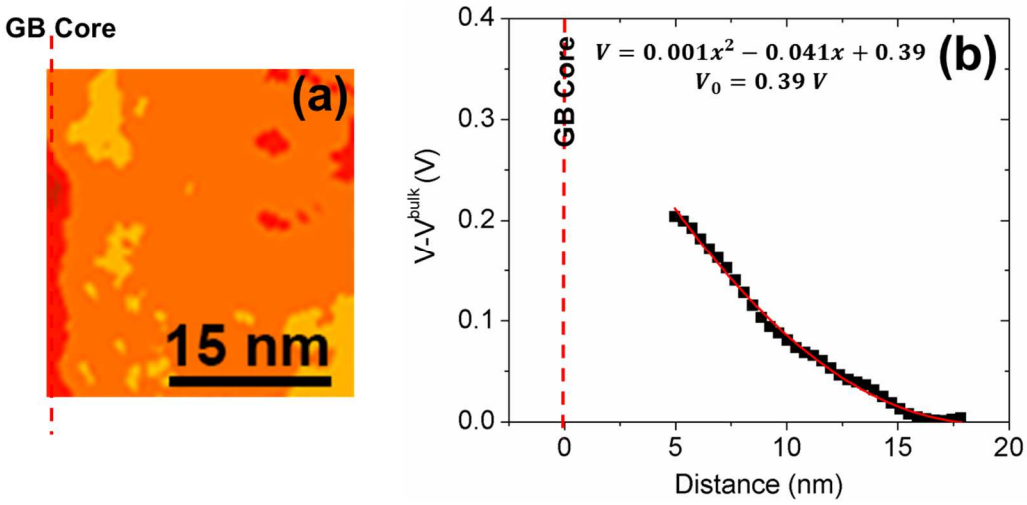

Figure 6.14 (a) Mean Inner Potential (MIP) map of a grain boundary in BZY15 specimen and (b) its space charge layer potential profile fitting. A grain boundary potential of 0.39 V is obtained for this grain boundary.

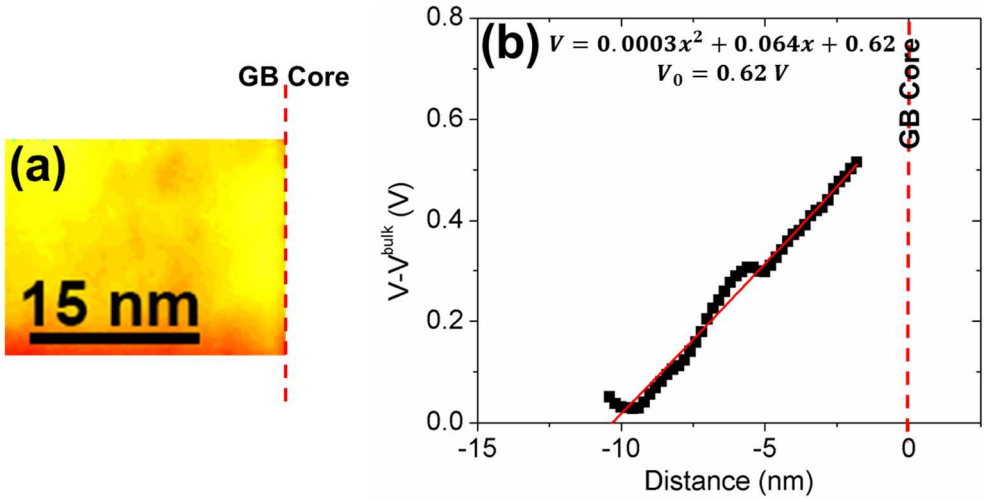

Figure 6.15 (a) Mean Inner Potential (MIP) map of a grain boundary in BZY15 specimen and (b) its space charge layer potential profile fitting. A grain boundary potential of 0.62 V is obtained for this grain boundary.

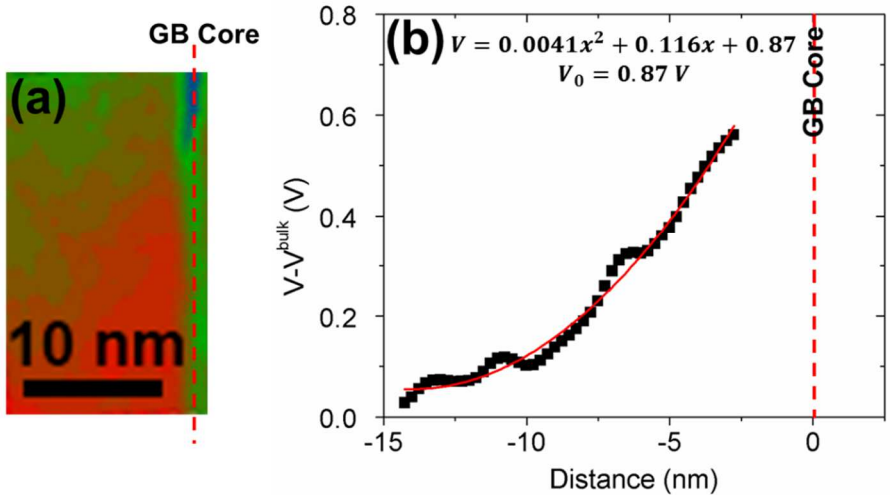

Figure 6.16 (a) Mean Inner Potential (MIP) map of a grain boundary in BZY15 specimen and (b) its space charge layer potential profile fitting. A grain boundary potential of 0.87 V is obtained for this grain boundary.

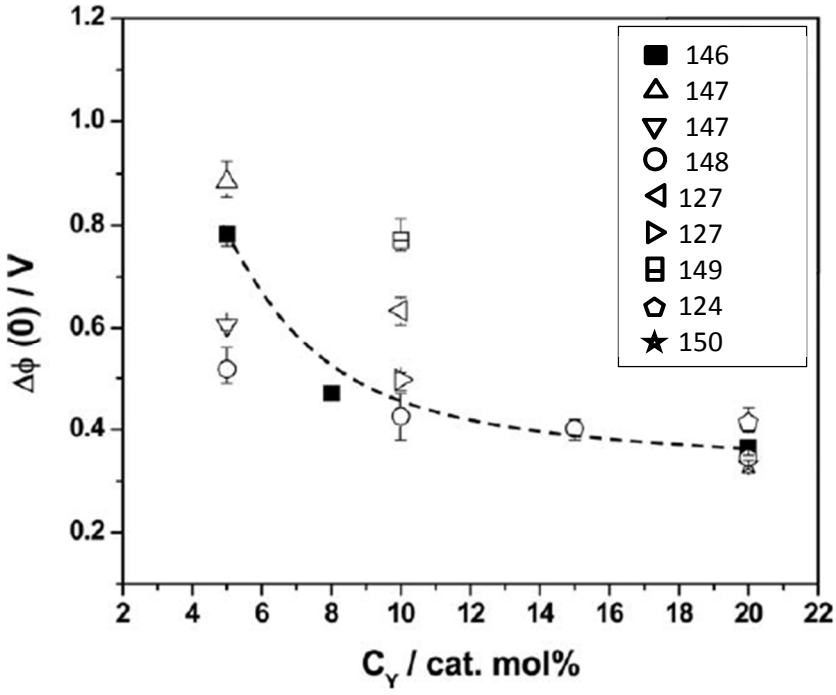

Figure 6.17 Grain boundary electrostatic potential for BZY samples reported in literature. The dotted line is a visual guide[146].

Chapter 7. Summary and Future Work

In this work, the importance of interfacial engineering of inorganic materials on their applications for energy conversion and storage is investigated.

In the first part, a systematic study is performed in which TiO_2 nanoparticles were annealed in various controlled atmospheres with the estimated oxygen partial pressure being varied from ~10^{-1} to ~ 10^{-25} atm and presence of other species (Ar, H_2, N_2, vacuum or hydrocarbon); subsequently, photocatalytic activities were tested. The results suggest that the oxygen partial pressure during annealing is not the dominant controlling factor. Furthermore, the use of vacuum environments or the presence of hydrocarbon species during annealing is effective in enhancing the photocatalytic activity, but the presence of H_2 at a partial pressure of 0.05 atm does not show an appreciable beneficial effect. HRTEM suggested that the enhanced photocatalytic activity of vacuum-activated TiO_2 may be related to subnanometer-thick disordered surface layers.

In the second part, the effect of surface nitridation on rate capability of TiO_2 as anode material for Li ion batteries is studied. It is demonstrated that the rate capabities of TiO_2 anatase nanoparticles can be improved substantially by annealing in NH_3 at 450-500 °C. The enhanced high-rate capacities are attributed to moderate surface nitridation with less-disordered nitridated regions, which may enhance the surface electronic conductivity without forming discrete nanoscale amorphous TiN/TiO_xN_y layers to block the lithium transport. For

future work, it would be interesting to use techniques such as EELS to determine the thickness of nitridation layer at different nitridation temperature/times. This could possibly help to further optimize the nitridation treatment to further improve the discharge capacity of TiO_2 at high rates.

In the third part, pseudocapacitive properties of V_2O_5-based adsorbates supported on TiO_2 nanoparticles have been systematically measured. Surface amorphous films (SAFs), which form naturally at thermodynamic equilibria at 550-600 °C with self-regulating or “equilibrium” thicknesses on the order of 1 nm, exhibit superior electrochemical performance at moderate and high scan rates (20-500 mV/s) that are of prime importance for supercapacitor applications, as compared with submonolayer and monolayer adsorbates formed at lower equilibration temperatures. For future work, it is possible to use different dopants which affect the thickness and physical properties of these monolayer catalysts. In addition to V_2O5/TiO_2 monolayer catalysts, there are also other types of monolayer catalysts which could be used for pseudocapacitor applications.

In the fourth part, a combined experimental and computational investigation into the effects of aliovalent doping in NASICON on both bulk and grain boundary ionic conductivity. Our results show that the dopants with low solid solubility limits in NASICON solid solution lead to the formation of a conducting secondary phase at grain boundaries, thereby improving effective grain boundary conductivity that is otherwise hindered by the poorly-conducting

Na_3PO_4 and ZrO_2 secondary phases in undoped NASICON. This is accompanied by a change in the Si/P ratio in the primary NASICON bulk phase, thereby transforming monoclinic NASICON to rhombohedral NASICON. The conductivity improvement of aliovalent-doped NASICON in previous reports is mainly attributed to substitution of Zr with dopants having similar radius to Zr. For future work, it may also be possible to prepare two-dimensional heterostructures with interfaces parallel to electric field which could help to obtain conductivities even higher than the ones obtained in 3-D bulk specimens. Interfaces with higher concentration of charge carriers would provide higher conductivities when they are parallel to electric field. In case of NASICON, this could even make it easier to prepare solid state batteries with NASICON membranes since it would be easier to prepare thin film of fragile NASICON on a substrate rather than thin free membrane of NASICON.

Finally, this work suggested that there are significant opportunities to improve both bulk and grain boundary conductivity of solid electrolytes via controlling the microstructure (e.g., the size and distribution of the secondary phase precipitated at grain boundaries) as well as interfacial engineering. In addition, prior studies have been successfully taken advantages of two-dimensional heterostructures[1] or textured columnar grains[123] to achieve much improved conductivities along one direction, and similar levels of controlled (well-defined) hetero-phase structures or interfaces (possibly with nanostructures) may help to achieve even higher Na ionic conductivity for Mg/Ni

doped NASICON. The assembly of this and early studies collectively suggest the important opportunities to achieve superior ionic conductivities via control microstructure and interfaces, in addition to the phase and doping of the primary bulk phases.

In the fifth part, inline electron holography is used to study the space charge layers at grain boundaries of Y-doped $BaZrO_3$. Using impedance spectroscopy techniques, an electrostatic potential of 0.4-0.8 V is reported at grain boundaries of Y-doped $BaZrO_3$ depending on concentration of dopants, temperature and atmosphere. An average of 0.8 V electrostatic potential is obtained using inline electron holography technique for BZY1 and BZY15 at room temperature in dry condition which seems to be higher than the ones reported in literature. Space charge layer on each side of grain boundaries are also thicker than the ones estimated using BLM model. For future work, phase images obtained at slightly different tilt angle can be combined to remove the artifacts due to dynamic electron diffraction in order to obtain more accurate values for grain boundary electrostatic potential. It is also possible to investigate single grain boundaries and compare electrostatic potential of grain boundaries with different type of grain boundary structure, segregation/absorption. Segregation of impurities with effective negative charge to grain boundary core could help to reduce the positive charge at grain boundary core therefore improving the grain boundary conductivity of Y-doped $BaZrO_3$.

References:

1 J. Maier, *Nat Mater*, 2005, **4**, 805–815.

2 K. Lehovec, *J. Chem. Phys.*, 1953, **21**.

3 C. Wagner, *J. Phys. Chem. Solids*, 1972, **33**, 1051–1059.

4 T. Jow and J. B. Wagner, *J. Electrochem. Soc.* , 1979, **126**, 1963–1972.

5 J. Maier, *J. Electrochem. Soc.* , 1987, **134**, 1524–1535.

6 J. Maier, *J. Phys. Chem. Solids*, 1985, **46**, 309–320.

7 J. Maier, *Prog. Solid State Chem.*, 1995, **23**, 171–263.

8 J. Luo, *Crit. Rev. Solid State Mater. Sci.*, 2007, **32**, 67–109.

9 M. Tang, W. C. Carter and R. M. Cannon, *Phys. Rev. B*, 2006, **73**, 24102.

10 X. Chen, S. Shen, L. Guo and S. S. Mao, *Chem. Rev.*, 2010, **110**, 6503–6570.

11 A. Fujishima, X. Zhang and D. A. Tryk, *Surf. Sci. Rep.*, 2008, **63**, 515–582.

12 X. Chen, L. Liu, P. Y. Yu and S. S. Mao, *Science (80-.).*, 2011, **331**, 746 LP-750.

13 J. Luo and Y.-M. Chiang, *Annu. Rev. Mater. Res.*, 2008, **38**, 227–249.

14 S. Tominaka, Y. Tsujimoto, Y. Matsushita and K. Yamaura, *Angew. Chemie Int. Ed.*, 2011, **50**, 7418–7421.

15 G. Wang, H. Wang, Y. Ling, Y. Tang, X. Yang, R. C. Fitzmorris, C. Wang, J. Z. Zhang and Y. Li, *Nano Lett.*, 2011, **11**, 3026–3033.

16 S. Yang, W. Tang, Y. Ishikawa and Q. Feng, *Mater. Res. Bull.*, 2011, **46**, 531–537.

17 M. Xing, J. Zhang, F. Chen and B. Tian, *Chem. Commun.*, 2011, **47**, 4947–4949.

18 F. Zuo, L. Wang, T. Wu, Z. Zhang, D. Borchardt and P. Feng, *J. Am. Chem. Soc.*, 2010, **132**, 11856–11857.

19 S. U. M. Khan, M. Al-Shahry and W. B. Ingler, *Science (80-.)*., 2002, **297**, 2243 LP-2245.

20 R. Leary and A. Westwood, *Carbon N. Y.*, 2011, **49**, 741–772.

21 N. Li, K. L. Yao, L. Li, Z. Y. Sun, G. Y. Gao and L. Zhu, *J. Appl. Phys.*, 2011, **110**.

22 B. Kang and G. Ceder, *Nature*, 2009, **458**, 190–193.

23 K. Sun and S. J. Dillon, *Electrochem. commun.*, 2011, **13**, 200–202.

24 A. Kayyar, H. Qian and J. Luo, *Appl. Phys. Lett.*, 2009, **95**.

25 D. Liu, Y. Liu, A. Pan, K. P. Nagle, G. T. Seidler, Y.-H. Jeong and G. Cao, *J. Phys. Chem. C*, 2011, **115**, 4959–4965.

26 K.-S. Park, A. Benayad, D.-J. Kang and S.-G. Doo, *J. Am. Chem. Soc.*, 2008, **130**, 14930–14931.

27 K. S. Han, J. W. Lee, Y. M. Kang, J. Y. Lee and J. K. Kang, *Small*, 2008, **4**, 1682–1686.

28 H. Han, T. Song, J.-Y. Bae, L. F. Nazar, H. Kim and U. Paik, *Energy Environ. Sci.*, 2011, **4**, 4532–4536.

29 J.-Y. Shin, J. H. Joo, D. Samuelis and J. Maier, *Chem. Mater.*, 2012, **24**, 543–551.

30 J. Lee, Y. S. Jung, S. C. Warren, M. Kamperman, S. M. Oh, F. J. DiSalvo and U. Wiesner, *Macromol. Chem. Phys.*, 2011, **212**, 383–390.

31 S. K. Das, M. Patel and A. J. Bhattacharyya, *ACS Appl. Mater. Interfaces*, 2010, **2**, 2091–2099.

32 P. Singh, M. Patel, A. Gupta, A. J. Bhattacharyya and M. S. Hegde, *J. Electrochem. Soc.* , 2012, **159**, A1189–A1197.

33 S. Yoon, B. H. Ka, C. Lee, M. Park and S. M. Oh, *Electrochem. Solid-*

State Lett. , 2009, **12**, A28–A32.

34 A. Kayyar, J. Huang, M. Samiee and J. Luo, 2012, e4104.

35 Y.-G. Guo, Y.-S. Hu, W. Sigle and J. Maier, *Adv. Mater.*, 2007, **19**, 2087–2091.

36 J. Zhang, X. Yan, J. Zhang, W. Cai, Z. Wu and Z. Zhang, *J. Power Sources*, 2012, **198**, 223–228.

37 Z. Zhang, X. Wang, J. Long, Q. Gu, Z. Ding and X. Fu, *J. Catal.*, 2010, **276**, 201–214.

38 J.-Y. Shin, D. Samuelis and J. Maier, *Solid State Ionics*, 2012, **225**, 590–593.

39 P. R. Cantwell, M. Tang, S. J. Dillon, J. Luo, G. S. Rohrer and M. P. Harmer, *Acta Mater.*, 2014, **62**, 1–48.

40 K.-X. Wang, X.-H. Li and J.-S. Chen, *Adv. Mater.*, 2015, **27**, 527–545.

41 M. Samiee and J. Luo, *J. Power Sources*, 2014, **245**, 594–598.

42 J. Huang and J. Luo, *Phys. Chem. Chem. Phys.*, 2014, **16**, 7786–7798.

43 W. Liu, W. Pan, J. Luo, A. Godfrey, G. Ou, H. Wu and W. Zhang, *Nat. Commun.*, 2015, **6**, 8354.

44 M. Samiee and J. Luo, *Mater. Lett.*, 2013, **98**, 205–208.

45 Q. Zhao, X. Wang, J. Liu, H. Wang, Y. Zhang, J. Gao, J. Liu and Q. Lu, *J. Electrochem. Soc.* , 2015, **162**, A845–A851.

46 S. L. Candelaria, B. B. Garcia, D. Liu and G. Cao, *J. Mater. Chem.*, 2012, **22**, 9884–9889.

47 I. E. Wachs, R. Y. Saleh, S. S. Chan and C. C. Chersich, *Appl. Catal.*, 1985, **15**, 339–352.

48 F. Cavani, E. Foresti, F. Trifiró and G. Busca, *J. Catal.*, 1987, **106**, 251–262.

49 M. Sanati and A. Andersson, *J. Mol. Catal.*, 1990, **59**, 233–255.

50 Y.-C. Xie and Y.-Q. Tang, ed. H. P. and P. B. W. B. T.-A. in C. D.D. Eley, Academic Press, 1990, vol. Volume 37, pp. 1–43.

51 I. E. Wachs and B. M. Weckhuysen, *Appl. Catal. A Gen.*, 1997, **157**, 67–

90.

52 I. E. Wachs, *Dalt. Trans.*, 2013, **42**, 11762–11769.

53 M. Epifani, T. Chavez-Capilla, T. Andreu, J. Arbiol, J. Palma, J. R. Morante and R. Diaz, *Energy Environ. Sci.*, 2012, **5**, 7555–7558.

54 H. Qian and J. Luo, *Appl. Phys. Lett.*, 2007, **91**.

55 H. Qian and J. Luo, *Acta Mater.*, 2008, **56**, 4702–4714.

56 J. Luo, M. Tang, R. M. Cannon, W. C. Carter and Y.-M. Chiang, *Mater. Sci. Eng. A*, 2006, **422**, 19–28.

57 D. R. CLARKE, *J. Am. Ceram. Soc.*, 1987, **70**, 15–22.

58 D. R. Clarke, T. M. Shaw, A. P. Philipse and R. G. Horn, *J. Am. Ceram. Soc.*, 1993, **76**, 1201–1204.

59 M. D. Stoller and R. S. Ruoff, *Energy Environ. Sci.*, 2010, **3**, 1294–1301.

60 V. Aravindan, Y. L. Cheah, W. F. Mak, G. Wee, B. V. R. Chowdari and S. Madhavi, *Chempluschem*, 2012, **77**, 570–575.

61 M. P. Yeager, W. Du, B. Bishop, M. Sullivan, W. Xu, D. Su, S. D. Senanayake, J. Hanson and X. Teng, *ChemSusChem*, 2013, **6**, 2231–2235.

62 I. E. Rauda, V. Augustyn, L. C. Saldarriaga-Lopez, X. Chen, L. T. Schelhas, G. W. Rubloff, B. Dunn and S. H. Tolbert, *Adv. Funct. Mater.*, 2014, **24**, 6717–6728.

63 I. Shakir, J. H. Choi, M. Shahid, S. A. Shahid, U. A. Rana, M. Sarfraz and D. J. Kang, *Electrochim. Acta*, 2013, **111**, 400–404.

64 M. Salari, S. H. Aboutalebi, K. Konstantinov and H. K. Liu, *Phys. Chem. Chem. Phys.*, 2011, **13**, 5038–5041.

65 J. Xu, Q. Gao, Y. Zhang, Y. Tan, W. Tian, L. Zhu and L. Jiang, *Sci. Rep.*, 2014, **4**, 5545.

66 S.-H. Park, S.-B. Yoon, H.-K. Kim, J. T. Han, H.-W. Park, J. Han, S.-M. Yun, H. G. Jeong, K. C. Roh and K.-B. Kim, *Sci. Rep.*, 2014, **4**, 6118.

67 T. Zhu, S. J. Zheng, Y. G. Chen, J. Luo, H. B. Guo and Y. E. Chen, *J. Mater. Sci.*, 2014, **49**, 6118–6126.

68 Y. Zhu, C. Cao, S. Tao, W. Chu, Z. Wu and Y. Li, *Sci. Rep.*, 2014, **4**, 5787.

69 Q. Yang, Z. Lu, X. Sun and J. Liu, *Sci. Rep.*, 2013, **3**, 3537.

70 M. Salari, S. H. Aboutalebi, A. T. Chidembo, I. P. Nevirkovets, K. Konstantinov and H. K. Liu, *Phys. Chem. Chem. Phys.*, 2012, **14**, 4770–4779.

71 C. Zhao and I. E. Wachs, *J. Catal.*, 2008, **257**, 181–189.

72 K. Alexopoulos, P. Hejduk, M. Witko, M.-F. Reyniers and G. B. Marin, *J. Phys. Chem. C*, 2010, **114**, 3115–3130.

73 S. Saha, M. Jana, P. Khanra, P. Samanta, H. Koo, N. C. Murmu and T. Kuila, *ACS Appl. Mater. Interfaces*, 2015, **7**, 14211–14222.

74 C. Hu, H. Xu, X. Liu, F. Zou, L. Qie, Y. Huang and X. Hu, *Sci. Rep.*, 2015, **5**, 16012.

75 G. Wang, X. Lu, Y. Ling, T. Zhai, H. Wang, Y. Tong and Y. Li, *ACS Nano*, 2012, **6**, 10296–10302.

76 J. B. Goodenough, H. Y. P. Hong and J. A. Kafalas, *Mater. Res. Bull.*, 1976, **11**, 203–220.

77 H. Y. P. Hong, *Mater. Res. Bull.*, 1976, **11**, 173–182.

78 L. Vijayan and G. Govindaraj, *J. Phys. Chem. Solids*, 2011, **72**, 613–619.

79 A. G. Jolley, G. Cohn, G. T. Hitz and E. D. Wachsman, *Ionics (Kiel).*, 2015, **21**, 3031–3038.

80 Q. Ma, M. Guin, S. Naqash, C.-L. Tsai, F. Tietz and O. Guillon, *Chem. Mater.*, **0**, null.

81 T. Salkus, A. Dindune, Z. Kanepe, J. Ronis, A. Urcinskas, A. Kezionis and A. F. Orliukas, *Solid State Ionics*, 2007, **178**, 1282–1287.

82 M. Jansen and U. Henseler, *J. Solid State Chem.*, 1992, **99**, 110–119.

83 A. Hayashi, K. Noi, N. Tanibata, M. Nagao and M. Tatsumisago, *J. Power Sources*, 2014, **258**, 420–423.

84 A. Hayashi, K. Noi, A. Sakuda and M. Tatsumisago, *Nat. Commun.*, 2012, **3**.

85 W. D. Richards, T. Tsujimura, L. J. Miara, Y. Wang, J. C. Kim, S. P. Ong,

I. Uechi, N. Suzuki and G. Ceder, 2016, **7**.

86 W. D. Richards, T. Tsujimura, L. Miara, Y. Wang, J. C. Kim, S. P. Ong, I. Uechi, N. Suzuki and G. Ceder, *Nat. Commun.*, 2016, **7**, 1–8.

87 G. Sahu and C. Liang, in *Handbook of Solid State Batteries*, pp. 365–389.

88 F. Mauvy, E. Siebert and P. Fabry, *Talanta*, 1999, **48**, 293–303.

89 R. O. Fuentes, F. Figueiredo, F. M. B. Marques and J. I. Franco, *Solid State Ionics*, 2001, **139**, 309–314.

90 B. Radhakrishnan and S. P. Ong, *Front. Energy Res.*, 2016, **4**, 1–12.

91 W. Bogusz, F. Krok and W. Jakubowski, *Solid State Ionics*, 1981, **2**, 171–174.

92 O. Bohnke, S. Ronchetti and D. Mazza, *Solid State Ionics*, 1999, **122**, 127–136.

93 W. Bogusz, F. Krok and W. Jakubowski, *Solid State Ionics*, 1981, **2**, 171–174.

94 R. Fuentes, F. M. Figueiredo, F. M. B. Marques and J. I. Franco, *Solid State Ionics*, 2001, **140**, 173–179.

95 Z.-Z. ZHANG, S.-Q. SHI, Y.-S. HU and L.-Q. CHEN, *J. Inorg. Mater.*, 2013, **28**, 1255–1260.

96 A. G. Jolley, D. D. Taylor, N. J. Schreiber and E. D. Wachsman, *J. Am. Ceram. Soc.*, 2015, **98**, 2902–2907.

97 Google Patents, 2012.

98 G. Kresse and J. Furthmüller, *Phys. Rev. B. Condens. Matter*, 1996, **54**, 11169–11186.

99 S. P. Ong, W. D. Richards, A. Jain, G. Hautier, M. Kocher, S. Cholia, D. Gunter, V. L. Chevrier, K. a. Persson and G. Ceder, *Comput. Mater. Sci.*, 2013, **68**, 314–319.

100 G. Henkelman, B. P. Uberuaga and H. Jónsson, *J. Chem. Phys.*, 2000, **113**, 9901.

101 A. Jain, S. P. Ong, W. Chen, B. Medasani, X. Qu, M. Kocher, M. Brafman, G. Petretto, G.-M. Rignanese, G. Hautier, D. Gunter and K. a. Persson, *Concurr. Comput. Pract. Exp.*, 2015, **27**, 5037–5059.

102 Z. Deng, B. Radhakrishnan and S. P. Ong, *Chem. Mater.*, 2015, **27**, 3749–3755.

103 A. Ahmad, T. A. Wheat, A. K. Kuriakose, J. D. Canaday and A. G. McDonald, *Solid State Ionics*, 1987, **24**, 89–97.

104 O. Bohnke, S. Ronchetti and D. Mazza, *Solid State Ionics*, 1999, **122**, 127–136.

105 J. T. S. Irvine and A. R. West, *Solid State Ionics*, 1989, **37**, 73–78.

106 R. E. Clausing, F. Waelbroeck, J. Winter, P. Wienhold, L. Kiinen and N. Noda, *Surf. Sci. Rep.*, 1989, **10**, 105–188.

107 S. Song, H. M. Duong, A. M. Korsunsky, N. Hu and L. Lu, *Sci. Rep.*, 2016, **6**, 32330.

108 E. R. Losilla, M. a. G. Aranda, S. Bruque, M. a. París, J. Sanz and A. R. West, *Chem. Mater.*, 1998, **10**, 665–673.

109 B. Lang, B. Ziebarth and C. Elsässer, *Chem. Mater.*, 2015, **27**, 5040–5048.

110 J.-S. Lee, C.-M. Chang, Y. I. L. Lee, J.-H. Lee and S.-H. Hong, *J. Am. Ceram. Soc.*, 2004, **87**, 305–307.

111 L. Zhang, F. Liu, K. Brinkman, K. L. Reifsnider and A. V Virkar, *J. Power Sources*, 2014, **247**, 947–960.

112 J. T. S. Irvine and A. R. West, *Mater. Res. Bull.*, 1987, **22**, 1047–1054.

113 W.-G. Yin, J. Liu, C.-G. Duan, W. N. Mei, R. W. Smith and J. R. Hardy, *Phys. Rev. B*, 2004, **70**, 64302.

114 A. Hooper, P. McGeehin, K. T. Harrison and B. C. Tofield, *J. Solid State Chem.*, 1978, **24**, 265–275.

115 K. Shahi and J. B. Wagner, *J. Phys. Chem. Solids*, 1982, **43**, 713–722.

116 K. Shahi and J. B. Wagner, *Appl. Phys. Lett.*, 1980, **37**.

117 N. Sata, N. Y. Jin-Phillipp, K. Eberl and J. Maier, *Solid State Ionics*, 2002, **154**–**155**, 497–502.

118 N. Sata, K. Eberman, K. Eberl and J. Maier, *Nature*, 2000, **408**, 946–949.

119 N. I. Sorokin, I. I. Buchinskaya, P. P. Fedorov and B. P. Sobolev, *Inorg.*

Mater., 2008, **44**, 189–192.

120 G. Harley, R. Yu and L. C. De Jonghe, *Solid State Ionics*, 2007, **178**, 769–773.

121 M. Samiee and J. Luo, *ACS Appl. Mater. Interfaces*, 2016, **8**, 12871–12880.

122 J. Luo, *J. Mater.*, 2015, **1**, 22–32.

123 D. Pergolesi, E. Fabbri, A. D'Epifanio, E. Di Bartolomeo, A. Tebano, S. Sanna, S. Licoccia, G. Balestrino and E. Traversa, *Nat Mater*, 2010, **9**, 846–852.

124 P. Babilo, T. Uda and S. M. Haile, *J. Mater. Res.*, 2007, **22**, 1322–1330.

125 Y. Yamazaki, R. Hernandez-Sanchez and S. M. Haile, *J. Mater. Chem.*, 2010, **20**, 8158–8166.

126 K. D. Kreuer, *Annu. Rev. Mater. Res.*, 2003, **33**, 333–359.

127 C. Kjølseth, H. Fjeld, Ø. Prytz, P. I. Dahl, C. Estournès, R. Haugsrud and T. Norby, *Solid State Ionics*, 2010, **181**, 268–275.

128 M. Shirpour, B. Rahmati, W. Sigle, P. A. van Aken, R. Merkle and J. Maier, *J. Phys. Chem. C*, 2012, **116**, 2453–2461.

129 M. Shirpour, R. Merkle and J. Maier, *Solid State Ionics*, 2012, **216**, 1–5.

130 F. Iguchi, C.-T. Chen, H. Yugami and S. Kim, *J. Mater. Chem.*, 2011, **21**, 16517–16523.

131 E. E. Helgee, A. Lindman and G. Wahnström, *Fuel Cells*, 2013, **13**, 19–28.

132 M. Shirpour, R. Merkle, C. T. Lin and J. Maier, *Phys. Chem. Chem. Phys.*, 2012, **14**, 730–740.

133 B. Joakim Nyman, E. E. Helgee and G. Wahnström, *Appl. Phys. Lett.*, 2012, **100**.

134 A. Lindman, E. E. Helgee, B. J. Nyman and G. Wahnström, *Solid State Ionics*, 2013, **230**, 27–31.

135 J. Fleig and J. Maier, *J. Electrochem. Soc.* , 1998, **145**, 2081–2089.

136 S. von Alfthan, N. A. Benedek, L. Chen, A. Chua, D. Cockayne, K. J.

Dudeck, C. Elsässer, M. W. Finnis, C. T. Koch, B. Rahmati, M. Rühle, S.-J. Shih and A. P. Sutton, *Annu. Rev. Mater. Res.*, 2010, **40**, 557–599.

137 J. M. Cowley, *Ultramicroscopy*, 1992, **41**, 335–348.

138 J. Zweck, *J. Phys. Condens. Matter*, 2016, **28**, 403001.

139 N. Shibata, S. D. Findlay, H. Sasaki, T. Matsumoto, H. Sawada, Y. Kohno, S. Otomo, R. Minato and Y. Ikuhara, *Sci. Rep.*, 2015, **5**, 10040.

140 C. T. Koch and A. Lubk, *Ultramicroscopy*, 2010, **110**, 460–471.

141 T. Latychevskaia, P. Formanek, C. T. Koch and A. Lubk, *Ultramicroscopy*, 2010, **110**, 472–482.

142 C. T. Koch, *Ultramicroscopy*, 2008, **108**, 141–150.

143 C. T. Koch, *Micron*, 2014, **63**, 69–75.

144 C. T. Koch, *Acta Crystallogr. Sect. A*, 2009, **65**, 364–370.

145 M. C. Gobel, G. Gregori and J. Maier, *Phys. Chem. Chem. Phys.*, 2014, **16**, 10214–10231.

146 C.-T. Chen, C. E. Danel and S. Kim, *J. Mater. Chem.*, 2011, **21**, 5435–5442.

147 F. Iguchi, T. Tsurui, N. Sata, Y. Nagao and H. Yugami, *Solid State Ionics*, 2009, **180**, 563–568.

148 F. Iguchi, N. Sata and H. Yugami, *J. Mater. Chem.*, 2010, **20**, 6265–6270.

149 S. B. C. Duval, P. Holtappels, U. F. Vogt, E. Pomjakushina, K. Conder, U. Stimming and T. Graule, *Solid State Ionics*, 2007, **178**, 1437–1441.

150 Y. Yamazaki, R. Hernandez-Sanchez and S. M. Haile, *Chem. Mater.*, 2009, **21**, 2755–2762.

151 P. Babilo, California Institute of Technology, 2007.